Doctoral theses at NTNU, 2023:268

Thomas Vågenes Brakstad

Potential Intermediate Band Materials: Fabrication and Ellipsometric studies

Doctoral thesis

NTNU
Norwegian University of Science and Technology
Thesis for the Degree of
Philosophiae Doctor
Faculty of Natural Sciences
Department of Physics

NTNU
Norwegian University of
Science and Technology

Thomas Vågenes Brakstad

Potential Intermediate Band Materials: Fabrication and Ellipsometric studies

Thesis for the Degree of Philosophiae Doctor

Trondheim, August 2023

Norwegian University of Science and Technology
Faculty of Natural Sciences
Department of Physics

NTNU
Norwegian University of
Science and Technology

NTNU
Norwegian University of Science and Technology

Thesis for the Degree of Philosophiae Doctor

Faculty of Natural Sciences
Department of Physics

ISBN 978-82-326-7236-3 (printed ver.)
ISBN 978-82-326-7235-6 (electronic ver.)
ISSN 1503-8181 (printed ver.)
ISSN 2703-8084 (online ver.)

Doctoral theses at NTNU, 2023:268

Printed by NTNU Grafisk senter

Abstract

The intermediate band solar cell (IBSC) is a relatively new solar cell concept with the potential to increase the power conversion efficiency by over 50% compared to a traditional, single junction solar cell, while maintaining a simple, 3-layer solar cell architecture. The IBCS relies on a so-called intermediate band (IB) material and absorbs light across a wider range of the solar spectrum while maintaining a large open-circuit voltage.

One way of fabricating an IB material is to create deep levels in the bandgap of the host material. This can potentially be achieved either through heavy doping or the careful defect engineering of a wide bandgap semiconductor. The main goal of this thesis has been to fabricate (Cr + N) co-doped TiO_2 with a range of doping concentrations, using pulsed laser deposition (PLD) and to perform optical and structural characterization of the potential IB materials produced. A method for designing and fabricating samples with a continuous compositional spread (CCS) using PLD, was developed in order to speed up the material screening process. In our case, the doping concentration was varied (from approx. 2 to 10 at-%), across the 50.8 mm substrates. In addition to undoped and (Cr + N) co-doped TiO_2, the optical properties of other potential intermediate band materials have also been studied, such as sub-stoichiometric MoO_3 and Cr doped ZnS.

As an IB material must absorb light below the bandgap of the host material, a first step is to determine if sub-bandgap absorption is observed. Spectroscopic ellipsometry is an optical characterization technique which uses polarized light in order to deduce the material's optical properties and thin film thickness. Ellipsometry exploits the fact that light reflects off a material differently depending on its polarization and the material's complex dielectric function. Therefore, by varying the incoming light's polarization, and measuring the polarization state of the reflected wave, the optical properties of the material can be deduced through careful optical modelling. Thus, ellipsometry is well suited to determine if sub-bandgap absorption occurs in a material.

The main findings for the material systems studied are that all of the potential IB materials demonstrate enhanced absorption below the bandgap. However, the most promising results were obtained for the (Cr + N) co-doped TiO_2 films, which displayed an interesting sub-bandgap absorption feature in line with the predicted absorption coefficient found in literature. The sub-bandgap absorption features were found to depend heavily on both doping concentration and the crystalline properties. As the aim of this work was on *doping incorporation* into TiO_2, further work should be done in order to improve the crystalline quality of the samples produced. Sub-stoichiometric MoO_{3-x} fabricated by the spin coating technique also exhibits an interesting below bandgap absorption feature, potentially related to an IB. Further work looking into incorporating MoO_{3-x} into a solar cell device should be done in an attempt to make a complete IBSC.

List of manuscripts and publications

Paper 1

"Structural, chemical, and optical properties of TiO_2 fabricated by PLD"
Thomas Brakstad, Marina Jorge, Morten Kildemo, and Turid Reenaas
Paper Draft

Paper 2

"Improved methods for design of PLD combinatorial PLD films"
Hogne Lysne, Thomas Brakstad, Morten Kildemo, and Turid Reenaas
Journal of Applied Physics **132** (2022), p. 125301

Paper 3

"nc-PLD of (Cr+N) co-doped TiO_2 for intermediate band solar cells PART 1: Challenges in N incorporation"
Thomas Brakstad, Hogne Lysne, Marcus Grand Michaelsen, Morten Kildemo, and Turid Reenaas
To be submitted to *Solar Energy Materials and Solar Cells*

Paper 4

"nc-PLD of (Cr+N) co-doped TiO_2 for intermediate band solar cells PART 2: Optical properties and micro structure"
Thomas Brakstad, Hogne Lysne, Andreas Rosnes, Marcus Grand Michaelsen, Morten Kildemo, Randi Holmestrand, and Turid Reenaas
To be submitted to *Solar Energy Materials and Solar Cells*

Paper 5

"Tailoring properties of nanostructured MoO_{3-x} thin films by aqueous solution deposition"
Katherine Inzani, Mohammadreza Nematollahi, Sverre M. Selbach, Tor Grande, Magnus Langøien Waalekalv, Thomas Brakstad, Turid Worren Reenaas, Morten Kildemo, and Fride Vullum-Bruer
Applied Surface Science **459** (2018), pp. 822-829

Paper 6

"Sub-stochiometric MoO_3 for intermediate band solar cells"
Marina Jorge, Thomas Brakstad, Mohammadreza Nematollahi, Morten Kildemo, and Turid Reenaas
In 2019 IEEE 46th Photovoltaic Specialists Conference (PVSC). IEEE 2019, pp. 1756-1759.

Paper 7

"Ellipsometric study of the optical response of ZnS:Cr for PV applications"
Thomas Brakstad, Benjamin R. Hope, Mohammadreza Nematollahi, Morten Kildemo, Nikolas J. Podraza, Kiran Ghimire, and Turid W. Reenaas
Applied Surface Science **421** (2017), pp. 315-319

My contributions to the publications

For several of the works included in this thesis, a CRediT author statement[1] is included at the end of the paper, giving information on who contributed to which part of the work. A brief description of my contributions to the papers is given below.

Paper 1: Turid Reenaas and I conceptualised the study and planned the film growth. I performed the thin film deposition together with Marina Jorge. Marina Jorge did the XPS measurements and analysis. I performed the ellipsometry measurements analysis. I also performed the XRD measurements. Marina Jorge and I wrote the draft and we reworked the manuscript together with Turid Reenaas.

Paper 2: Hogne Lysne, Turid Reenaas and I conceptualised the study, developed the method and planned the film growth. I performed the thin film deposition together with Hogne Lysne. I performed the ellipsometry measurements and analysis. I wrote the original draft together with Hogne Lysne and we reworked and finalized the manuscript together with Turid Reenaas.

Paper 3: Hogne Lysne, Turid Reenaas and I conceptualised the study and planned the film growth. I performed the thin film deposition together with Hogne Lysne. I performed the ellipsometry measurements and analysis. Marcus Grand Michaelsen and I performed the XRD measurements. I wrote the original draft together with Hogne Lysne and we reworked and finalized the manuscript together with Turid Reenaas.

Paper 4: Hogne Lysne, Turid Reenaas and I conceptualised the study and planned the film growth. I performed the thin film deposition together with Hogne Lysne. I performed the ellipsometry measurements and analysis. I wrote the original draft together with Hogne Lysne and we reworked and finalized the manuscript together with Turid Reenaas.

Paper 5: I performed the ellipsometry measurements and determined the optical models together with Magnus waalekalv. I contributed writing on the parts on ellipsometry and determining and interpretation of the optical properties in the original draft.

Paper 6: I performed the ellipsometry measurements and determined the optical models. I contributed writing the section on the optical properties in the original draft and finalized the manuscript together with Marina Jorge and Turid Reenaas.

Paper 7: Mohammadreza Nematollahi performed the thin film deposition. Benjamin Roaldsønn Hope performed the ellipsometry measurements and I determined the optical models together with the rest of the co-authors. I wrote the original draft together with Morten Kildemo, and we reworked and finalized the manuscript.

[1] Brand, Amy, et al. "Beyond authorship: attribution, contribution, collaboration, and credit." Learned Publishing 28.2 (2015): 151-155.

List of manuscripts and publications not included in this thesis

Paper 8

"Dispersion of polarization coupling, localized and collective plasmon modes in a metallic photonic crystal mapped by Mueller Matrix Ellipsometry"
Thomas Brakstad, Morten Kildemo, Zahra Ghadyani, and Ingve Simonsen
Optics Express **23**, no.17 (2015), pp. 22800-22815

Paper 9

"Optical response of gold hemispheroidal lattices on transparent substrates"
Morten Kildemo, Jean-Philippe Banon, Alexandre Baron, Brage B. Svendsen, Thomas Brakstad, and Ingve Simonsen
Applied Surface Science **421** (2017), pp. 593-600

Paper 10

"Optical response of rectangular array of elliptical plasmonic particles on glass revealed by Mueller matrix ellipsometry and finite element modeling"
Per Magnus Walmsness, Thomas Brakstad, Brage B. Svendsen, Jean-Philippe Banon, John C. Walmsley, and Morten Kildemo
JOSA B **36**, no.7 (2019), pp. E78-E87

Paper 11

"Characterization of bandgap changes in Cu_2O by single doping and N,K-codoping"
Marina Jorge, Katherine Inzani, Thomas Brakstad, Trygve Sørgård, Cristian Soncini, Federica Bondino, Igor Pis, Silvia Nappini, Christophe Licitra, Jean-Paul Barnes, Narciso Gambacorti, Luke Antwis, Sverre Selbach, Turid Reenaas, and Maddalena Pedio
Paper draft[2]

Paper 12

'TEM Study of Cr, N co-doped TiO_2 Continuous Composition Spread Thin Film Made With Natural Spread Combinatorial-PLD"
Andreas Rosnes, Hogne Lysne, Thomas Brakstad, Emil Christiansen, Turid Reenaas, and Randi Holmestrand
Paper draft[3]

[2] Marina Rodrigues Jorge. "Potential Oxide-Based Intermediate Band Materials: Fabrication and Photoemission Studies" PhD thesis. NTNU, 2020

[3] Hogne Lysne. "Design and fabrication of (Cr+N) co-doped TiO_2 films with a continuous compositional spread" PhD thesis. NTNU, 2023

Preface

This thesis is submitted to the Norwegian University of Science and Technology (NTNU) as a partial fulfillment of the requirements for the degree of Philosophiae Doctor. This work resulted in 4 published articles and three unpublished paper drafts. All of the articles are related to potential intermediate band materials characterized by spectroscopic ellipsometry. This thesis has been carried out under the supervision of Professor Turid Reenaas and Professor Morten Kildemo, both working at the Department of Physics at NTNU, and funded as part of the OX-IB project (RCN Project No. 240466) through the Research Council of Norway.

Thomas V. Brakstad
Trondheim, Norway
June 2023

Acknowledgments

Looking back at the (several) years as a Ph.D. candidate at NTNU, I have many fond memories and truly a lot of great colleagues whom I've had the pleasure to work with.

First of all, thank you to my main supervisor, Professor Turid Reenaas, not only for the opportunity and guidance along the way for me to pursuit my dream of a Ph.D. degree, but also for her patience and understanding. The same thank you goes to my co-supervisor, Professor Morten Kildemo, whom I'm going to miss going to conferences with as much as playing football with. You have both, with your patience, managed to guide me through a Ph.D. Thank you.

Another, who deserve a truly spectacular thanks for hauling me through at the end of this thesis, is my colleague and officemate, Hogne Lysne, who, by his sheer multi-tasking ability and productivity, managed to get many of our seemingly overambitious ideas put to life. Thank you, for being a good colleague and a great friend.

Also, another office mate who had to endure my 'makrell i tomat' in front of the computer, as well as waiting for my plots before hard deadlines, Marina Jorge, thank you for being a good friend and colleague.

Of other help, in the lab or in publishing papers, i would like to thank Mohammadreza Nematollahi, for his guidance in the PLD lab and contributions to several articles. Also, thank you to Katherine Inzani, for including me in her work on reduced MoO_3. Thank you to Ken Roger Ervik and Kristoffer Kjærnes, for helping me out, on several occasions, with issues regarding Nanolab and XRD, respectively. Also, a great deal of work has been done by fantastic master students, and a special thank you to Magnus, Herman, Benjamin, Andreas, and Marcus, for producing great data and data analysis. Thank you.

I suppose Ph.D. students as a group are as homogeneous a work force as any, and I will truly miss my Ph.D. colleagues as much in the lunchroom as well as at the bouldering center. Thank you especially to Per Magnus, who had to share a hotel room with me on several trips abroad, and Trygve, for making night shift at synchrotron a memorable experience. Thank you to Nina for helping me see progress along the way.

Thank you mamma og pappa, for everything, including not knowing any better and therefore not warning me against starting on a PhD. It has been a journey I would not be without and has made me a richer person. And finally, thank you so much Elisabeth, for your patience and understanding regarding this whole PhD project. I would never have finished it without your help and support, and for that, I will be forever grateful. ♡

Contents

Part I

Introduction

1 Introduction

1.1 Motivation

According to the Emissions Gap Report 2022, time is running out for the countries of the world to prevent irreversible global climate change and calls for a rapid transformation to a sustainable society [1]. This can only be achieved if a large part of the world power consumption is generated from renewable energy sources, like wind energy and solar energy, while at the same time addressing issues like seasonal energy storage and investing in smart grids and long-distance electricity transportation [2]. Even though the cost of the current solar cells has been drastically reduced (from 80 to 0.3 $\$/$W from 1980 to 2019 [3]), the potential for enhancing the energy conversion efficiency is large: the current Si-based solar cell approaches the theoretical maximum conversion efficiency limit of $\sim$ 30 % for a single junction solar cell with bandgap of 1.1 eV [4]. If we are to produce photovoltaic electricity in large scale, close to where people live, and without destroying too much natural habitats, higher efficiency solar cells are highly desirable [5]. One newly proposed solar cell technology, the intermediate band solar cell (IBSC), is predicted to have as high as 49% energy conversion efficiency operating at 1 sun, that is, over 50% higher efficiency than the current theoretical maximum of the Si based solar cell [6]. This increase in efficiency follows from just adding a single extra layer to the traditional solar cell design, which makes the IBSC an interesting concept worth exploring.

1.2 IBSC State of the Art

Intermediate band solar cells (IBSCs) are based on an intermediate band (IB) material, in which a narrow, intermediate energy band is present in the forbidden bandgap of a semiconductor [7,

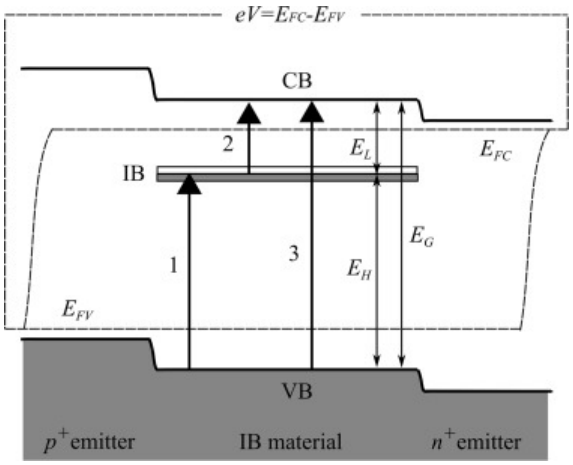

Figure 1.1. A band diagram illustrating the main principle of an IBSC. A wide bandgap material, with bandgap energy E_G, is modified with a partially filled, intermediate band, IB, which effectively makes the material behave like a '3-bandgap' material, E_H, E_L and E_G. The IB must be electrically isolated from the p and n emitting layers of the solar cell, maintaining the large open circuit voltage of the wide bandgap semiconductor, $eV = E_{FC} - E_{FH}$, while facilitating for photons with $E < E_G$ to contribute to the photogenerated current. Figure from ref. [9]

8]. A schematic band diagram of such an IB material in a solar cell is given in Fig. 1.1. In an IBSC, electron-hole pairs can be generated in one of two ways: either by absorbing photons with energies above the bandgap of the material, E_G, like a traditional solar cell, or, electrons can be excited by absorbing two sub-bandgap energy photons (if they have higher energies than E_H and E_L, see Fig. 1.1), by using the IB as an intermediate 'step'. This additional route for exciting electrons from the valence band to the conduction band is the reason behind the IBSC enhanced conversion efficiency, and less energy is wasted to producing heat. To maintain the large open circuit voltage related to the initial wide bandgap of the host material, the IB-material must be sandwiched between two wide bandgap p- and n-emitters, which take care of the current collection and transfer to the outer electrodes. This ensures that the output voltage over the cell, eV, is not reduced due to the presence of the intermediate band, but is proportional to the quasi-Fermi level split of electrons (E_{FC}) and holes (E_{FH}), $eV = E_{FC} - E_{FH}$, see Fig. 1.1 [9].

There are three main strategies in order to create an intermediate band material, namely: 1) by utilizing confinement effects in quantum dots [10], 2) by fabrication of highly mismatched alloys [11], or 3) by ultrahigh doping in a wide bandgap semiconductor in order to create levels deep into the bandgap [12]. The latter concept is the least investigated and is based upon having a high enough concentration of dopants (uniformly distributed in the host material) merging de-localized electron states into an energy band. When such a band is formed, the effects of non-radiative Schokley-Read-Hall recombination, which occurs when the electron states in the bandgap are localized (typically caused by impurities and point defects in ordinary solar cells), are predicted to be suppressed [13]. However, this topic is controversial, and some authors, like Kirch et. al [14], argue that a de-localized band will become localized by phonons in the recombination process. However, Kirch does not discard the deep level IB concept but suggests, instead of focusing on the

de-localization of the IB bands, to rather focus on finding IB materials with a high photo absorptivity and small capture cross section for electrons and holes [15, 16]. Thus, the deep level IB material concept can be considered controversial.

A functioning IBSC has already been demonstrated for quantum dots, which is also the most heavily researched approach to fabricating an IB material [17]. None the less, high efficiencies (>19 % [18, 19, 20]) has not yet been achieved, as the difficulty lie in having an extremely high quantum dot density and narrow size distribution in an operating IBSC. In addition, quantum dots are mostly fabricated using toxic, non-abundant materials, and synthesized by expensive fabrication methods. Therefore, the less studied, deep level approach, even though it could be considered controversial, is an approach worth investigating further none the less.

For a specific semiconductor material to be considered as a promising host of an IB-material, the bandgap should be in the range of $\sim$1.5- 3.5 eV [21], it must be possible to achieve an ultra-high doping concentration (up to several atomic percent), and the carriers in the conduction band and valence band must have high enough mobilities in order to be collected. For a sustainable development, the material should also be non-toxic, for humans and the environment, and should consist of abundant elements.

This thesis has investigated new potential deep level IB materials, both in terms of fabrication and in terms of characterizing the novel materials' optical, structural, and topographical properties. As both fabricating and demonstrating an IB material is a large endeavor for a PhD, the focus here has been to investigate if the fabricated materials demonstrate optical absorption below the bandgap of the host material. Although the goal is to fabricate an IBSC, the IB material in itself has many potential other use cases, i.e., in photocatalytic or gas sensing applications.

1.3 Outline of Thesis

The thesis is structured as follows: in chapter 2, I will introduce the material systems studied in this thesis, namely (Cr + N) co-doped TiO_2, substoichiometric MoO_3, and Cr doped ZnS. In chapter 3, I will describe the basic concepts of how the samples were fabricated, which for most samples included in this thesis was done using pulsed laser deposition (PLD). In chapter 4, the main characterizations techniques used in this work will be presented, both basic physical principles of the techniques, and how these techniques complement each other. Finally, in chapter 5, I will give a summary of the thesis; suggestions for future work will also be presented. The results of this thesis' investigations are summarized in several manuscripts and articles included in Part 2 of this thesis.

2
Material Systems

In this chapter, I will present the motivation and some of the literature in light of fabricating (Cr + N) co-doped TiO_2, which has been the main focus of this work. I will also present a brief literature motivating substoichiometric MoO_3 and Cr doped ZnS as candidate IB materials, for completeness, even though I have mainly been responsible for the optical characterization of the latter material systems.

2.1 (Cr + N) co-doped TiO_2

TiO_2 is a well-studied, wide bandgap ($\sim$ 3.0-3.3 eV depending on crystal structure) semiconductor that occurs in nature mainly in three crystal structures, or phases; rutile, anatase and brookite, with the first two as the most stable. TiO_2 has found its way into a myriad of different applications, from white pigment in paints [22], transport layers and anti-reflection coatings in solar cells [23], as well as recently receiving a lot of attention for photo catalysis applications [24, 25, 26]. In addition, some theoretical studies have identified Cr and N co-doped anatase TiO_2 as a potential IB material candidate with a potential efficiency of 56.7% under fully concentrated sunlight [27]. Even though the study suggests anatase as the preferred crystal structure, it is not unambiguously clear which phase would be the best choice as host matrix for a TiO_2 based IB material: anatase, rutile, or a mix. Anatase might have a higher carrier mobility [28], higher conductivity, and longest carrier lifetimes compared to rutile [29], which might be due to anatase being an indirect bandgap semiconductor with rutile as a direct bandgap semiconductor [30]. However, as has been observed for TiO_2 in photocatalytic applications, a mix of anatase and rutile phase could even be beneficial [31].

Several theoretical studies have been published on Cr and N co-doping of TiO_2 which predict that the resulting material has an intermediate energy band inside the bandgap of TiO_2 [32, 33,

34, 35, 36]. There has also been several experimental reports on the fabrication of Cr and N co doped TiO_2, both from other deposition methods [37, 38, 39, 40, 41] and by PLD [42, 43, 44, 45], but few with a ultra-high doping concentration (above several at.%), and none has studied the material system as an IB material candidate. Most authors study (Cr + N) co-doped TiO_2 for photocatalysis applications, with the aim of reducing the bandgap; not produce an isolated intermediate band. The idea for the current PhD project was therefore to utilize so-called non-compensated co-doping scheme of TiO_2 fabricated using combinatorial PLD [46, 47, 48], in order to screen for optical properties against high doping concentrations. TiO_2 has previously been fabricated by many different deposition techniques, including PLD [49, 50, 51]. PLD is generally considered well suited for prototyping complex oxides due to the high flexibility with regards to the materials being deposited, high structural quality and complex stoichiometry of the materials produced.

In this thesis, the optimization procedure for fabricating single phase rutile, anatase and mixed phase thin films, both stoichiometric and substoichiometric, and subsequent chemical, structural and optical analysis resulted in paper 1. The optimization procedure for designing combinatorial (Cr + N) co-doped TiO_2 thin films resulted in paper 2. The final (Cr + N) co-doped TiO_2 and the analysis of its' structural and optical properties resulted in paper 3 and 4.

2.2 Substoichiometric MoO_3

In addition to the doping approach motivating (Cr + N) co-doped TiO_2, point defects (vacancies, interstitials etc.) are inevitable in the fabricated materials, and these can affect the material's opto-electronic properties. In this thesis, substoichiometric MoO_3 (MoO_{3-x}) has been studied as a candidate IB material.

MoO_3 is also a highly studied, wide bandgap ($\sim$3.0 eV) transition metal oxide with several application, such as in catalysis [52, 53], gas detection [54] inorganic light emitting diodes[44], li-ion batteries [55] and electrochromic and photochromic devices [56, 57]. MoO_3 crystallize in a orthorhombic layered structure [58]. In addition, MoO_3 has a number of stable phases of MoO_{3-x} in the regions $0<x<1$ [59, 60, 61, 62, 63, 64], and different oxygen vacancies create different energy levels in the bandgap of MoO_3 [65]. By controlling the stoichiometry of MoO_{3-x}, one can control the position and filling of these states [66, 67, 68]. These studies suggest that the sub-bandgap states could be exploited in order to fabricate an intermediate band material, used as the absorption layer in an IBSC.

In this thesis, MoO_{3-x} fabricated by both spin coating technique and by PLD has been studied by spectroscopic ellipsometry. The samples studied were fabricated by my colleagues Katherine Inzani and Mohammadreza Nematollahi, and the optical investigations done by me contributed to paper 5 and 6, respectively.

2.3 Cr doped ZnS

ZnS is a non-toxic and abundant semiconductor material with a wide bandgap ($\sim$3.6-3.9 eV depending on crystal structure) for which theoretical studies suggest an intermediate band would form by Cr doping [69, 70]. ZnS has a bandgap which is wider than ideal values ($\sim$1.5 - 3.5 eV

[21]) for an IBSC. None the less, Cr doped ZnS is a good potential candidate to demonstrate the intermediate band concept and calls for further investigation.

The Cr doped ZnS samples studied in this thesis were fabricated by PLD by former PhD candidate Mohammadreza Nematollahi [71, 72, 73]. The optical data acquisition was done by my former colleagues Lars Martin Aas and Benjamin Roaldsønn Hope, and the ellipsometric data analysis, presented in paper 7, was done by me.

3

Pulsed Laser Deposition

Several fabrications techniques has been utilized in order to produce the samples studied in this thesis. However, the main experimental fabrication technique used by me is pulsed laser deposition (PLD), which was used for making the single component TiO_2 films of paper 1, the combinatorial PLD films of paper 2, and the (Cr + N) co-doped films of paper 3 and 4. Therefore, PLD and continuous compositional spread (CCS) PLD will be presented in this chapter. It should be noted, however, that this is not a detailed explanation of the complete PLD process, but merely an introduction to the basic concepts of PLD. The interested reader is referred to either [74] or [75], both excellent textbooks on thin film deposition and PLD. Also, the experimental details of the main work contained in this thesis are given in the respective papers, included in part 2 of this thesis.

3.1 Conventional PLD

Pulsed lased deposition (PLD) is a highly flexible deposition technique which is generally well suited for prototyping new materials; this is due to the possibility to ablate nearly any target material, the ability to deposit with a layer-by-layer control, by changing the ablated target, and to deposit material in a reactive atmosphere, even under high ambient pressures. Finally, PLD offers the possibility of depositing material 'out of thermal equilibrium', or with high (10-100eV) kinetic energy of the incoming species, which could overcome potential barriers in (heavily doped) crystal formation. Some of the challenges often associated with PLD includes particulates depositing in the films, and the inhomogeneous thickness distribution of the films due to the size of the plume. This inhomogeneous thickness distribution, however, might be used as an advantage, which will be discussed in the combinatorial section below. Even though methods for using PLD in commercial production lines are being developed [76, 77, 78], using PLD for large scale PV production might not be sustainable, as it is an energy demanding deposition process. Nonetheless, the large

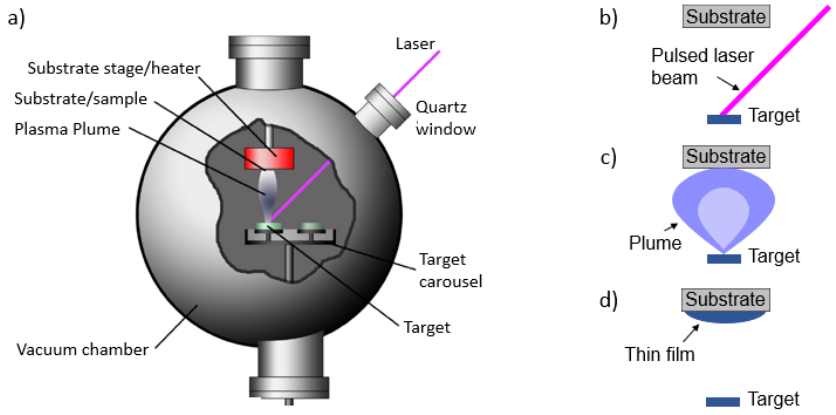

Figure 3.1. (a) A figure illustrating the PLD setup with the main components labeled. (b), (c) and (d) illustrate the PLD deposition process in which a laser interacts with the target (b), a plasma plume is generated (c), and a thin film is deposited onto the substrate (d).

prototyping capabilities of PLD should still be exploited with the aim to demonstrate the deep level IBSC concept.

A schematic illustration of a typical PLD set-up is shown in Fig. 3.1 (a) in which a vacuum chamber is shown with the main components labeled: the target carousel with different target materials mounted, a substrate/sample mounted close to a substrate heater, and a plasma plume, which is ignited by the incoming laser through a quartz window (often at around 45-55 degrees incident to the target). The steps of the PLD process is illustrated in Fig. 3.1 (b), (c) and (d). First, a pulsed, high-power laser hits the target material inside the vacuum chamber, illustrated in (b). The laser ignites a plasma plume which ejects target material into the vacuum chamber, shown in (c), and the incoming material deposits on the substrate, resulting in a thin film, illustrated in (d). The material spread will depend on the plume shape and size, which again depends on the deposition parameters, like laser spot size on the target and chamber pressure.

Thus, fabricating thin films by PLD might seem like a relatively straight forward procedure, but the physical processes involved can, in fact, be quite complex. For example, an ablated TiO_2 target could produce different species, like Ti- or O- ions, or TiO or TiO_2 molecules. The different species can interact with the ambient chamber gas, i.e. Ar, O_2 or N_2 (or a mix), in order to modify the plume shape and kinetic energy of incoming species onto the substrate, or even chemically alter the incoming species altogether (i.e., changing Ti molecules into TiN molecules for ablation in an N_2 atmosphere). Care must even be made on laser repetition rate, as ablating a target heats the target itself up, potentially causing oxidation of i.e. a CrN target for depositions using a high oxygen background pressure. The species that hit the substrate will either stick to the substrate (or film) surface where they land (forming unordered, amorphous, potentially porous films), diffuse around the surface and bond in a crystalline structure (forming poly-crystalline, textured, or single crystal thin films), or be re-emitted into the vacuum chamber, again depending on deposi-

tion properties such as substrate temperature and chamber background pressure. Some general structural characteristics and trends covering properties like substrate temperature, chamber pressure, or species kinetic energy can be described by i.e. a structure zone model [79, 80, 81, 82]; however, a complete physical description of the various mechanisms involved in PLD growth are beyond the scope of this thesis. The main aim of this work has been to incorporate different doping concentrations into the films with some crystal phase control.

3.2 Combinatorial PLD

In conventional PLD, the substrate is often rotated throughout the deposition in order to produce more uniform film properties. However, in continuous compositional spread CCS films, the fact that the plume and subsequent thin film has a non-uniform thickness distribution is exploited to our advantage. If instead of continuously rotating the substrate, the substrate is kept still during the deposition of one target material, and then rotated, for instance 180 degrees, before depositing using another target material, a thin film with a continuously varying doping concentration along a 'centerline' is made, see Fig. 3.2. In Fig. 3.2 (a), target 1 is ablated and deposits material 1 on the substrate. In Fig. 3.2 (b), the substrate has been rotated 180 degrees, the target has been changed to target 2, and a thin layer of material 2 is deposited as illustrated. When this process is repeated, the deposited thin film will have a layered structure illustrated in Fig. 3.2 (c). This method could be extended to include more target materials and deposited at different rotation angles [46].

In order to fully utilize PLD's unique ability for layer-by-layer deposition with a 'built in' film thickness gradient, a careful mapping of each of the targets' material spread is needed in order to design the desired CCS film. For this purpose, spectroscopic ellipsometry is an ideal tool, as it obtains both information on film thickness and local optical properties. Before the CCS film is designed and fabricated, single component plume calibration films for each target needs to be deposited (using the same parameters, such as laser fluence, target-substrate distance, background pressure etc.), without rotating the substrate during deposition, and the film thickness needs to be carefully mapped out in order to model the plume material distribution. Then, by using our in-house developed python code [83], the desired doping concentration or film thickness distribution can be designed and the optimal position of plume center in relation to the substrate is calculated.

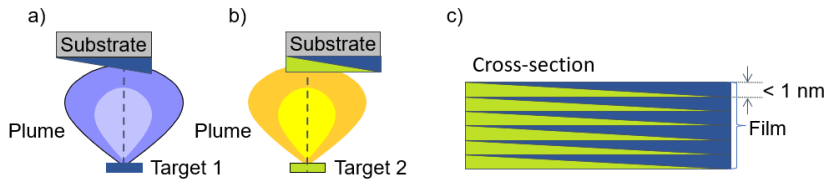

Figure 3.2. (a) A schematic indicating material from target 1 depositing inhomogeneously across the substrate. (b) A schematic illustrating the buildup of a continuous compositional spread where the ablated material from target 2 is deposited on top of the deposited material from target 1, after the substrate has rotated 180 degrees about the center of the substrate. (c) The resulting CCS film, where each layer is indicated as less than 1 nm.

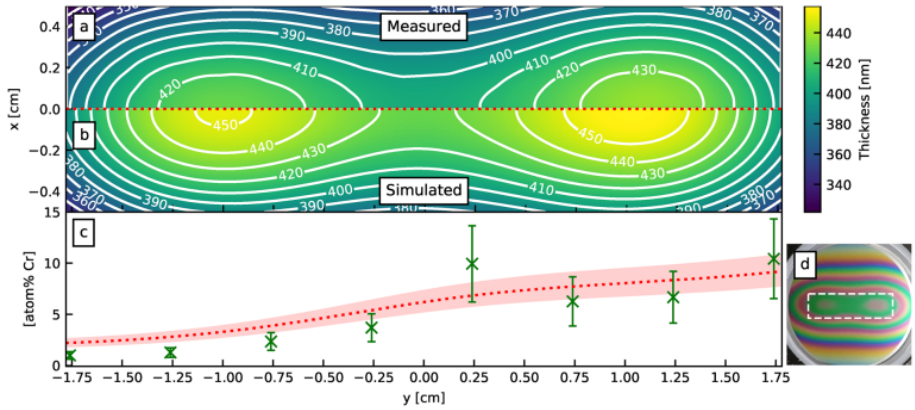

Figure 3.3. (a) The measured thickness distribution of a (Cr + N) co-doped TiO_2 thin film (CCS-O-700), for the central (3.5 cm x 1.0 cm) part of the 50.8 mm diameter substrate, using spectroscopic ellipsometry. (b) The simulated thickness distribution based on single component plume film samples and a subsequent computational optimization procedure. (c) Calculated (red dashed line) and measured (green 'x') Cr at.% along the 'centerline' between the two plume centers. The concentration measurements were done using secondary ion mass spectroscopy (SIMS). (d) A top view photograph of the sample with the thickness distribution plotted in (a) and (b) indicated by a white dashed rectangle. Figure taken from ref. [83].

For instance, we wanted to explore different Cr and N doping concentrations of (Cr + N) co-doped TiO_2 for IB applications (paper 3 and 4) and aimed to make a (Cr + N) co-doped TiO_2 sample with a CCS of Cr and N varying from $\sim$ 2 to 10 at.%. This resulted in a sample with a relatively uniform thickness ($\sim$400$\pm$25 nm) along a 3 cm 'centerline' (on a 2" Si wafer) for which the doping concentration is optimized, see Fig. 3.3. In Fig. 3.3 (d), a top view photograph of a 2" Si wafer with a CCS (Cr + N) co-doped TiO_2 film is shown. The interference fringes seen in the photograph are a clear indication of the thickness variation of the film towards the edges of the wafer. The superimposed white rectangle on the photograph indicates the area of interest for which the thickness uniformity was optimized and subsequently characterized by spectroscopic ellipsometry. The thickness distribution map of the film measured by ellipsometry is plotted in Fig. 3.3 (a), and the simulated thickness map is given in Fig. 3.3 (b). The simulated (red dashed line) and measured (using SIMS, plotted here in green 'x') Cr at.% concentration is plotted in Fig. 3.3 (c). Figure taken from ref. [83]. As can be seen from Fig. 3.3, the thickness distribution and Cr doping concentration is very similar to the simulated properties and demonstrates the flexibility of PLD for prototyping CCS films. For further details regarding the CCS procedure and Fig. 3.3, see paper 2 (ref. [83]).

One challenge encountered when using/depositing the full width of the plume for fabricating CCS films is the variation of the kinetic energy of the incoming species in the plume. The kinetic energy is highest at the plume center (indicated by the dashed lines in Fig. 3.4). Further away (on the substrate) from the plume center, the species in the plume have traversed a longer distance from the target to the substrate. This leads to more interactions between the ablated species and with the background gas, and thus, less kinetic energy for the incoming species for diffusion on the

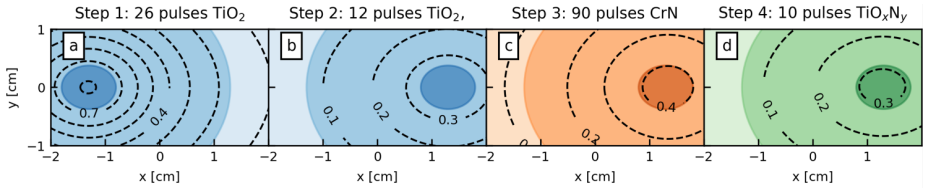

Figure 3.4. (a-d) Contour plots of simulated deposition of four steps in the natural spread CCS PLD cycle (for the CCS-Cap-1 sample, see Paper 4). The color shading indicates deposition at the plume center (dark color), flank (medium) and far-flank (light) which result in decreasing kinetic energy of the incoming ad-atoms from the plume. Figure adapted from [84].

substrate. In Fig. 3.4, a graphical representation of the spread in the deposited material for one of the CCS films fabricated in this thesis is shown. Each panel (a) - (d) in the figure shows almost the same central area of the substrate as in Fig. 3.3, but is for another CCS film (CCS-Cap-1). In Fig. 3.4 the central (4 cm x 2 cm) is shown, while in Fig. 3.3 the central (3.5 cm x 1 cm) is shown.

The material is in any case unevenly deposited on the substrate, indicated by the contour plots in Fig. 3.3 (a) - (d), where the kinetic energy of the incoming species is divided into 3 regions: 'plume center', 'plume flank' and 'plume far flank' indicated by the three shades of each color. The darkest colour indicates the highest kinetic energy, schematically. The different colors indicate different target + background gas combinations. For full details regarding the deposition procedure, see paper 4. From the figure, we see that the region between the two plume centers (at $x = 0$ cm), only material from the plume flank is deposited. For each of the plume centers (at $x = \pm 1.3$ cm), most of the material is deposited from the plume center area, but some come from the far plume flank region. As will be presented in Paper 4, the use of the full plume width for the deposition of the CCS films has a negative impact on the crystalline quality in certain regions of the films. This means that even though we achieved the goal of fabricating films with a compositional gradient, still more work must be done to optimize the crystalline quality.

4

Characterization methods

In the following chapter, I will give a brief description of how the primary characterization tools utilized in this thesis works and what material properties can be obtained. However, it will not be a detailed mathematical description of all the physical principals involved. For a great introduction to practical materials characterization, see reference [85]. Also, for a comprehensive description of characterization of solar cell materials by spectroscopic ellipsometry, reference [86] is highly recommended.

4.1 Spectroscopic Ellipsometry

Spectroscopic ellipsometry is a bonkers bananas characterization technique. Or, put in a more scientific term, 'the technique *par prefèrènce*' for investigating the optical properties of materials [87]. It has been, by far, the most important characterization technique in this thesis, and a perfect companion to prototyping thin films made by PLD. Spectroscopic ellipsometry gives highly accurate information on the film thickness as well as the optical properties of thin films, which again is highly related to the crystalline structure (polymorph, amorphous, porosity etc.), bandgap, absorption coefficient and can even give details regarding the band structure of the material. It is fast, non-destructive, and even has mapping capabilities. The main disadvantage of spectroscopic ellipsometry is that it is a 'non-direct' measurement technique, as the optical properties and film thickness are not found directly from the measurements, but through careful optical modeling. Therefore, measurements using other techniques, like AFM, XRD and SEM/TEM, are often needed in order to confirm the ellipsometric results.

Ellipsometry exploits the fact that electromagnetic waves, which is reflected off (or transmitted through) a material, changes its polarization due to the material's optical properties. If the polarization state of the incident light is known, and the polarization state after the light-sample

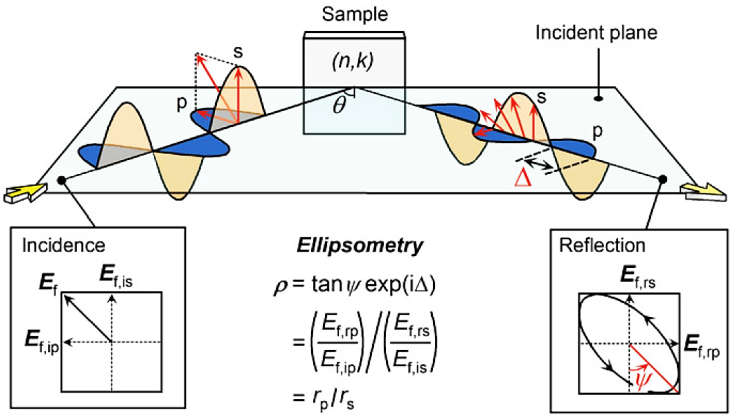

Figure 4.1. A schematic drawing illustrating the main principle of ellipsometry. Polarized light with a parallel (p) and perpendicular (s) component to the incident plane is incoming from the left side, then reflected off the sample in the specular direction to the angle of incidence, θ, and the polarization change is measured in the forms of the ellipsometric angles ψ and Δ. For an ideal case, that is, an infinitely thick substrate with no surface roughness, ψ is related to the relative amplitude ratio of the Fresnel coefficients for p to s polarized light, and Δ is related to the change in phase between s and p polarized light. Figure adapted from [86]

interaction is measured, the change in polarization due to the light-sample interaction can be directly linked to the *total samples'* optical properties. This "total samples' optical properties" include properties like surface roughness of the sample, substrate optical properties, film thickness, and, of course, the complex dielectric function of the thin film itself, just to mention a few parameters. The main challenge with ellipsometry lies in decomposing the contribution from each component, and in the process, determine the film optical properties and thickness.

Fig. 4.1 illustrates the basic principles of ellipsometry. Electromagnetic waves of a known polarization, with the electric field components denoted 'p' and 's', parallel and perpendicular to the plane of incidence, respectively, is incident at a certain angle of incidence, θ, onto a sample. The reflected wave's change in polarization state, represented by the ellipsometric parameters Ψ and Δ, or, the relative field amplitude ratio and phase difference, respectively, is then measured. The challenge then lies in the de-composition of all the contributing factors to the polarization change of the sample, which is done in terms of optical modeling. To guide in this process, several textbooks are available, such as [88, 89]. For solar cell specific materials, [86] is recommended.

Transmission measurements

Spectroscopic ellipsometry is highly sensitive to both transparent films and absorbing films. One area in which ellipsometry is not sensitive is when the material is weakly absorbing, with $\alpha < 500\mathrm{cm}^{-1}$ [86]. In this case, transmission measurements are often performed to assist in the optical modelling, to extract more precise information on the optical bandgap of the material [89]. It can sometimes be useful to divide the ellipsometric spectra into different regions depending on whether or not the film is completely transparent, slightly absorbing, or highly absorbing, as in the interband

transition region [90]. Subsequently, the regions can be connected by assuming the real part of the dielectric function is continuous and that the real and imaginary part of the dielectric function is Kramer-Kronig consistent.

In this thesis, every paper I have contributed to contains some ellipsometry analysis, usually accompanied by transmission measurements whenever possible (the exception being single side polished substrates or non-transparent substrates).

4.2 Atomic Force Microscopy

Atomic force microscopy (AFM) is a common characterization technique used to acquire information on the surface topography of samples. For instance, to see if a substrate preparation process gives atomically smooth steps or leaves contaminants, or in order to find root mean square values of the surface roughness of thin films. Fig. 4.2 (a) show a schematic drawing of the AFM instrument. A cantilever driven by a piezo transducer is operated through a controller. The cantilever is scanned over the sample, either in tapping mode or contact mode. A laser is reflected off the cantilever so that the motion of the cantilever can be monitored by a photodetector. In Fig. 4.2 (b), a 1x1 μm^2 AFM image is shown of a $LaAlO_3$ substrate after annealing at 1025 °C for 2 hours. As seen, the 3.35 Å terraces, corresponding to $LaAlO_3$'s unit cell height, are clearly visible, ascribing to the high sensitivity of the AFM tool.

AFM gives a very direct measure on the surface topography of thin films and substrates and is a great way to evaluate the surface roughness deduced by ellipsometry. As long as the wavelength of the probing ellipsometric light is considerably longer than the surface roughness features of the film ($\lambda >> AFM_{rms}$), several studies have confirmed a linear trend between surface roughness found by ellipsometry and AFM [91, 92]. However, depending on the lateral dimensions of the roughness features, more elaborate optical modeling might be needed in order to deduce the roughness more accurately [93] and thus, care must be taken when obtaining surface roughness using ellipsometry. One disadvantage of AFM is that it only 'see' roughness in a small area [83]. Therefore, ellipsometry and AFM complement each other very well; ellipsometry with fast measurements and mapping of roughness trends, and AFM to control-check root mean square (rms) values at select locations [83].

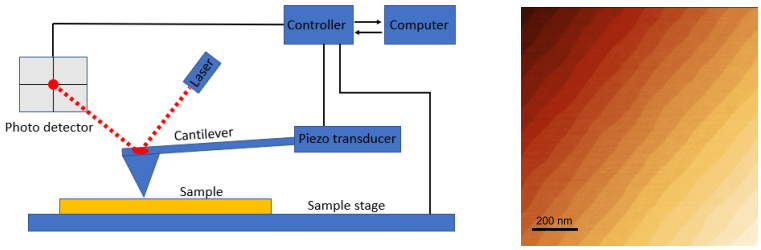

Figure 4.2. Left: A schematic drawing illustrating the main components of the AFM. Right: 1x1 μm^2 AFM image of a $LaAlO_3$ substrate baked at 1025 °C for 2 hours. The steps indicate the unit cell of $LaAlO_3$ (∼3.8 Å), the scale bar is 200 nm and the color code indicates a 10 nm height variation (from 0 to 10 nm).

4.3 X-ray Diffraction

X-ray diffraction (XRD) is an experimental technique used to find information of a samples' crystalline properties, i.e., if the sample is crystalline or amorphous, which crystal phases are present (both which chemical phase, i.e. TiO_2 vs Ti_2O_3, and which polymorph, i.e. anatase TiO_2 or rutile TiO_2), and information on the film's texture, or preferred crystal orientation (often in relation to the substrate). XRD utilizes that electromagnetic waves of a certain wavelength (X-rays) *diffract* from the inter-planar spacings between two neighboring crystal planes, which are made up from the atomic order in the crystal. These inter planar spacings are also known as d-spacings. The diffracted X-rays create local interference maxima at certain angles of incidence/reflectance which is then measured and can be regarded as a 'fingerprint' of a certain crystallographic phase.

The basic concept of XRD is illustrated in Fig. 4.3. In Fig. 4.3 (a), a cross section of a simple crystal is shown where different planes with different d-spacings are drawn in. Each of these planes would create different intensity peaks at certain angles of incidence/diffraction. In Fig. 4.3 (b), an X-ray is incoming at an angle θ to a crystal with d spacing d. Constructive interference occurs when the angle of incidence and reflection satisfy Bragg's law: $n\lambda = 2d\sin(\theta)$. Here, n is a whole number, λ is the wavelength of the electromagnetic wave (X-ray) in nm, d is the d spacing (in nm), and θ is the angle of incidence, respectively.

XRD scans can be taken in different configurations depending on what type of sample it is (a powder or thin film sample) and what degree of crystallinity and texture is expected (polycrystalline vs textured vs single crystal thin films). An un-textured, polycrystalline thin film consists of crystallites with random orientation, and the XRD peak intensities would coincide with XRD measurements of a powder sample, as, statistically, all planes would be probed and some plains would reflect X-rays more efficiently than others. Textured samples are polycrystalline samples where the crystallites all have similar orientation, although, with some mosaicity. Finally, a single crystal material (which could be considered similar to a highly textured material) is when the crystallites become very large, or, even a truly single crystal material. The difference of the reciprocal space map between a polycrystalline and a single crystal sample is illustrated in Fig. 4.4. Here, in (a), a single crystal sample is plotted (in reciprocal space), while a polycrystalline sample is shown

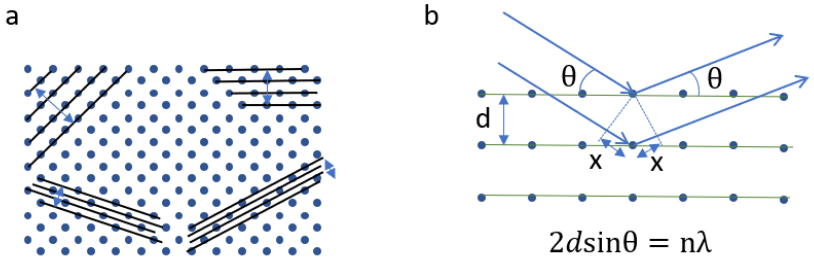

Figure 4.3. (a) The repetitive atomic order in a crystal provides planes with different 'd' spacing which can be imagined as planes that reflects X-rays. (b) Constructive interference will occur when the path difference experienced by parallel X-rays equal a whole number of wavelengths, or when $2x = 2d\sin\theta = n\lambda$.

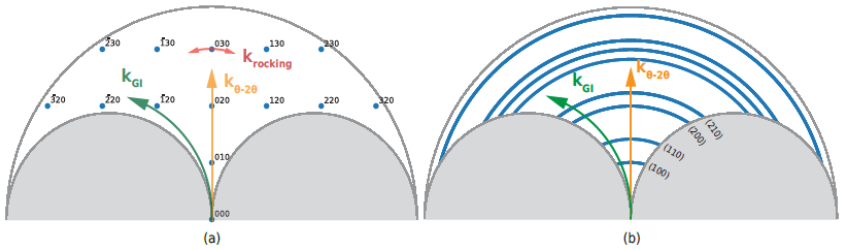

Figure 4.4. A figure illustrating the different XRD scans of (a) a single crystal sample, and (b) a poly crystalline sample, drawn in reciprocal space. The green arrow illustrates GI-XRD scans, the orange curve illustrates $\theta - 2\theta$ (or $\omega - 2\theta$) scans, and red arrows illustrate rocking curves. Figure taken from ref. [94].

in Fig. 4.4 (b). The points in 4.4 (a) indicate where the Laue condition in reciprocal space are satisfied (which is equivalent to Bragg's law in real space). For a polycrystalline sample, these points are 'smeared out' into semi discs with a constant radius. Different XRD scans then map out different directions in reciprocal space; green arrows in Fig. 4.4 indicates grazing incidence XRD scans, orange arrows indicates $\theta - 2\theta$ (or $\omega - 2\theta$) scans, and red arrows indicates rocking curves.

$\theta - 2\theta$ scans are perhaps the most common XRD scan, in which the incoming beam is scanned over a range of incoming angles of incidence and subsequently measured in the specular direction. This scan gives information on which crystal phases are present for both polycrystalline films and highly textured films, see Fig. 4.4. However, $\theta - 2\theta$ scans will only measure planes parallel to the sample surface, i.e., the vertical direction of reciprocal space (orange arrows of Fig. 4.4 (a) and (b)). To reach the remaining peaks for a highly textured sample in reciprocal space, so-called *reciprocal space mapping* can be utilized. For reciprocal space mapping, extra care of the alignment of the sample must be done, which is then often referred to as high resolution XRD (denoted $\omega - 2\theta$ scans) as the slight miscut of substrates relative to the sample surface is considered. For reciprocal space mapping, a combination of sample stage, X-ray source and detector scans are performed in order to map out an *area* in reciprocal space. Reciprocal space mapping gives more information regarding strain and relaxation of the film relative to the substrate and is utilized for highly textured/single crystalline films.

Grazing incidence XRD (GI-XRD) is another type of XRD scan in which the incoming X-ray is kept constant at a low (grazing) angle of incidence, and the detector is scanned about the sample. This type of scan is mostly used to probe polycrystalline samples, as the scanning curve runs the risk of missing any d spacings for a highly textured crystal (see green curve in Fig. 4.4 (a)). A polycrystalline material with random orientation, however, will exhibit semicircles in reciprocal space and thus is probed by the GI-XRD scan (see green curve in Fig. 4.4 (b)).

Another common XRD scan is the rocking curve. This scan is often performed for highly crystalline samples and is done by fixing the angle of incidence and diffraction at an angle where a peak of high intensity from the sample is located, and then rocking the sample stage back and forth. This is effectively scanning the diffraction peak at a semicircle in reciprocal space with a fixed $|\mathbf{k}|$, see red curve Fig. 4.4 (a). This reveals how single crystalline a sample is, as a textured sample will have a broader peak compared to a highly textured or single crystalline sample. The full width half maxima (FWHM) of a peak can be used to compare samples' crystallinity.

In this work, simple $\omega - 2\theta$ scans or GI-XRD scans has mostly been utilized in order to search for phases present in thin film samples, such as CrN vs Cr_2O_3 or anatase TiO_2 vs rutile TiO_2. In paper 1, GI-XRD was used in comparison with $\omega - 2\theta$ scans to probe effects of substrate, laser fluence and oxygen partial pressure on crystal phase, texture, and crystallinity. Rocking curves was used to compare crystallinity of the films to values found in the literature. Similar analysis were done in paper 2 and paper 3.

4.4 Scanning/Transmission Electron Microscopy

Scanning electron microscopy (SEM) and Transmission electron microscopy (TEM) are experimental techniques in which electrons are used instead of photons in order to create an image of a sample. Since the optical (lateral) resolution of an instrument depends on the distance between two distinguishable radiating points, the resolution is directly related to the wavelength of the probe (i.e., Rayleigh criterion). Electrons can be described as waves, with a De Broglie wavelength depending on its energy. When accelerating electrons to 1-30 keV (typical values for a SEM) resolution of $\sim$ 1 nm can be achieved, while TEM typically accelerate electrons up to several 100s of eV with proportionally higher resolution still, and atomic resolution can be obtained. The incoming accelerated electrons interact with the atoms in the sample and, depending on the electron-sample interaction, different properties, such as surface topography, crystal structure, and composition of the sample, can be obtained.

Scanning Electron Microscopy

Scanning electron microscopy (SEM) uses a focused beam of electrons to create an image of the *surface* of a sample and is typically used to analyze the features such as composition, shape and structure. Cross sectional SEM can also be performed by, for instance, cleaving a sample along a substrate's crystal axis and mounting the sample surface plane normal perpendicular to the electron beam.

The scanning electron probe can interact in several ways with the sample, and the different signal sources originate in different physical interaction between the sample and incoming electron beam. These interactions emanate from different depths in the so-called interaction volume, see Fig. 4.5 (a). In this figure, a cross-section of a thin film (blue) is shown, with an electron beam (yellow) scanning the surface, in addition to an interaction volume (shades of green) with different labels of the signal originating from the electron-sample interaction. Secondary electrons are the main source for generating images in SEM and originate from a relatively small region near the surface of the total interaction volume. Secondary electrons are generated when the ionization energy of the material is exceeded by the incoming electrons and electrons from the material leave the material and is collected to form an image. Another useful signal from the electron beam sample interaction is the characteristic X-ray. These X-rays are generated as the electron beam excites electrons from the atom core, and an X-ray is emitted as electrons drop to the atom's original state. These X-rays can then be used to analyze the composition of a sample and to identify different elements present. Other sources from the electron-sample interaction include auger electrons, backscattered electrons, cathodoluminescence, and fluorescent X-rays, see Fig.

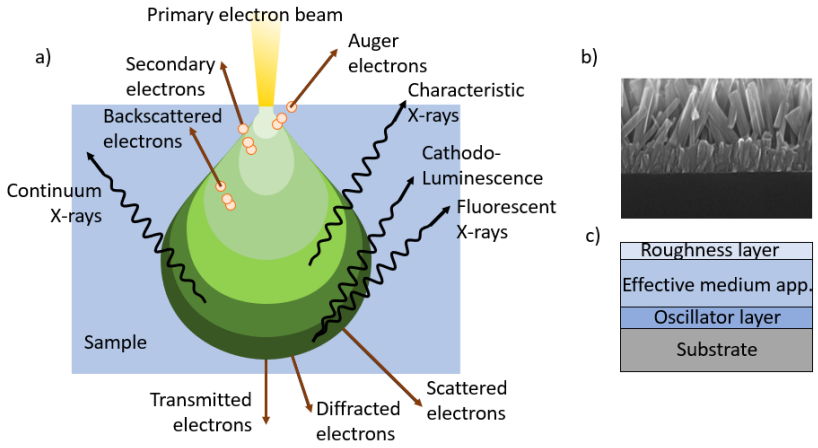

Figure 4.5. a) A schematic illustrating the total interaction volume and denoting the physical origin of different signal sources of information originating from the sample. Image adapted from [96]. b) A SEM image of a MoO_3 sample prepared by PLD. Different 'zones' in the film is observed at different depths of the film. c) An ellipsometric optical model based on the SEM image.

4.5 (a). For a detailed explanation of the SEM instrument and a further description of the different sources originating in the interaction volume, see i.e. [95].

In this thesis, SEM has mostly been utilized for studying the PLD target topography after ablation, thin film surface topography, and as input to optical modeling for ellipsometry by looking at the cross section of thin films to control film thickness. In Fig. 4.5 b), a cross sectional view of a MoO_3 thin film sample grown by PLD is shown. The sample was difficult to model (for ellipsometry) using the expected single thin film layer (in addition to a surface roughness layer). However, as seen from Fig. 4.5 b), the film appears to have different regions where the film is quite dense at the bottom, with a grass like structure growing in the middle region. This observation led us to extend the optical model to include three thin film layers, see Fig. 4.5 c), with an 'optically dense' bottom layer, a porous middle layer, and a surface roughness top layer. This resulted in a much better fit to data, and the determined optical properties are presented in paper 6. Also, characteristic X-rays can be used to estimate sample composition, and this was done for paper 4 for qualitative measurements of Cr doping concentrations.

Transmission Electron Microscopy

Transmission electron microscopy (TEM) is an imaging technique similar to SEM but uses a beam of electrons that *passes through* a sample in order to create an image of the sample. It is used to analyze the structure and composition of samples at the atomic and molecular level. In order to be able to see through a sample with atomic resolution, the sample has to be extremely thin ($\sim$100nm thick) and preferably with a single atomic column of the crystal running parallel to the probing electron beam. This means that TEM measurements are dependent on a specific (and very time consuming) sample preparation procedure in which a small piece of a sample is milled

from the top in order to form a thin slice of sample, which can then be lifted out and mounted on a TEM grid (TEM sample holder). This sample preparation procedure is typically done using an instrument called focused ion beam (FIB). The TEM grid can then be mounted in the TEM and electrons can be passed through the thin sample in order to form an image, so called bright field TEM. TEM has an extremely high (sub nm) resolution due to the large acceleration voltages (high energy -> small De Broglie wavelength) used. Additional information, such as crystallinity, crystal phase, crystal orientation, and composition can be found from TEM measurements, depending on the detectors mounted in the TEM.

In this thesis, others have done the TEM sample preparation and measurements, while I have been a part of the analysis and writing of the results.

5 Summary and Outlook

As mentioned earlier, the aim of this thesis has been to fabricate and optically characterize (by means of spectroscopic ellipsometry) potential deep level intermediate band materials. These deep levels could form either through atomic vacancies/interstitials, i.e. oxygen vacancies in TiO_2 or MoO_3, or by ultra-high doping of materials, like (Cr + N) co-doped TiO_2 or Cr doped ZnS. The main focus for my part has been to fabricate and characterize highly (Cr + N) co-doped TiO_2 made using PLD and to do mainly the optical characterization on the other material systems mentioned above. A summary of the main findings in this thesis is presented in the following sections.

5.1 Summary and main conclusions

5.1.1 Paper 1: Optimizing undoped TiO_2 growth

The starting point of this thesis was to establish TiO_2 growth by PLD at our group's PLD laboratory and studying the resulting film's optical and structural properties in order to prepare for depositing (Cr + N) co-doped TiO_2. This work resulted in a paper draft where we present results from TiO_2 deposited under different laser fluences and oxygen partial pressures, on 4 different substrates, simultaneously, for each deposition. The resulting films were studied by XRD, ellipsometry, AFM and XPS.

In order to study in detail the influence of the substrate on the film growth, we used a special sample holder in which 4 1×1 cm substrates could be deposited on, simultaneously. The substrates studied here were (001) $SrTiO_3$ (STO), (001) $LaAlO_3$ (LAO), (0001) Al_2O_3 (sapphire) and (100) Si (without removing the native oxide). STO and LAO are lattice matched to anatase (001) TiO_2 [97, 98, 99], while sapphire is lattice matched to rutile TiO_2 [100]. Si, with its native oxide, should give for a well-known, inexpensive, and flat surface with a less imposing influence

on the crystalline growth. These experiments were done both in order to study the impact of the substrate and growth conditions for anatase and rutile TiO_2, and also with the aim to fabricate substoichiometric TiO_2.

The main findings from paper 1 was that, in line with literature, we can control the phase and crystallinity by tuning the PLD deposition parameters, like oxygen partial pressure and laser fluence, in addition to the choice of substrate. The paper draft focuses on films deposited on $LaAlO_3$ substrates. For both stoichiometric anatase and rutile, the optical properties were also found to be in line with literature. For sub-stoichiometric rutile, a large sub-bandgap feature was observed for one of the samples. This had a center peak position in line with reported values of blue rutile and is attributed to oxygen vacancies; however, the amplitude observed was much higher for our films than the reported values in literature [101].

5.1.2 Paper 2: Developing a tool for combinatorial PLD films

After obtaining good growth conditions for anatase TiO_2, we developed a new design tool in order to fabricate 1) flat PLD films and 2) hyperdoped PLD films with a continuous compositional spread by so-called natural spread combinatorial PLD. This work resulted in paper 2.

The main finding of this paper was that SIMS measurements confirmed that we have good control of the total material volume fraction of the deposited films, and thickness measurements from ellipsometry confirmed that we now could fabricate 'flat' films by only first depositing a 'calibration plume' film for each target used. The developed tool (python code) is now available online and free to use for designing CCS films and further development.[1]

5.1.3 Papers 3 and 4: Structural and optical properties of (Cr + N) co-doped TiO_2

The previous work (paper 1 and 2) combined, provided the foundation for the (Cr + N) co-doped TiO_2 samples studied in paper 3 and 4. The motivation of (Cr + N) co-doped TiO_2 was that several theoretical articles in the literature predicted an IB to form in this material system. However, the ideal doping concentration is unknown. Therefore, we utilize our continuous compositional spread methodology [83] with previously obtained growth conditions favoring the anatase phase (identified in paper 1) in order to fabricate TiO_2 with a continuous Cr and N co-doping gradient, and study these samples' optical and structural properties.

The main finding in paper 3 was the difficulty in incorporating N into the CCS films. This difficulty was identified as the oxidation of the deposited CrN film. Furthermore, we present the optical and crystalline properties of highly (singly) Cr doped TiO_2, which does not display the sub-bandgap absorption feature expected from DFT calculations. At the end of paper 3, we propose a deposition scheme to overcome the difficulty of N incorporation.

In paper 4, we present the optical and structural properties of the films made in line with the suggestions in paper 3. In these new films, we observed a very interesting, sub-bandgap absorption peak, in line with a theoretically predicted optical response of Cr and N co-doped anatase TiO_2 [32]. This absorption peak below the bandgap was not observed for the singly Cr doped samples. Also, this peak was observed in an area of the film with nano crystalline structure, as opposed

[1] https://github.com/hognely/pyPLD

to similarly doping concentrations with amorphous structure. This seems to indicate that the sub bandgap absorption feature is related to the film crystallinity as well as the composition.

5.1.4 Papers 5, 6 and 7: Optical properties of potential IB materials

Other IB material systems have also been studied in this thesis. Substoichiometric MoO_3 was fabricated both by spin coating technique, in paper 5, and grown using PLD, in paper 6. For the MoO_{3-x} produced by spin coating technique, XRD and AFM indicated a crystalline film with optical properties in line with literature. In addition, an interesting, sub-bandgap absorption peak at $\sim$ 1.3 eV was observed for some of the substoichiometric samples, which may indicate an IB. However, further work needs to be done in order to confirm that an actual IB is formed.

Finally, samples of Cr doped ZnS, grown by a previous PhD candidate, was studied in detail with spectroscopic ellipsometry, which resulted in paper 7. The main finding here was that the films displayed optical properties of ZnS in line with literature. The amount of Cr doping was optically well modeled as ZnS with the inclusion of an Urbach tail, like what was done in ref [90]. This optical model could account for much of the observed below bandgap absorption, but not all. In order to decrease the mean square error (MSE) of the optical model to measured data, a Gaussian oscillator below the bandgap was needed for the most heavily doped samples. Thus, the inclusion of Cr in ZnS produced some states within the bandgap, and further investigations should be done in order to determine if the states form an IB.

5.2 Future work

There is a huge amount of potential future work following this thesis, and I am truly sad to have run out of time. However, if I did have more time, there are a few areas where I would continue this work.

First and foremost, I would continue the work where paper 3 and 4 left off, and try to optimize deposition parameters for (Cr + N) co-doped TiO_2 further. In paper 4, we managed to incorporate large amount of both Cr and N into TiO_2, and identified an interesting sub-bandgap absorption feature. As paper 4 indicate that crystallinity is a crucial factor for the sub-bandgap feature observed, more work should be done in order to increase the crystalline quality. Our first approach in order to incorporate N in our films was to add a capping layer of TiO_2 deposited in an N atmosphere in order to avoid the deposited CrN to oxidize. However, as we found that the capping layer also contributes to smaller grains in addition to promoting the rutile phase, further work should be done in order to investigate if it is possible to incorporate N into the films without the use of a capping layer. This could be achieved by for instance depositing the samples under lower temperatures. In addition, by using lattice matched substrates, further enhancement of the crystallinity might be achieved, as we observed for our undoped TiO_2 films [94].

As our previous work on undoped TiO_2 (summed up in part in paper 1) indicate that the substrate plays a very large role on the crystal phase, a combinatorial (Cr + N) co-doped TiO_2 film with a high doping concentration ($\sim$6-9 at.%) and uniform film thickness, deposited on multiple substrates simultaneously, could make for an interesting comparison between (Cr + N) co-doped anatase (on $LaAlO_3$ and $SrTiO_3$) vs. rutile (on Al_2O_3) TiO_2. By using our in-house python library [83], an optimal film, with little thickness variation and uniform doping concentration across the 1x1

cm substrates, and with the plume center directly over the (rotating) substrates, a very interesting sample series could be made. This could be the next step after deciding whether the TiO_2 capping layer (TiO_2 deposited under N2 atmosphere) is critical for N incorporation.

One material system that I truly wanted to work more with was the reduced MoO_3. The optical properties from the spin-coated films indicated an interesting sub-bandgap absorption feature. However, one of the challenges with the spin coating technique was the difficulty in fabricating thick (> 60 nm) films. PLD on the other hand produces porous, 'grass like' films, as reported in paper 6. One interesting aspect could then be to combine spin coating and PLD, by using the large grained, thin MoO_3 films obtained by spin coating as a 'seed' in order to grow thick, dense MoO_3 films by PLD on top. Even though MoO_3 has other potential challenges as an absorption layer in a solar cell device, like it's very large electron affinity, it is nonetheless an interesting candidate to demonstrate the bulk IBSC concept.

In addition to fabricating new samples, this work has already produced a huge amount of ellipsometric data which have yet to be fully analyzed. Both TiO_2 and MoO_3 should be analyzed in depth as was done for the Cr doped ZnS samples in paper 7; ideally, with the aid of DFT calculations to back up the labeling of critical points. The dielectric function of the hyperdoped TiO_2 samples generally had few sharp features in the optical spectra, so little time was spent on critical point analysis of these samples. However, the measurements of single crystal anatase and rutile reference samples, the thin film samples deposited on LAO, STO, and sapphire in paper 1, and the MoO_3 samples in paper 5, all displayed sharp absorption features in the optical region, ideal for further optical modeling and analysis. Sadly, time ran out before I managed to finish this work.

I have now spent several years working on this PhD thesis, and still, I truly wished I had more time. There is just so much more research to be done!

Bibliography

[1] UNEP. *Emission gap Report 2022; the closing window*. 2022. URL: https://www.unep.org/resources/emissions-gap-report-2022 (visited on 11/11/2022).

[2] Sarah R Kurtz et al. "Revisiting the terawatt challenge". In: *MRS Bulletin* 45.3 (2020), pp. 159–164.

[3] Xiaoting Wang and Allen Barnett. "The evolving value of photovoltaic module efficiency". In: *Applied Sciences* 9.6 (2019), p. 1227.

[4] William Shockley and Hans J Queisser. "Detailed balance limit of efficiency of p-n junction solar cells". In: *Journal of applied physics* 32.3 (1961), pp. 510–519.

[5] Jonas Kristiansen Nøland et al. "Spatial energy density of large-scale electricity generation from power sources worldwide". In: *Scientific Reports* 12.1 (2022), pp. 1–26.

[6] Antonio Luque and Antonio Marti. "Increasing the efficiency of ideal solar cells by photon induced transitions at intermediate levels". In: *Physical review letters* 78.26 (1997), p. 5014.

[7] Antonio Luque and Antonio Marti. "A metallic intermediate band high efficiency solar cell". In: *Progress in Photovoltaics: Research and Applications* 9.2 (2001), pp. 73–86.

[8] Antonio Luque, Antonio Marti, and Colin Stanley. "Understanding intermediate-band solar cells". In: *Nature Photonics* 6.3 (2012), pp. 146–152.

[9] E López et al. "Demonstration of the operation principles of intermediate band solar cells at room temperature". In: *Solar Energy Materials and Solar Cells* 149 (2016), pp. 15–18.

[10] Takeyoshi Sugaya et al. "Miniband formation in InGaAs quantum dot superlattice". In: *Applied Physics Letters* 97.4 (2010), p. 043112.

[11] Nair López et al. "Engineering the electronic band structure for multiband solar cells". In: *Physical Review Letters* 106.2 (2011), p. 028701.

[12] J Olea et al. "Room temperature photo-response of titanium supersaturated silicon at energies over the bandgap". In: *Journal of Physics D: Applied Physics* 49.5 (2016), p. 055103.

[13] Antonio Luque et al. "Intermediate bands versus levels in non-radiative recombination". In: *Physica B: Condensed Matter* 382.1-2 (2006), pp. 320–327.

[14] Jacob J Krich, Bertrand I Halperin, and Alan Aspuru-Guzik. "Nonradiative lifetimes in intermediate band photovoltaics—absence of lifetime recovery". In: *Journal of Applied Physics* 112.1 (2012), p. 013707.

[15] JT Sullivan et al. "Methodology for vetting heavily doped semiconductors for intermediate band photovoltaics: A case study in sulfur-hyperdoped silicon". In: *Journal of Applied Physics* 114.10 (2013), p. 103701.

[16] Joseph T Sullivan et al. “Targeted search for effective intermediate band solar cell materials”. In: *IEEE Journal of Photovoltaics* 5.1 (2014), pp. 212–218.

[17] Inigo Ramiro et al. “Review of experimental results related to the operation of intermediate band solar cells”. In: *IEEE Journal of Photovoltaics* 4.2 (2014), pp. 736–748.

[18] SA Blokhin et al. “AlGaAs/GaAs photovoltaic cells with an array of InGaAs QDs”. In: *Semiconductors* 43.4 (2009), pp. 514–518.

[19] K Sablon et al. “GaAs quantum dot solar cell under concentrated radiation”. In: *Applied Physics Letters* 107.7 (2015), p. 073901.

[20] Juan Villa et al. “Contribution to the study of sub-bandgap photon absorption in quantum dot InAs/AlGaAs intermediate band solar cells”. In: *IEEE Journal of Photovoltaics* 11.2 (2020), pp. 420–428.

[21] Iñigo Ramiro and Antonio Marti. “Intermediate band solar cells: Present and future”. In: *Progress in Photovoltaics: Research and Applications* 29.7 (2021), pp. 705–713.

[22] Tony Jones, John Edwards, and Jani Kallioinen. “Titanium compounds, inorganic”. In: *Kirk-Othmer Encyclopedia of Chemical Technology* (2000), pp. 1–76.

[23] Taro Hitosugi et al. “Properties of TiO2-based transparent conducting oxides”. In: *Physica status solidi (a)* 207.7 (2010), pp. 1529–1537.

[24] Amy L Linsebigler, Guangquan Lu, and John T Yates Jr. “Photocatalysis on TiO2 surfaces: principles, mechanisms, and selected results”. In: *Chemical reviews* 95.3 (1995), pp. 735–758.

[25] Li-Wu Zhang, Hong-Bo Fu, and Yong-Fa Zhu. “Efficient TiO2 photocatalysts from surface hybridization of TiO2 particles with graphite-like carbon”. In: *Advanced Functional Materials* 18.15 (2008), pp. 2180–2189.

[26] Kazuya Nakata and Akira Fujishima. “TiO2 photocatalysis: Design and applications”. In: *Journal of photochemistry and photobiology C: Photochemistry Reviews* 13.3 (2012), pp. 169–189.

[27] Fengcheng Wu et al. “Quantum efficiency of intermediate-band solar cells based on non-compensated np codoped TiO2”. In: *The Journal of chemical physics* 137.10 (2012), p. 104702.

[28] H Tang et al. “Electrical and optical properties of TiO2 anatase thin films”. In: *Journal of applied physics* 75.4 (1994), pp. 2042–2047.

[29] Mingchun Xu et al. “Photocatalytic activity of bulk TiO 2 anatase and rutile single crystals using infrared absorption spectroscopy”. In: *Physical Review Letters* 106.13 (2011), p. 138302.

[30] Jinfeng Zhang et al. “New understanding of the difference of photocatalytic activity among anatase, rutile and brookite TiO2”. In: *Physical Chemistry Chemical Physics* 16.38 (2014), pp. 20382–20386.

[31] David O Scanlon et al. “Band alignment of rutile and anatase TiO2”. In: *Nature materials* 12.9 (2013), pp. 798–801.

[32] Matiullah Khan et al. “Ab-initio calculations of synergistic chromium–nitrogen codoping effects on the electronic and optical properties of anatase TiO2”. In: *Vacuum* 92 (2013), pp. 32–38.

[33] Qingsen Meng et al. “Understanding electronic and optical properties of anatase TiO 2 photocatalysts co-doped with nitrogen and transition metals”. In: *Physical Chemistry Chemical Physics* 15.24 (2013), pp. 9549–9561.

[34] Long Lin et al. “Density functional study on electronic structures and magnetic properties in (Cr, N) co-doped anatase TiO2”. In: *Materials Research Express* 6.11 (2019), p. 116332.

[35] Veysel Celik and Ersen Mete. “Electronic and optical properties of Cr and Cr–N doped anatase TiO2 from screened Coulomb hybrid calculations”. In: *Journal of Physics: Condensed Matter* 25.36 (2013), p. 365502.

[36] Renhui Zhang et al. “Optical properties of N and transition metal R (R= V, Cr, Mn, Fe, Co, Ni, Cu, and Zn) codoped anatase TiO2”. In: *Physica B: Condensed Matter* 407.14 (2012), pp. 2709–2715.

[37] K Kollbek et al. “Optical and electrical properties of Ti (Cr) O2: N thin films deposited by magnetron co-sputtering”. In: *Applied Surface Science* 380 (2016), pp. 73–82.

[38] Jinmin Fan et al. “Synthesis of Cr, N-codoped titania nanotubes and their visible-light-driven photocatalytic properties”. In: *Applied Surface Science* 324 (2015), pp. 691–697.

[39] C-C Pan and Jeffrey Wu. “Visible-light response Cr-doped TiO {sub 2-X} N {sub X} photocatalysts”. In: *Materials Chemistry and Physics* 100 (2006).

[40] Yuan Li et al. “Comparing Cr, and N only doping with (Cr, N)-codoping for enhancing visible light reactivity of TiO2”. In: *Applied Catalysis B: Environmental* 110 (2011), pp. 148–153.

[41] Raúl Gago et al. “Phase selectivity in Cr and N co-doped TiO2 films by modulated sputter growth and post-deposition flash-lamp-annealing”. In: *Coatings* 9.7 (2019), p. 448.

[42] C Parks Cheney et al. “Origins of electronic band gap reduction in Cr/N codoped TiO 2”. In: *Physical review letters* 112.3 (2014), p. 036404.

[43] Zhengwang Cheng et al. “Electronic properties of Cr-N codoped rutile TiO2 (110) thin films”. In: *Surface Science* 666 (2017), pp. 84–89.

[44] Po-Sheng Wang et al. “Enhancement of current injection in organic light emitting diodes with sputter treated molybdenum oxides as hole injection layers”. In: *Applied Physics Letters* 98.17 (2011), p. 80.

[45] J Jaćimović et al. “Electrical property measurements of Cr-N codoped TiO2 epitaxial thin films grown by pulsed laser deposition”. In: *Applied Physics Letters* 102.17 (2013), p. 172108.

[46] ND Bassim et al. “Model, prediction, and experimental verification of composition and thickness in continuous spread thin film combinatorial libraries grown by pulsed laser deposition”. In: *Review of Scientific Instruments* 78.7 (2007), p. 072203.

[47] Paul J McGinn. “Thin-film processing routes for combinatorial materials investigations—a review”. In: *ACS Combinatorial Science* 21.7 (2019), pp. 501–515.

[48] Martin L Green, Ichiro Takeuchi, and Jason R Hattrick-Simpers. “Applications of high throughput (combinatorial) methodologies to electronic, magnetic, optical, and energy-related materials”. In: *Journal of Applied Physics* 113.23 (2013), 9_1.

[49] H Sakama et al. “Epitaxial growth of anatase TiO2 thin films on LaAlO3 (100) prepared using pulsed laser deposition”. In: *Thin Solid Films* 515.2 (2006), pp. 535–539.

[50] T Nambara et al. “Preparation of strain-included rutile titanium oxide thin films and influence of the strain upon optical properties”. In: *Thin Solid Films* 515.5 (2007), pp. 3096–3101.

[51] Nadia Sbai et al. “Structural, optical, and electrical properties of epitaxial titanium oxide thin films on LaAlO 3 substrate”. In: *Journal of Applied Physics* 104.3 (2008), p. 033529.

[52] Barbara Grzybowska-Świerkosz. “Thirty years in selective oxidation on oxides: what have we learned?” In: *Topics in Catalysis* 11.1 (2000), pp. 23–42.

[53] Thorsten Ressler et al. “Bulk structural investigation of the reduction of MoO3 with propene and the oxidation of MoO2 with oxygen”. In: *Journal of Catalysis* 210.1 (2002), pp. 67–83.

[54] S Barazzouk, RP Tandon, and S Hotchandani. “MoO3-based sensor for NO, NO2 and CH4 detection”. In: *Sensors and Actuators B: Chemical* 119.2 (2006), pp. 691–694.

[55] CV Ramana et al. “Electrochemical properties of sputter-deposited MoO3 films in lithium microbatteries”. In: *Journal of Vacuum Science & Technology A: Vacuum, Surfaces, and Films* 30.4 (2012), p. 04D105.

[56] Tao He and Jiannian Yao. “Photochromism of molybdenum oxide”. In: *Journal of Photochemistry and Photobiology C: Photochemistry Reviews* 4.2 (2003), pp. 125–143.

[57] JN Yao, K Hashimoto, and A Fujishima. “Photochromism induced in an electrolytically pretreated Mo03 thin film by visible light”. In: *Nature* 355.6361 (1992), pp. 624–626.

[58] Lars Kihlborg. “Least squares refinement of crystal structure of molybdenum trioxide”. In: *Arkiv for Kemi* 21.4 (1963), p. 357.

[59] LA Bursill. “On the relation between molybdenum trioxide and rhenium trioxide type crystal structures”. In: *Acta Crystallographica Section A: Crystal Physics, Diffraction, Theoretical and General Crystallography* 29.1 (1973), pp. 28–30.

[60] EM McCarron. “β-MoO3: a metastable analogue of WO3”. In: *Journal of the Chemical Society, Chemical Communications* 4 (1986), pp. 336–338.

[61] Stig Asbrink and Lars Kihlsburg. “A Study of the Crystal Symmetry and Structure of Orthorhombic”. In: *Acta Chem. Sound* 18.6 (1964).

[62] Arne Magneli. “The Crystal Structures of Mo9O26 (Beta’-Molybdenum Oxide) and MO8O23 (Beta-Molybdenum Oxide)”. In: *Acta Chemica Scandinavica* 2.5-6 (1948), pp. 501–517.

[63] M Sato, M Onoda, and Y Matsuda. “Structural transitions in MonO3n-1 (n=9 and 10)”. In: *Journal of Physics C: Solid State Physics* 20.29 (1987), p. 4763.

[64] LARS Kihlborg et al. “The crystal structure of Mo17O47”. In: *Acta Chem. Scand* 14.7 (1960).

[65] Theodoros A Papadopoulos et al. “Nature of the Interfaces Between Stoichiometric and Under-Stoichiometric MoO3 and 4, 4’-N, N’-dicarbazole-biphenyl: A Combined Theoretical and Experimental Study”. In: *Advanced Functional Materials* 23.48 (2013), pp. 6091–6099.

[66] CZ Chen, Y Li, and XD Tang. “Evidence of oxygen vacancy and possible intermediate gap state in layered α-MoO3 single-crystal nanobelts”. In: *Physica B: Condensed Matter* 481 (2016), pp. 192–196.

[67] Katherine Inzani et al. “Electronic properties of reduced molybdenum oxides”. In: *Physical chemistry chemical physics* 19.13 (2017), pp. 9232–9245.

[68] Katherine Inzani et al. “Progression of reduction of MoO3 observed in powders and solution-processed films”. In: *Thin Solid Films* 626 (2017), pp. 94–103.

[69] C Tablero. “Optoelectronic properties of Cr-substituted II–VI semiconductors”. In: *Computational materials science* 37.4 (2006), pp. 483–490.

[70] C Tablero. “Effects of the impurity–host interactions on the nonradiative processes in ZnS: Cr”. In: *Journal of Applied Physics* 108.9 (2010), p. 093114.

[71] Mohammadreza Nematollahi et al. “Molecular beam and pulsed laser deposition of ZnS: Cr for intermediate band solar cells”. In: *Solar Energy Materials and Solar Cells* 141 (2015), pp. 322–330.

[72] Mohammadreza Nematollahi et al. “Pulsed laser ablation and deposition of ZnS: Cr”. In: *Thin Solid Films* 590 (2015), pp. 28–32.

[73] Mohammadreza Nematollahi et al. “Compositional and structural properties of pulsed laser-deposited ZnS: Cr films”. In: *Applied Physics A* 122.2 (2016), pp. 1–11.

[74] Donald L Smith and David W Hoffman. “Thin-film deposition: principles and practice”. In: *Physics Today* 49.4 (1996), p. 60.

[75] Robert Eason. *Pulsed laser deposition of thin films: applications-led growth of functional materials*. John Wiley & Sons, 2007.

[76] Dave HA Blank, Matthijn Dekkers, and Guus Rijnders. “Pulsed laser deposition in Twente: from research tool towards industrial deposition”. In: *Journal of physics D: applied physics* 47.3 (2013), p. 034006.

[77] MD Nguyen et al. “Wafer-scale growth of highly textured piezoelectric thin films by pulsed laser deposition for micro-scale sensors and actuators”. In: *Journal of physics: Conference series*. Vol. 922. 1. IOP Publishing. 2017, p. 012022.

[78] Zakhar Vakulov et al. “Towards scalable large-area pulsed laser deposition”. In: *Materials* 14.17 (2021), p. 4854.

[79] John A Thornton. “Influence of apparatus geometry and deposition conditions on the structure and topography of thick sputtered coatings”. In: *Journal of Vacuum Science and Technology* 11.4 (1974), pp. 666–670.

[80] Norbert Kaiser. “Review of the fundamentals of thin-film growth”. In: *Applied optics* 41.16 (2002), pp. 3053–3060.

[81] R Messier, AP Giri, and RA Roy. “Revised structure zone model for thin film physical structure”. In: *Journal of Vacuum Science & Technology A: Vacuum, Surfaces, and Films* 2.2 (1984), pp. 500–503.

[82] André Anders. “A structure zone diagram including plasma-based deposition and ion etching”. In: *Thin Solid Films* 518.15 (2010), pp. 4087–4090.

[83] Hogne Lysne et al. “Improved methods for design of PLD and combinatorial PLD films”. In: *Journal of applied Physics* 132 (2022), p. 125301.

[84] Hogne Lysne. “Design and fabrication of (Cr+N) co-doped TiO_2 films with a continuous compositional spread”. PhD thesis. NTNU, 2023.

[85] Mauro Sardela. *Practical materials characterization*. Springer, 2014.

[86] Hiroyuki Fujiwara and Robert W Collins. *Spectroscopic ellipsometry for photovoltaics*. Vol. 1. Springer, 2018.

[87] Iryna Valyukh et al. “Spectroscopic ellipsometry characterization of electrochromic tungsten oxide and nickel oxide thin films made by sputter deposition”. In: *Solar Energy Materials and Solar Cells* 94.5 (2010), pp. 724–732.

[88] Sadao Adachi. *Optical properties of crystalline and amorphous semiconductors: Materials and fundamental principles*. Springer Science & Business Media, 2012.

[89] Hiroyuki Fujiwara. *Spectroscopic ellipsometry: principles and applications*. John Wiley & Sons, 2007.

[90] Kiran Ghimire et al. “Optical properties of single-crystal Gd3Ga5O12 from the infrared to ultraviolet”. In: *physica status solidi (b)* 252.10 (2015), pp. 2191–2198.

[91] P Petrik et al. “Comparative study of surface roughness measured on polysilicon using spectroscopic ellipsometry and atomic force microscopy”. In: *Thin Solid Films* 315.1-2 (1998), pp. 186–191.

[92] H Fujiwara et al. “Assessment of effective-medium theories in the analysis of nucleation and microscopic surface roughness evolution for semiconductor thin films”. In: *Physical Review B* 61.16 (2000), p. 10832.

[93] Daniel Franta and Ivan Ohlidal. “Influence of lateral dimensions of the irregularities on the optical quantities of rough surfaces”. In: *Journal of Optics A: Pure and Applied Optics* 8.9 (2006), p. 763.

[94] Marcus Grand Michaelsen. “Pulsed Laser Deposited TiO2: X-ray Diffraction and Raman Spectroscopy Studies”. MA thesis. NTNU, 2022.

[95] Joseph I Goldstein et al. *Scanning electron microscopy and X-ray microanalysis*. Springer, 2017.

[96] Ponor. *Electron-matter interaction volume and various types of signal generated*. 2020. URL: https://commons.wikimedia.org/wiki/File:Electron-matter_interaction_volume_and_various_types_of_signal_generated_-_v2.svg (visited on 10/28/2022).

[97] RJ Kennedy and PA Stampe. “The influence of lattice mismatch and film thickness on the growth of TiO2 on LaAlO3 and SrTiO3 substrates”. In: *Journal of Crystal Growth* 252.1-3 (2003), pp. 333–342.

[98] M Zhu et al. “A high-resolution transmission electron microscopy investigation of the microstructure of TiO2 anatase film deposited on LaAlO3 and SrTiO3 substrates by laser ablation”. In: *Thin Solid Films* 441.1-2 (2003), pp. 140–144.

[99] BH Park et al. “Role of atomic arrangements at interfaces on the phase control of epitaxial TiO 2 films”. In: *Applied physics letters* 80.7 (2002), pp. 1174–1176.

[100] MR Bayati et al. “Structure–property correlation in epitaxial (2 0 0) rutile films on sapphire substrates”. In: *Journal of Solid State Chemistry* 187 (2012), pp. 231–237.

[101] Vyacheslav N Kuznetsov and Nick Serpone. “On the origin of the spectral bands in the visible absorption spectra of visible-light-active TiO2 specimens analysis and assignments”. In: *The Journal of Physical Chemistry C* 113.34 (2009), pp. 15110–15123.

Part II

Publications

Paper 1

Thomas Brakstad, Marina Jorge, Morten Kildemo and Turid Reenaas

"Structural, chemical, and optical properties of TiO_2 fabricated by PLD"

Paper draft

Paper 2

Hogne Lysne, Thomas Brakstad, Morten Kildemo, and Turid Reenaas

"Improved methods for design of PLD and combinatorial PLD films"

Journal of Applied Physics **132** (2022), p. 125301

Journal of Applied Physics METHOD scitation.org/journal/jap

Improved methods for design of PLD and combinatorial PLD films

Cite as: J. Appl. Phys. **132**, 125301 (2022); doi: 10.1063/5.0105298
Submitted: 23 June 2022 · Accepted: 28 August 2022 ·
Published Online: 22 September 2022

Hogne Lysne,[a] Thomas Brakstad,[b] Morten Kildemo,[c] and Turid Reenaas[d]

AFFILIATIONS

Department of Physics, Norwegian University of Science and Technology (NTNU), N-7491 Trondheim, Norway

[a]hogne.lysne@ntnu.no
[b]thomas.brakstad@ntnu.no
[c]morten.kildemo@ntnu.no
[d]**Author to whom correspondence should be addressed:** turid.reenaas@ntnu.no

ABSTRACT

Pulsed laser deposition (PLD) is a powerful technique for prototyping thin film materials, both single component (single composition) films and films with a varying composition (e.g., lateral continuous compositional spread, CCS). In this work, we improve one of the simulation methods used to design the deposition of PLD films: We extend the mathematical model for the material spread on the substrate, $T_1(x, y)$, for each laser pulse hitting the target, and we use a more accurate method to determine $T_1(x, y)$ experimentally. The deposition of the material on the substrate is simulated by repetitively adding $T_1(x, y)$, from one or more targets, at the selected location on the substrate. Using the new model, a high agreement between the simulated and grown films' thickness and composition across the substrate was obtained. The basis for the high agreement is the use of variable angle spectroscopic ellipsometry to carefully determine $T_1(x, y)$ by measuring at 794 locations on the 50.8 mm (2 in.) diameter substrates. Factors, such as variation in optical properties and porosity across the plume/calibration films, were considered in the determination of the thicknesses. As test cases, we simulated and deposited (single component) TiO_2 thin films and (CCS) TiO_2 films doped with Cr and N, deposited on 50.8 mm diameter Si wafers. The modeling and simulations are implemented in an open-source Python library, pyPLD.

I. INTRODUCTION

Pulsed laser deposition (PLD) has proven to be a powerful tool for prototyping a wide range of materials.[1–4] In PLD, material is evaporated (or ablated) from a target using a pulsed laser. The ablated material is ejected from the target in a highly directional plume. The material is, thereby transferred to a substrate where a thin film is formed, as illustrated in Fig. 1(a). A challenge in PLD is that the lateral size of the plume of the ablated material is often smaller than the width of the substrate, and this limits the spread of the deposited material onto the substrate.[5] This can result in a non-uniform film thickness [see Fig. 1(a)]. A more uniform film thickness can be achieved through optimization of the lateral substrate position relative to the plume center[6,7] or by laser beam rastering on the target.[6–10] For rastering systems, the laser spot is moved on the target relative to the substrate, and this moves the origin of the plume, resulting in a movement of the plume over the substrate during deposition. For non-rastering systems, the laser spot is fixed, and thus, the plume origin is fixed.

Combinatorial thin film deposition is a methodology for making thin films with a variation of properties laterally across the film using both PLD and other deposition techniques as a starting point.[11,12] Often, the composition is varied, resulting in films with a continuous compositional spread (CCS), but other parameters, such as substrate temperature, can be varied as well.[11] The fabrication of CCS films speeds up the screening process when searching for materials with a set of desired properties. A wide range of combinatorial PLD (c-PLD) techniques have been engineered,[13–22] and here, we will focus on natural spread c-PLD, nc-PLD, where the limited size of the plume is the basis of achieving the desired compositional spread. nc-PLD is a simple technique compared to many other c-PLD techniques and just requires the PLD setup to have the ability to swap targets and to rotate the substrate.[21] In Fig. 1(b),

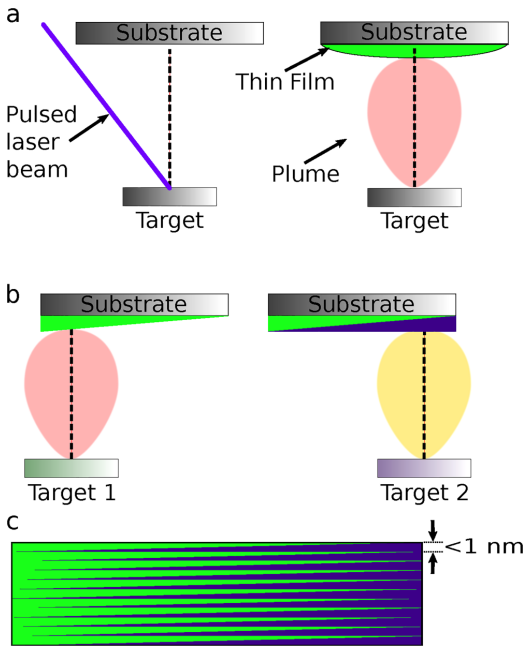

FIG. 1. (a) The basic steps in PLD: (Left side) First, a pulsed laser hits the target. (Right side) Second, a plume is formed, and the material in the plume deposits onto the substrate (green layer). Notice the non-uniformity of the film thickness. The material deposited from a single pulse is denoted $T_1(x, y)$. (b) In natural spread combinatorial PLD (nc-PLD), materials from two (or more) different targets are deposited on different locations onto the substrate. The natural, limited, spread of material from each plume then results in a continuous compositional spread between the locations of the two plumes. (c) The process steps in (b) are repeated to build up a film of the desired thickness.

nc-PLD is shown schematically. First, Target 1 is ablated, and a non-uniform (sub nm thickness) film of this material (shown in green in the figure) is deposited onto the substrate. Subsequently, the substrate is moved, the target is replaced by another target, and material from Target 2 is ablated and deposited (shown as purple). These steps are repeated to build up the CCS film layer by layer, as shown schematically in Fig. 1(c). If desired, additional targets and substrate positions can be used.

To tailor the film's compositional spread and/or the film thickness variation across a substrate, one must be able to simulate the deposition of material for both conventional PLD (for single composition films) and nc-PLD (for CCS films). The material spread on the substrate in conventional PLD and various c-PLD rastering techniques has been successfully simulated.[6,8–10] Note that these simulations are not atomistic simulations of the interactions between atoms and ions in the plume and the ambient gas, or the interactions with the substrate and in the growing film, but a simulation of the amount of material depositing on the substrate for each laser pulse. Nevertheless, such non-atomistic simulations are very useful as an aid in the design of PLD and c-PLD (film deposition) process steps, and the current work aims to improve the existing design tools. For atomistic simulations, the reader is referred to Refs. 23–26.

For basic PLD setups (without automated laser rastering or substrate movement except for substrate rotation), Guilfoyle *et al.*[6] simulated the PLD process by performing a numerical integration of an analytical model for the material deposited for each laser pulse/each plume. They demonstrate how offsetting the plume from the substrate rotational axis results in a more uniform film thickness over a larger area.

Bassim *et al.*[14,22] have simulated the material spread and composition of CCS films grown by nc-PLD. They consider a setup with three targets, combined with a substrate rotation of 120° between the ablation/deposition from each target. The initial step in the simulation of the growth is to determine the (natural) material spread on the substrate for each of the targets to be used. The material spread will depend on the deposition parameters, such as laser fluence, laser spot size, background gas pressure, etc. Thus, a series of calibration samples (later referred to as plume films) must be made for each target/each plume, where the relevant deposition parameters are used, and the substrate is not rotated. The thickness variation, $T(x, y)$, across the substrate of these single component/composition films is then measured and fitted to the following expression:[1]

$$T(x,y) = T_0 \left(\frac{z}{\sqrt{z^2 + (x - x_p)^2}} \right)^n \left(\frac{z}{\sqrt{z^2 + (y - y_p)^2}} \right)^m, \quad (1)$$

where T_0 is the maximum thickness of the film, z is the distance between the target and the substrate, and x_p and y_p are the coordinates of the center of the plume relative to the substrate center ($x = y = 0$, where $T = T_0$). m and n are fitting parameters describing the rate of decrease in the thickness of the calibration sample. Bassim *et al.* then simulated the final thickness and compositional spread of their desired CCS films by summing the contribution per pulse from each of the three components/targets. Bassim *et al.* assume that the volume of the material deposited in the multi-component CCS film is equal to the volume deposited in the single component calibration films. They also seem to assume that the sticking coefficient does not change with time as the film thickness increases neither in the calibration films nor the CCS films. Snyder *et al.*[21] explicitly assume a constant (unity) sticking coefficient in their simulations of CCS films. Although these assumptions might be incorrect in some cases, the match between their simulated and deposited films indicates that the assumptions are valid in their cases.

A critical issue in this type of CCS-film simulations is the accuracy of the experimentally determined thickness variation for the calibration samples. Bassim *et al.* obtained thickness maps from reflectometry measurements, but they used reference data for the optical properties (the complex refractive index, $n^* = n + ik$) from the literature instead of measuring them. This results in a reduced

TABLE I. List of samples, including the nominal number of laser pulses, N_p, the rotational speed of the substrate, ω, and the position of the plume center, (x_p, y_p), relative to the substrate center during deposition, for the plume films (TiO_2-P and CrN-P) and the "flat" TiO_2 films. The TiO_2 films with "FR" in the label were deposited ensuring the substrate is "fully rotated," while "NFR" denotes "not full rotations." Photographs of some of the films can be seen in Fig. 2, and thickness maps will be presented later in the paper (in Figs. 5 and 8). Also listed are the maximum T_{max} and minimum T_{min} thicknesses for each film, determined by ellipsometry as described in the text. For the two plume films, T_{max} is at location 1 indicated in Fig. 2(a) and T_{min} is near the edge of the substrate in the lower left quadrant. For the flat films, T_{max} is at the substrate center for TiO_2-FR-0 and TiO_2-FR-3 and at the edge for TiO_2-FR-1 and TiO_2-FR-2.

Sample	N_p	ω (deg/s)	x_p (cm)	y_p (cm)	T_{max} (nm)	T_{min} (nm)
TiO_2-P	15 000	0	0.33	1.63	533	31
CrN-P	40 000	0	0.33	1.63	156	18
TiO_2-FR-0	18 000	29	0.33	1.63	277	130
TiO_2-FR-1	36 000	29	0.0	3.0	200	179
TiO_2-FR-2	36 000	29	0.0	2.8	206	193
TiO_2-FR-3	18 000	29	0.0	2.5	148	124
TiO_2-NFR	15 000	29	1.0	2.4	114	101

accuracy for the thickness if n^* for their sample deviates from the literature data and/or if n^* varies across the substrate.

To improve the accuracy, Bassim *et al.* suggest using ellipsometry to measure the actual complex refractive index, and this was done by Socol *et al.*[27] and Barron *et al.*[15] However, Barron *et al.*[15] obtained n^* for reference films, and not for the actual films used for the determination of the material spread, and Socol *et al.*[27] used a less extensive modeling of the material spread as compared to Bassim *et al.* As an alternative approach, Snyder *et al.*[21] determined the thickness variation using a (time consuming and destructive) patterned selective etch and direct profilometer measurements of the thickness, while using a similar simulation approach as Bassim *et al.*[14]

In this paper, we extend on the simulation of PLD done by Guilfoyle *et al.*[6] and Bassim *et al.*[14] for both conventional PLD and nc-PLD, respectively, by making very accurate determinations of the thickness variation in the calibration samples as well as in the final films. This was achieved using mapping variable angle spectroscopic ellipsometry (VASE), which can be used to accurately determine the local thickness across thin films, or stacks of films, down to 0.1 Å accuracy.[28] The high accuracy in the thickness determination enabled us to extend the model in Eq. (1), resulting in a very high agreement between the simulated and measured material spread. In the process, we have established a flexible simulation tool for PLD deposition, where we keep track of the material deposited for every laser pulse, $T_1(x, y)$. This results in information about the film thickness and composition across the (50.8 mm diameter) substrate. The simulations serve as a design tool to determine the locations of the plumes on the substrate and the sequence of laser pulses hitting each of the targets to be used. This is a precise, straightforward, and more realistic simulation of the deposition compared to the simulations of Guilfoyle *et al.*[6] and is very similar to the approach of Bassim *et al.*

In this paper, two categories of films were made: calibration films to obtain $T_1(x, y)$ and films designed through the simulations to demonstrate usability of the simulations to design PLD films. We assume that $T_1(x, y)$ can be expressed as $T_1(x, y) = T(x, y)/N_p$, where N_p is the number of pulsed used to deposit the calibration film. This means that we assume that the sticking coefficient and the volume of the deposited material are independent of the film thickness and the substrate/the growing film's surface and a constant laser fluence. The validity of the assumptions is addressed when the simulated and measured film thicknesses are compared. However, as the aim of this work is to develop a design tool for PLD and not to simulate the actual film growth, it is not crucial that all assumptions are fully valid at this stage. It should be noted that non-constant values for the sticking coefficient, volume, and laser fluence easily can be implemented in the simulation method to achieve an even better match between simulated and measured thicknesses when desired.

The resulting simulation scheme developed in this work is implemented in a Python library, pyPLD, that will be made accessible online.

In Sec. II, we present the experimental details for the PLD deposition and the characterization of the films. In Sec. III, we describe how the thickness is determined using VASE, and in Sec. IV, we present how we model the material distribution resulting from every laser pulse on the target, $T_1(x, y)$. The simulation procedure and assumptions are described in Sec. V. In Sec. VI, we present the PLD simulations of designed single component/composition "flat" (TiO_2) films where we optimize for thickness uniformity. In Sec. VII, we present simulations of a two-component CCS film (Cr and N doped TiO_2, using a CrN and a TiO_2 target) and compare with measured thickness and composition. In Sec. VIII, we present the pyPLD simulation tool, and finally, in Sec. IX, the conclusions are presented.

II. EXPERIMENTAL DETAILS

A. PLD deposition

The film deposition took place in a Neocera PLD system, with a base pressure of 10^{-9}–10^{-10} Torr. During deposition, the chamber was back-filled with oxygen to a pressure of 1.3×10^{-2} Torr. The films were deposited on 50.8 mm (2 in.) diameter p-type Si(100) wafers, kept at ~700 °C during deposition. Prior to deposition, the wafers were cleaned with acetone (VLSI grade) and isopropanol (SLSI grade), meaning that the native oxide is not removed from the Si wafers. The distance between the target and the substrate was (4.40 ± 0.05) cm. A KrF excimer laser

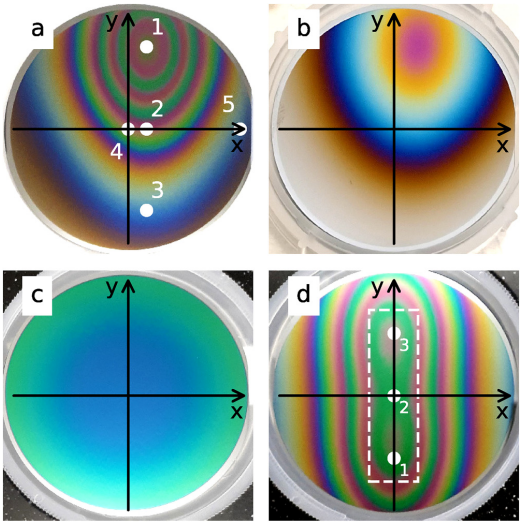

FIG. 2. Photographs of the (a) TiO_2 plume film (TiO_2-P), (b) the CrN plume film (CrN-P), (c) a "flat" TiO_2 film (TiO_2-FR-1), and (d) the CCS film of Cr and N doped TiO_2. Since the films are highly transparent, the thickness variation is easily seen by the naked eye in the interference fringes that occur due to the thickness being on the order of the wavelength of visible light. The white dots in (a) indicate where AFM images were taken (positions 1–3) and the initial VASE measurements (positions 1, 4, and 5). The plume films are the thickest at position 1 indicated in (a). The thickness was mapped for 794 points across the plume films and the flat films. The white dashed rectangle in (d) indicates the area on the substrate where the film is tailored to be rather flat and to have an increasing Cr content along the y-axis, ranging from 2 at. % at $y = -1.75$ cm to 8 at. % in at $y = +1.75$ cm. The white dots in (d) indicate where AFM images were taken.

(Coherent COMPexpro 110, 248 nm, 20 ns FWHM) was operated at 5 Hz to ablate a TiO_2 target (PI-KEM, 99.9% purity) or 10 Hz to ablate a CrN target (Stanford Advanced Materials, 99.5% purity) with a fluence of $\sim 1.5\,J/cm^2$ ($\sim 29.4\,MW/cm^2$). The laser spot size on the targets was approximately $1 \times 2\,mm^2$. The laser window was not cleaned between depositions, and thus, the actual laser fluence on the target was slowly reduced as more depositions were performed. This resulted in a reduction of the deposition rate up to 18% for the film deposited last, approximately 600 000 pulses after the deposition of the calibration film.

First, two calibration films/plume films (with no substrate movement during the deposition) were made to determine $T_1(x, y)$ for each target: One for the TiO_2 target and one for the CrN target, labeled TiO_2-P and CrN-P, respectively. The number of pulses (N_p) and the relative positioning of the plume on the substrates (x_p, y_p) for the plume films are listed in Table I. Photographs of the plume films are shown in Figs. 2(a) and 2(b), and a measured thickness map of the TiO_2-P film will be shown later, in Fig. 5.

Second, a set of films were simulated/designed and deposited to demonstrate the usability of our simulation method, both single component TiO_2 films and a CCS film.

For the single component films, the aim was to obtain as flat films as possible across the central part of the 50.8 mm wafers: Five TiO_2 films were deposited on rotating substrates, but with different positions of the plume center on the substrate. These films are referred to as flat films. Four of these are labeled TiO_2-FR, meaning that the substrates are "fully rotated" (i.e., that the substrate makes an integer number of rotations during the actual firing of the laser pulses), and one was labeled TiO_2-NFR, as the substrate was not "fully rotated" for this film. The number of pulses (N_p) and the relative positioning of the plume on the substrates (x_p, y_p) for the TiO_2 films are listed in Table I. Note that the films deposited with the center of the plume far from the substrate center (large x_p and/or y_p), a lower deposition rate per pulse is to be expected across the substrate. A photograph of a "flat" TiO_2 film (TiO_2-FR1) is shown in Fig. 2(c).

For the second type of designed films, a CCS thin film using a TiO_2 and a CrN target was deposited. The CCS film was built up by adding (thin) plume films at two locations on the substrate, as illustrated in Fig. 1(b). For this film, the two locations are on the $x-$axis ($x_p = 0$) and the position on the $y-$axis is at $y_p = \pm 1.3$ cm. The plume is "moved" from one position to the other by rotating the substrate 180 degrees. A photograph of the CCS film is shown in Fig. 2(d). The CCS film is built up by 400 repetitions of the deposition sequence listed in Table II: First the laser is fired 26 times onto the TiO_2-target with the substrate fixed in the starting position/orientation ($y_p = -1.3$ cm). Then the substrate is rotated 180° and an additional 22 pulses is fired onto the target, to obtain an even thickness of TiO_2 across the wafer. Finally, 45 laser pulses are fired onto the CrN target to obtain an increasing amount of Cr and N across the centerline of the wafer, ranging from ≈2 at. % at $y = -1.75$ cm to 8 at. % in at $y = +1.75$ cm. The substrate is then rotated back to the starting 0° position, and the sequence is repeated.

Tables I and II also list data on the thickness variation determined, as described below, for the different samples.

B. Film characterization

A dual rotating compensator variable angle spectroscopic ellipsometer (VASE) (RC2, J. A. Woollam Co.) with a photon energy range 0.73–5.9 eV was used to determine the thickness variation across the 50.8 mm (2 in.) substrates. The samples were illuminated with white light. The VASE data were measured slightly differently for the different samples depending on the expected variation in optical properties. For the plume films and the TiO_2 films, Mueller matrix ellipsometric measurements at 55°–75° angle of incidence with 5° intervals were taken at selected locations on the samples, giving insight into the variation in optical properties and thickness across the samples. Next, the thickness maps were obtained using a fixed angle of incidence, 65°, with an automated routine in which each general ellipsometric measurement was taken over 5 s and repeated with 1.5 mm spacing in the x and y directions over the whole 50.8 mm (2 in.) wafer. The measurements were, thus, done at 794 locations across the wafer. Focusing optics was

used to reduce the ellipsometer light beam diameter from approximately 3 mm to 150 μm (NA $\approx$ 0.15). For the CCS sample, as the optical properties were expected to vary greatly across the sample since the composition is varying, multiple angles of incidence at each measurement location were taken. This is done in order to enhance the likelihood of obtaining a global minimum when fitting for optical properties, thin film thickness, and surface roughness simultaneously. For the CCS sample, the main region of interest is within the $1.5 \times 4\,\text{cm}^2$ (white dashed) rectangle indicated in Fig. 2(d). VASE measurements were taken with a resolution of 3.75 mm in x- and 4.4 mm in the y- direction within this rectangle. Along the centerline (at $x = 0$), the spacing between the measurement points was halved (i.e., 2.2 mm), as it is along the centerline the doping concentration is tailored. All measurements were taken with the use of focusing optics. This mapping procedure was chosen in order to get a good overview of both optical properties and thickness distribution across the region of interest on the CCS sample.

For measurements of the surface topography, a Bruker Dimension Icon atomic force microscope (AFM) with a ScanAsyst tip in the tapping mode was used. All measurements were taken using Bruker's proprietary algorithm in a ScanAsyst/air mode. The images were analyzed using Gwyddion[29] (http://gwyddion.net/), where the following image correction functions were applied to all scans: (1) level data by mean level subtraction, (2) align rows by the median method, and (3) remove horizontal scars.

For measurements of Cr dopant concentrations, secondary ion mass spectroscopy (SIMS) was performed, using a Cameca IMS 7f. The measurements were performed with O_2^+ ions primary beam at 10 kV. Positive secondary ions were collected, and the signals from ^{52}Cr and $^{48}Ti^{16}O^{16}O$ were measured. For our samples, special care needs to be taken in the quantification since we are at or above the concentration limit for SIMS to be accurate (for 1 at. % and higher concentrations),[30] and large uncertainty is to be expected. Two Cr implanted TiO_2 reference samples were used to find the relative sensitivity factor, RSF[30]: a single crystal rutile TiO_2 substrate and a single crystal anatase TiO_2 substrate (MTI corp), both with Cr implanted to 5 at. %.

III. THICKNESS MAPPING

As mentioned earlier, a crucial point in the simulation of PLD deposition is accurate knowledge on how much material is deposited for each laser pulse that hits the target and how this material spreads out across the substrate, $T_1(x, y)$. This is found by depositing a high number of pulses, N_p, and measuring the total thickness, $T(x, y)$, as $T_1(x, y) = T(x, y)/N_p$. When optical methods are used to determine $T(x, y)$, care must be taken since the accuracy of the results depends on how accurately the optical properties (i.e., the complex refractive index; $\tilde{n}$ = n + ik, where n is the refractive index and k the extinction coefficient) are known. We use variable angle spectroscopic ellipsometry (VASE) to determine the complex refractive index and the thickness with high accuracy.

In this paper, single films of *a priori* unknown optical properties and thickness [on known c-Si(100) substrates with an SiO_2 thickness of 1.62–3.31 nm on the surface, tabulated optical properties of Si and SiO_2 from Ref. 31] and with unknown surface topography are characterized. For some of the samples, input on the topography of the films is obtained from AFM measurements. Based on the different categories of samples studied in this work (plume, flat, and CCS films), we expect differences in how the optical properties and the film thickness vary across the samples from category to category. Therefore, the procedure for mapping out the thickness also varies, as described below.

TABLE II. CCS film deposition routine (see the text for explanation). The sequence of the three sub-layers listed is repeated 400 times to get a final CCS film thickness of 400–500 nm, along the centerline of the wafer. Also listed is the maximum thickness of each sub-layer, which is found at the location of the plume center.

Sub-layer material	Substrate position (deg)	Number of laser pulses	Max thickness sub-layer (nm)
TiO_2	0	26	0.884
TiO_2	180	22	0.748
CrN	180	45	0.176

A. Plume films

The plume films, TiO_2-P and CrN-P, are deposited using a single target and without moving or rotating the substrate. The laser fluence and repetition rate, the temperature of the substrate, and the background gas conditions are the same as for the deposition of the flat films and the CCS film later. The thickness variation of the resulting films corresponds to the natural material spread caused by the relatively small size of the plume. Photographs of the TiO_2-P and CrN-P samples are shown in Figs. 2(a) and 2(b), respectively.

AFM measurements acquired over $2 \times 2\,\mu\text{m}^2$ at three different locations on the TiO_2 plume film are shown in Figs. 3(a)–3(c), with the locations on the sample indicated in Fig. 2(a). Line profiles through the middle of the AFM images are shown in Figs. 3(d)–3(f). The line profiles reveal that at location 1, corresponding to the plume center where the film is the thickest, there are holes in the film, up to several tens of nm deep. These holes get shallower toward the outer parts of the plume film (location 2), and they disappear at the edge of the plume film (location 3). The holes might affect the optical properties of the film and must, therefore, be taken into consideration for the optical model for the plume films.

As the procedure used to accurately determine the complex refractive index and the material distribution for the two plume films is the same, only the procedure for the TiO_2-P film is presented here. First, VASE measurements at three different locations on the TiO_2-P film were analyzed individually and modeled as single "unknown" thin films (unknown film thickness and unknown film optical properties) with a Kramer–Kronig (KK) consistent b-spline layer[32,33] on a semi-infinite "known" c-Si substrate (with a thin layer of "known" SiO_2 optical properties with unknown thickness). As indicated in Fig. 2(a), the VASE data are from somewhat different locations on the sample than the AFM data, although location 4 is still between the plume center and the edge and location 5 is at the plume film edge.

In line with standard practice, the unknown film surface roughness was taken into account in the optical modeling by adding a thin (~1–5 nm) surface layer consisting of a 50–50 volume fraction of thin film and void using the Bruggeman

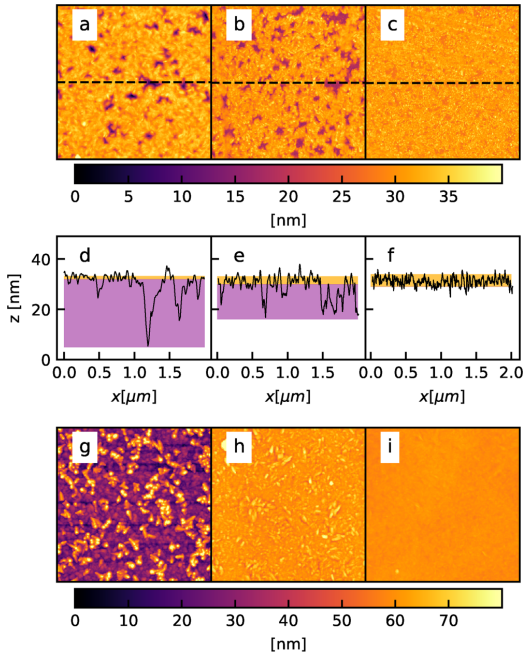

FIG. 3. (a)–(c) $2 \times 2\,\mu m^2$ AFM images of TiO_2-P, in location 1–3, indicated i Fig. 2(a), respectively. (d)–(f) Line profiles along the middle of the AFM images, as indicated by the dashed lines in (a)–(c), respectively. Yellow colored areas in the line scans correspond to ellipsometric best fit roughness, while the purple area indicates the inclusion of some volume fraction of void in the film in the ellipsometry analysis. (g)–(i) $2 \times 2\,\mu m^2$ AFM images of the CCS film, in location 1–3, indicated in Fig. 2(d), respectively.

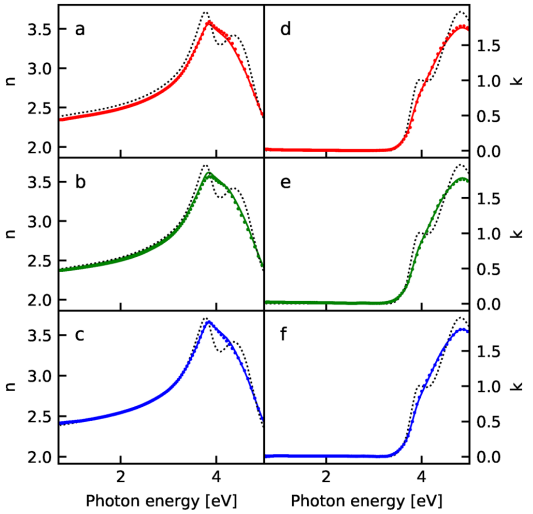

FIG. 4. (a)–(c) The real part of the complex refractive index, n, for locations 1, 4, and 5, indicated in Fig. 2(a), respectively, for two different optical models as explained in the text of the films (dotted and solid curves). (d)–(f) The imaginary part of the complex refractive index, k, for locations (1, 4, and 5), respectively. The black dotted curves in each panels are n and k resulting from measurements on an anatase (100) TiO_2 single crystal.

effective medium approximation (BEMA).[34] The goodness of fit between the measured data and the optical model was quantified by the mean square error (MSE).[35] The selected optical model resulted in a good fit to the measured data for the three locations, with MSE in the range of 2–5. The resulting real (n) and imaginary (k) parts of the complex refractive index for the three locations on the TiO_2-P plume film are plotted as dotted colored curves in Fig. 4. Also plotted (black dotted curves) are the results from measurements of a single crystal reference sample of anatase (001) TiO_2 (from MTI Corp.).

As seen from Fig. 4, the optical properties of the TiO_2-P plume film deviate somewhat from the anatase TiO_2 reference and also vary slightly as a function of distance from the plume center, especially visible below the bandgap of TiO_2 (~3.2 eV) for the refractive index n. This slight variation in n can be explained by the presence of voids in the films,[36] in agreement with what we have observed in the AFM images shown in Fig. 3. Not taking this slight variation in optical properties into consideration might lead to less accurate values for the thickness variation across the plume film. The deviation in the above bandgap region of the complex refractive index compared to the single crystal reference sample is most likely due to the multi-crystalline nature of the film, seen in XRD and Raman characterization of the film (not shown).

To implement the variation in the amount of void across the plume film in the optical model and at the same time reduce the number of fit parameters for the later plume film mapping analysis, the VASE data from all three locations were analyzed a second time, but now in a single "multi-sample"[37] ("multi-location" in our case) analysis. Data from all three of the multiple angles of incidence measurements are analyzed simultaneously, instead of the individual analysis for each location separately done in the first analysis. In the second, a "multi-location" approach, one assumes that the optical properties of the material are the same at different locations and that the amount of voids is responsible for the variation in the refractive index. The optical model in the second analysis consisted of a Bruggeman effective medium approximation (EMA) layer,[38] consisting of a b-spline fit for the film material and of void,[39] where the amount of void, thickness of film material, and surface roughness were used as local fitting parameters for each of the three locations. The b-spline part of the effective medium acted as a "global" fit parameter that did not vary between the three locations, along with the SiO_2 interface layer. The MSE of the new, multi-sample analysis, EMA based model

was 6, and the resulting complex refractive index is also plotted in Fig. 4 as solid lines for the three locations.

As can be seen from Fig. 4, the results from the second modeling of the VASE data (solid lines) match very well with the individually determined optical properties (dotted lines) found in the first modeling. Since we have observed voids in the film, the fact that the two approaches result in similar refractive indices justifies the simplifications done in the second model, namely, that the variation observed in the refractive index across the sample is mainly due to porosity. The thicknesses obtained using the second model match the ones obtained using the first very well, with a difference found to be below 1 nm, corresponding to less than 1% of the total film thickness.

Finally, the thickness map for the whole plume film was found performing a "multi-location" sequential analysis of measurements at 794 locations across the 50.8 mm (2 in.) substrate, with a 1.5 mm spacing in the x and y directions. In the optical model, the b-spline and the SiO_2 thickness found from the second modeling were assumed to be valid for the whole sample, and the parameters "thickness TiO_2 film," "roughness," and the "amount of void" were freely fitted at each location. The mean MSE for the whole TiO_2 plume film (all 794 locations) was 6, with a standard deviation of 2.1. The TiO_2-P plume film was determined to be 533 nm thick at its thickest (in the plume center) and 31 nm furthest away from the plume center; see Table I. The fitted roughness for each measurement point in the map (not shown) indicates a smooth film, with radially increasing surface roughness, from 1 nm at the plume center to 5 nm at the plume edge. The fitted amount of voids decreases radially from 4% in the center to 0% at the edge. The orange coloring in the line profiles of Figs. 3(d)–3(f) indicates the range of roughness values obtained from the VASE data, and the purple coloring indicates that a fraction of voids is included to obtain a good fit.

The same combined AFM and VASE data analysis procedures were then executed on the CrN plume film, CrN-P, and similar trends were found, with the exception that voids only appeared toward the edge of the sample, where the peak to valley roughness features became comparable to the determined film thickness. The difference in film thickness (obtained for the two optical models) was again determined to be below 1 nm, and the mean MSE over all 794 locations was 6 with a standard deviation of 1.8. The roughness and porosity trends determined by VASE were found to agree with AFM measurements to be in the range of 1–7 nm surface roughness and 0%–12% void (from center to edge).

The final plume film thickness maps are used as input for modeling of the material spread in Secs. IV–VII. Note that even though we have included porosity in the optical modeling here, we have chosen not to include occurrence of porosity when modeling material spread in Sec. IV. This is in line with the assumption that the volume of the deposited material is the same in the designed films as in the plume films. However, we will present the effect of accounting for porosity on the final thickness of the CCS film in Sec. VII.

B. Flat TiO_2 films

The complex refractive index and the thickness of the five TiO_2 films deposited on rotating Si(001) substrates were obtained in a similar way as for the two plume films. For these films, however, the initial overview measurements (not shown) indicated that the refractive index did not vary significantly across the substrate. A single b-spline layer was, thus, used in the optical model of the TiO_2 film, and it was fitted to the data obtained using multiple angles of incidence on two different locations on the films: one in the center and one toward the edge of the 50.8 mm (2 in.) substrate. A surface roughness layer and a SiO_2 interface layer were included in the model like for the plume samples.

As before, the thickness maps for the five TiO_2 films were then obtained by fixing the b-spline model and the SiO_2 layer obtained from the first two locations (i.e., assuming identical optical properties and SiO_2 thickness across the film) in a "multi-location" analysis of the VASE data from 794 locations simultaneously. The parameters "film thickness" and "roughness" were fitted at each of the 794 locations. The fitted BEMA surface roughness layer varied slightly as a function of distance from the rotation center, from 3 to 2 nm for the smoothest film, and 6 to 3 nm for the roughest film (not shown). The trend in increasing roughness away from the plume center was observed in all films and in agreement with the AFM measurements (not shown). The uncertainty of the film thickness was again estimated to be ± 1 nm, corresponding to less than 1% of the total film thickness. The average MSE for each of the films over the whole map was again found to be from 5 to 6 with a standard deviation of 2–3, which again indicates a good match of the optical model to measured data. The TiO_2 flat films were determined to be in the range of 100–190 nm thick and with a thickness variation depending on x_p and y_p (the relative position of the plume on the substrate during deposition); see Table I.

C. The continuous compositional spread film

The continuous compositional spread (CCS) film has a designed thickness variation determined by the position of the two plume centers on the substrate, and the refractive index will also most likely vary. Therefore, the unknown refractive index for each location in the CCS film was found using a single b-spline layer. The b-spline model, and, thus, the refractive index, is allowed to vary freely at each measured point, along with the thickness of the film and thickness of the surface roughness, as the measurement included multiple angles of incidence for each point in the measured map. To minimize the number of parameters fitted, the SiO_2 interface layer was fixed at 3.3 nm as this was the best fit for several measurements along the centerline. The variation in the refractive index as a function of Cr and N content will be presented elsewhere. In this work, our main objective is to determine the thickness variation accurately, along with the variation in surface roughness.

The CCS film thickness was determined to be between 377 and 437 nm along the centerline for which the doping concentration gradient was optimized. The surface roughness obtained from the VASE data varied greatly across the sample, from 1 to 25 nm, with the roughest area being at $y = -1.75$ cm (where less CrN was deposited) and the smoothest area around the second plume center, at $y = 1.3$ cm. The trends in roughness were again confirmed by AFM measurements; see Figs. 3(g)–3(i). As the thickness and refractive index are found at each point, with a mean MSE of 6

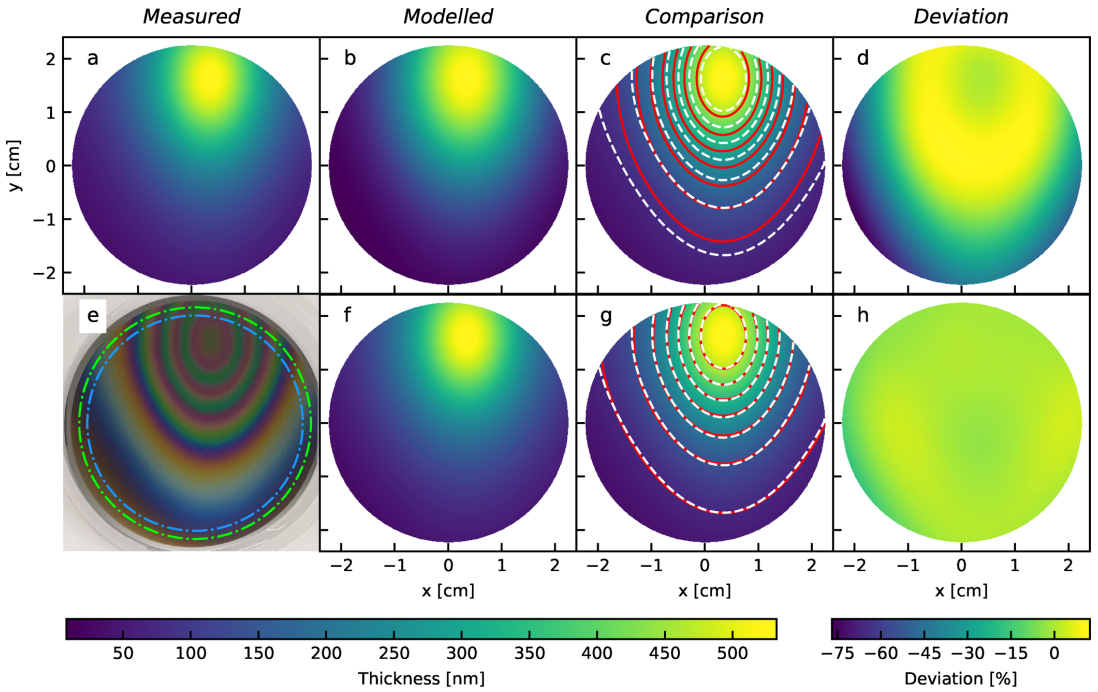

FIG. 5. (a) Measured thickness map for the TiO_2-P plume film, obtained from the VASE data. Modeled thickness map using (b) the single-term plume model in Eq. (1) or (f) the double-term plume model in Eq. (2). Comparison between the measured and simulated maps for the single (c) and double (g) term plume model, with the corresponding deviation (in %) in (d) and (h). In (c) and (g), the red curves are contours for the measured map, while the dashed white are contours for the simulated maps. (e) Photography of the TiO_2-P plume film, where the green dashed–dotted circle indicates the outer boundary for the area mapped using VASE, and the blue dashed circle indicates the area used for curve fitting of the model. The color scale for the thickness maps in (a)–(c) and (f)–(g) is shown in the bottom left and for the deviation maps in the bottom right.

and a standard deviation of 3, the uncertainty of the thickness was again estimated to be below 1 nm.

The thicknesses obtained from the VASE data analysis are hereafter referred to as "the measured thicknesses."

IV. PLUME MODELING

In this section, we present how we model the material spread on the substrate. The starting point is the careful mapping of the plume film thickness across the substrate, as described in Sec. III. The resulting thickness map for the TiO_2 plume film is shown in Fig. 5(a). In total, 794 locations across this region were measured, and the thickness is interpolated between these 794 points. The photograph of the plume film is shown again in Fig. 5(e).

As mentioned in Sec. I, the material spread in a plume film can be modeled as shown in Eq. (1). From Fig. 5(e), it can be seen that the thickness distribution of the TiO_2-P plume film has an elliptical shape. (A more circular shape would have been obtained using a square shaped laser spot, instead of the rectangular one that we have used.) To be able to fit Eq. (1), and later Eq. (2), directly to the measured thickness distribution, we need to find the orientation of this ellipse and align it with the x and y axis. After alignment, our measured thickness map was fitted to Eq. (1). The resulting fitted model of the material spread can be seen in Fig. 5(b), and the fitted parameters are listed in Table III.

The fitted plume film thickness model $T(x, y)$ is compared with the measured thickness in Fig. 5(c), data in white, model in red. The deviation between the two (in %), calculated as the difference between the modeled and measured thickness, divided by the measured thickness, is shown in Fig. 5(d).

From Figs. 5(c) and 5(d), it can be seen that there is a considerable deviation in using Eq. (1) as a model for the material distribution in the TiO_2 plume film. Our suggested solution is to model the plume as a sum of multiple sub-plumes by adding terms to Eq. (1) with each term assigned a weight. These plumes have the same center position, x_p and y_p, but different angular spread. This

TABLE III. Plume model fit parameters found by fitting the measured plume film thickness to Eq. (1), in the first row, or to Eq. (2) in the second and third row. T_0 is the maximum thickness of the plume film. T_0/N_p is the maximum thickness divided by the number of pulses N_p, i.e., the maximum thickness deposited per pulse. n_1, m_1, n_2, and m_2 are the exponents describing the spread of the plume. Values for x_p, y_p, z, and N_p are listed in Table I.

Plume film	T_0 (nm)	T_0/N_p (nm)	n_1	m_1	n_2	m_2
TiO_2-P	532.6	0.0355	21.4	10.1	…	…
TiO_2-P	532.6	0.0355	10.7	5.9	47.9	22.3
CrN-P	156.4	0.0039	6.4	4.4	31.0	17.6

approach can be justified as different species (atomic and molecular ions) can have different angular distributions in the plume[26,40,41] and, thus, make up separate sub-plumes, all contributing to the total plume film thickness. This concept is implemented in our simulations in its simplest version by modeling the plume film's thickness as consisting of two sub-plume films each weighted with a factor 1/2,

$$T(x,y) = \frac{1}{2}T_0\left(\frac{z}{\sqrt{z^2+(x-x_p)^2}}\right)^{n_1}\left(\frac{z}{\sqrt{z^2+(y-y_p)^2}}\right)^{m_1} + \frac{1}{2}T_0\left(\frac{z}{\sqrt{z^2+(x-x_p)^2}}\right)^{n_2}\left(\frac{z}{\sqrt{z^2+(y-y_p)^2}}\right)^{m_2}, \tag{2}$$

where n_1 and m_1 describe the angular distribution of the first sub-plume film and n_2 and m_2 describe the angular distribution of the second.

The resulting improvement in model fit is shown in Figs. 5(f)–5(h), where the results using Eq. (2) are plotted. The deviation is considerably reduced when using the double plume model. The resulting fitting parameters for TiO_2-P, using the double plume in the expression for $T(x, y)$, are also listed in Table III, together with the fitting parameters for the CrN plume film, used for the simulation of the CCS film below. For both plume films, the maximum amount of material deposited for a single laser pulse, T_0/N_p, is also given.

In the following, the material deposited per pulse, defined as $T_1(x, y) = T(x, y)/N_p$, is used in the simulations of the PLD film deposition of both single component films (Sec. V) and CCS films (Sec. VII).

The concept of including multiple sub-plume terms to model the plume film thickness could be extended to an arbitrary number of terms, which could be connected to the actual species present in the plume, but this is beyond the scope of this article. The agreement between the measured and modeled plume film thickness for our plume films is very high.

V. PLD FILM SIMULATION PROCEDURE AND ASSUMPTIONS

Before we describe the PLD simulations, we have a short note on the time scale of different processes occurring in the PLD deposition. The laser pulse has a duration on the order of nanoseconds (20 ns FWHM in this work), and the laser ignites a plasma plume that exists for some hundred microseconds.[26] The time between the pulses is in milliseconds (100–200 ms for in this work). As the laser pulse and the plume duration are short compared to the time between pulses, the material transfer can be considered instantaneous (i.e., that no rotation occurs during the material deposition).

The PLD deposition is simulated by first modeling the material spread deposited by a single pulse as $T_1(x, y) = T(x, y)/N_p$, where $T(x, y)$ is determined as described in Sec. IV. When T_0, n_1, m_1, n_2, and m_2 are determined, x_p and y_p can be chosen, depending on the kind of film one wants to deposit.

The deposition of the film on the substrate is simulated by repetitively adding $T_1(x, y)$, from one or more targets, at the selected location on the substrate. Similarly to previous work on this type of simulations,[14,21] we, therefore, assume that the sticking coefficient is constant during the deposition of the films (i.e., independent of film thickness) and that the sticking is the same for a given material (A) both when deposited on the same material (A) or another material (B). In other words, we assume $T_1^{AA}(x, y) = T_1^{AB}(x, y)$. We also assume that the volume of the deposited material is independent of film thickness and the growing film's surface. Finally, we assume that the laser fluence hitting the target is constant, meaning that the amount of material in the plume and the plume shape does not change over time.

The validity of the assumptions is addressed in the discussion of the results. However, as was mentioned in Sec. I, since the aim of this work is to develop a design tool for PLD, and not to do an atomistic simulation of the actual film growth, it is not crucial that all assumptions are fully valid.

The next step in the simulation is to choose the movement of the substrate during deposition. In our case, the substrate can be stationary or it can be rotating at a certain speed, while the material is added to it. For multi-component CCS films, the deposition process is not continuous but is divided into steps where material is deposited and rotational steps (typically 120 or 180° at a time) where no material is deposited. In this manner, material from different targets can be deposited at different locations on the substrate. The simulation of the CCS deposition will be presented in Sec. VII. First, we focus on single component films.

VI. SIMULATION AND GROWTH OF FLAT PLD FILMS

For the simplest case of a non-moving substrate, the deposited (single component) film can be simulated by multiplying the

material spread by the desired number of pulses. For a rotating substrate, the material spread $T_1(x, y)$ is added to the substrate for each pulse with the chosen rotation of the substrate between each additional laser pulse.

A. Single vs double plume model

To demonstrate the improved accuracy of the plume film modeling using two sub-plumes in the expression for $T(x, y)$, we deposited a film (TiO_2-FR-0 in Table I) with the same parameters as for the deposition of the TiO_2-P plume film, but now for a rotating substrate ($\omega = 29$ deg/s). This results in a film symmetrical around the rotation center (nominally at $x = 0, y = 0$), as shown in Fig. 6. In Figs. 6(a) and 6(b), the thickness map for TiO_2-FR-0 obtained from ellipsometry measurements is shown in the left half of each panel, while the thickness from the PLD simulation is shown in the right half of the panels for the single and double plume models, respectively. The deviation between the measured and simulated film thickness maps is shown in Figs. 6(c) and 6(d) for the single and double plume models, respectively, and we see a significantly better agreement using the double plume model. For this reason, all simulations presented from here on are simulated using the double plume model in Eq. (2).

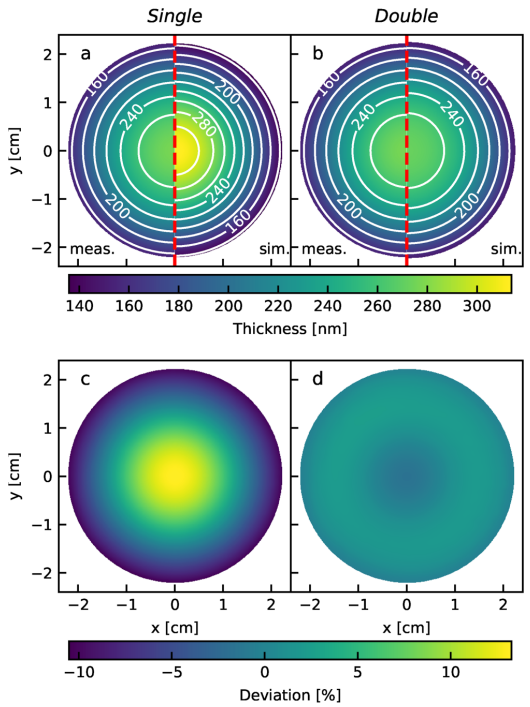

FIG. 6. Thickness maps for TiO_2-FR-0: Measured thickness (left half of the maps) and simulated thickness (right side) when using the single (a) and double (b) plume models in the PLD simulations. The deviation (in %) between the simulated and measured thicknesses when using the single (c) and double (d) plume model for $T(x, y)$ in Eqs. (1) and (2), respectively.

B. The importance of full rotations during deposition

To obtain a uniform film thickness, the substrate must be rotated an integer number of full rotations during the deposition of the film. Figure 7 illustrates the result when the substrate is not fully rotated, as was the case for sample TiO_2-NFR in Table I. (Notice that this film was deposited using slightly different plume parameters than those shown above in Fig. 5.) Figure 7 also illustrates the precision obtained in the PLD simulations when using VASE to determine the thickness maps with a high accuracy, as described in Sec. III. In Fig. 7(a), the measured thickness of TiO_2-NFR-0 is shown, and in (b), the simulated thickness of the same film is shown. This film is grown using 15 000 laser pulses at a 5 Hz repetition rate and with a substrate rotation of 29 °/s. This corresponds to 241.67 rotation of the substrate during the deposition, and thus, 1/3 of a rotation is missing for an integer number of rotations. From Fig. 7, it can be seen that the film thickness is not uniform along a given radius of the sample and that the film is clearly thicker for parts of the rotation. This can be seen both in the measured and simulated thickness, and it should be noted that

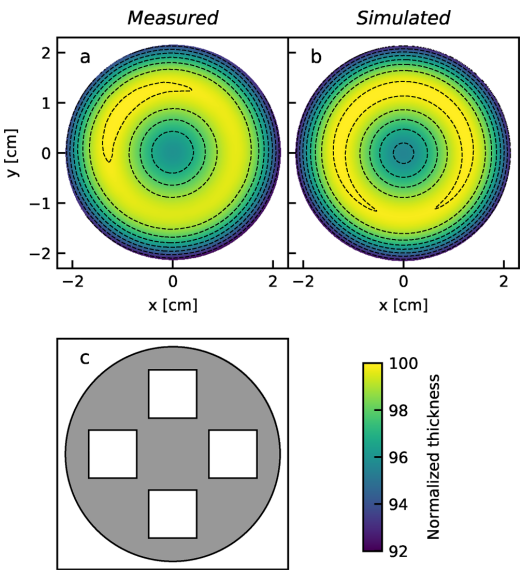

FIG. 7. Measured film thickness (a) and simulated film thickness (b) for the not fully rotated film TiO_2-NFR-0. (c) Schematic drawing of our sample holder where such a "doughnut" film shape is useful.

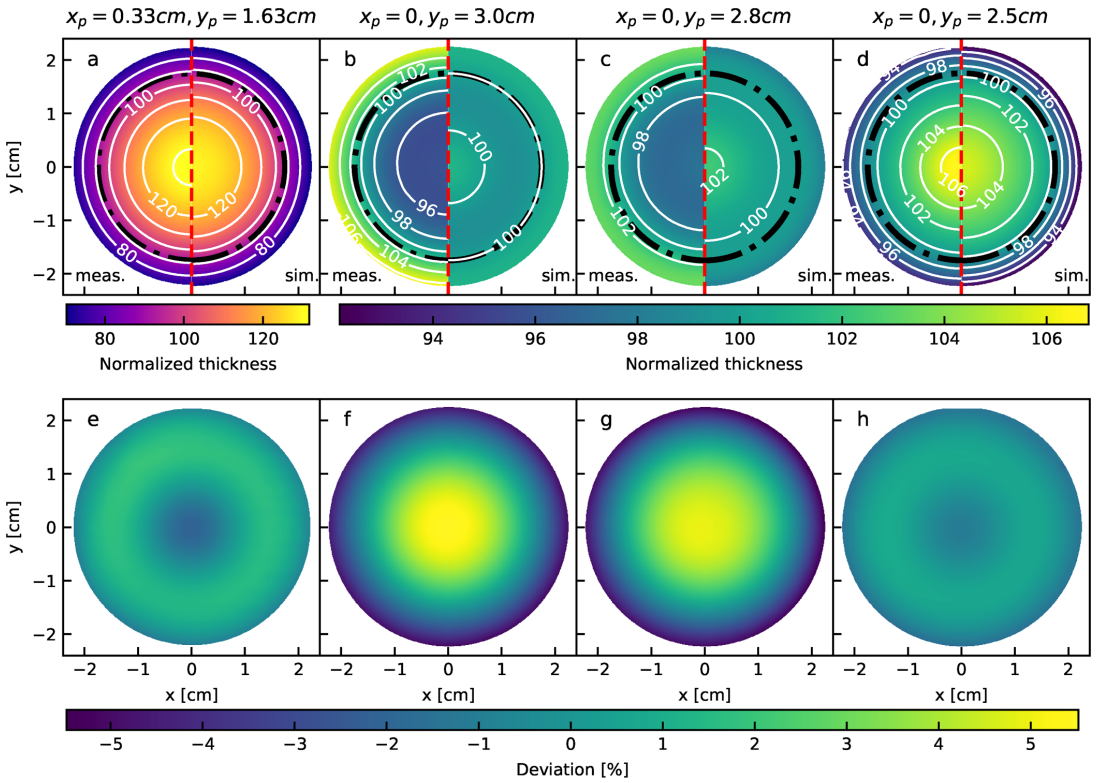

FIG. 8. Comparison of films optimized for having a flat area within a radius of 1.75 cm, indicated by the black dashed–dotted circles. In (a)–(d), the normalized thickness is plotted (measured in the left half and simulated in the right half) for sample TiO_2-FR-0 to TiO_2-FR-3, respectively. The normalized mean thickness of each sample corresponds to a value of 100. The position of the plume for each case, x_p and y_p, is given above the thickness maps. In (e)–(h), the deviation between simulated and measured thicknesses is plotted for the films in (a)–(d), respectively. Note the different color scales used.

this deviation from complete rotational symmetry is caused by the additional 41 pulses after rotation number 241 was completed. In other words, both the simulations and the measurements can detect the effect of 41 out of 15 000 pulses.

It should be mentioned that the non-uniform, donut shape of the thickness for sample TiO_2-NFR-0 is intentional and is ideal when using a substrate holder, such as the one shown in Fig. 7(c), where four $10 \times 10\,mm^2$ substrates are positioned at a certain radius.

C. Optimization of thickness uniformity

We next present how the PLD simulations can be used to optimize the thickness uniformity within a certain diameter of a rotating substrate/substrate holder. The optimization is done using the thickness variation across the region of interest as a fitting parameter to be minimized, while varying x_p and y_p systematically in the simulations.

In Fig. 8, we show the results from an iterative optimization of the film thickness uniformity within a radius of 1.75 cm. Three films were simulated and deposited: TiO_2-FR-1, TiO_2-FR-2, and TiO_2-FR-3; see Table I for details. The starting point is the film presented in Fig. 6, film TiO_2-FR-0, which is repeated in Fig. 8(a) for ease of comparison. As in Fig. 6, the left side of the maps is the measured thicknesses, while the right side is the simulated ones. Since the actual thickness is varying from film to film, the thickness is normalized to the mean thickness of each film: The mean thickness of each sample corresponds to a normalized thickness of 100 nm in Fig. 8, and the actual maximum thicknesses are listed in Table I. Note that in Table I, the minimum thickness listed is outside the current region of

interest. The black dashed–dotted circle in Fig. 8 indicates the 1.75 cm radius area we are optimizing for.

From Fig. 8(a), it is clear that the starting film is thicker in the center (131.7 nm) than 1.75 cm from the center (91.2 nm); thus, we knew we needed to move the center of the material spread, defined by x_p and y_p, further from the substrate center. Indeed, the first attempt of fitting x_p and y_p to obtain a flat film resulted in $x_p = 0$ and $y_p = 3$ cm, meaning that the plume center is actually further out than the edge of the 50.8 mm (2 in.) wafer. The resulting film thickness is shown in Fig. 8(b) for film TiO_2-FR-1. We see that the film is much flatter than the film in Fig. 8(a). However, this film is thinner in the center (96.5 nm) than at 1.75 cm from the center (101.6 nm). In a second attempt, we, therefore, simulated and deposited a film with the center of the material spread slightly closer to the substrate center at $x_p = 0$ and $y_p = 2.8$ cm. The resulting film, TiO_2-FR-2, is shown in Fig. 8(c), and we can see this film is even flatter (97.0 nm in the center and 101.4 nm at 1.75 cm). The normalized measured minimum and maximum thickness within the area of interest (diameter of 3.5 cm) is given in Table IV, together with the variation in the film thickness in this area, ΔT.

The next step is to evaluate the deviation between the simulated and measured film thickness, shown in Figs. 8(e)–8(h). As shown earlier, the starting film, TiO_2-FR-0 in (e), has a very small deviation, even though it is not very flat. However, for film TiO_2-FR-1 and TiO_2-FR-2 in Figs. 8(f) and 8(g), respectively, the deviation is larger. The simulations overestimate the thickness in the center and underestimate it toward the edges of the wafer. For both these films, the plume center has been moved outside the wafer/substrate holder edge: The wafer radius is ~2.55 cm and $y_p = 3.0$ cm and 2.8 cm for TiO_2-FR-1 and TiO_2-FR-2, respectively. This is also far outside the measured and fitted area (radius ~2.28 cm) in the plume modeling. Thus, a considerable part of the plume model used for the simulation of TiO_2-FR-1 and TiO_2-FR-2 is not based on measured data and only on the assumption that the model in Eq. (2) is still valid as we move further away from the plume center. Based on the findings in Fig. 8, we can conclude that this is not the case.

To test the limit of the model use for the TiO_2 plume film, we simulated and deposited a third flat film with the material spread center at the wafer edge, $x_p = 0$ and $y_p = 2.5$ cm, TiO_2-FR-3. The resulting film thickness and deviation between simulation and measurements are shown in Figs. 8(d) and 8(h), respectively. It is clear from Fig. 8(d) that this film is not as uniform in thickness as the films in (b) and (c), but the deviation between the simulations and the measured thickness in Fig. 8(h) is of the same magnitude as for the film in (a). This indicates that the model used for the material spread for TiO_2 breaks down between 2.5 cm $< y_p <$ 2.8 cm.

To solve this problem, one could deposit a plume further out (larger y_p in this case) than used in the current plume film fitting and modeling or even better, deposit on a larger 3 or 4″ wafer (if the PLD setup allows this), map out the thickness distribution with VASE, and use this as input to the simulations. For our use, the TiO_2-FR-1 and TiO_2-FR-2 films are flat enough, and further optimization was not performed.

Until now, we have presented and discussed the normalized thicknesses of the flat films. We now turn the attention to the absolute thicknesses to address the validity of our assumptions of a constant laser fluence as the number of pulses increases (from film to film) and as the film grows. As mentioned in Sec. II, we expect a reduction in the deposition rate due to contamination of the window. We observed (not shown) a roughly linear trend in the reduction in the deposition rate with the number of laser pulses, up to 18% reduction for the film deposited last (600 000 pulses after the plume film). A major part of the deviation between the absolute measured and simulated film thickness can, therefore, be explained by a reduction in laser fluence. We expect that the reduced fluence mainly alters the total thickness and not the thickness distribution[1] and, as such, does not affect the conclusion of the work. For the assumptions of constant sticking and volume of the deposited material, we hypothesize that the effect of these being incorrect is smaller than the effect of the reduction in laser fluence, from film to film. To test the validity of these two assumptions, a systematic study must be carried out, but that is beyond the scope of this work.

TABLE IV. Minimum, NT_{min}, and maximum, NT_{max}, values for the normalized measured thicknesses, within the area of interest (3.5 cm in diameter) of the films shown in Fig. 8. The mean thickness of each sample corresponds to a value of 100 nm. Also listed is the variation in the normalized thickness (in percent) in this area, $\Delta T = (NT_{max} - NT_{min})/NT_{max}$, for each film.

Sample	NT_{min} (nm)	NT_{max} (nm)	ΔT (%)
TiO_2-FR-0	91.2	131.7	30.8
TiO_2-FR-1	95.6	101.6	5.9
TiO_2-FR-2	97.0	101.4	4.4
TiO_2-FR-3	99.0	106.8	7.4

VII. SIMULATION AND GROWTH OF CCS FILMS

In this section, we describe how to simulate and tailor CCS films grown by natural spread PLD using two targets, as illustrated in Fig. 1(b). The resulting two-component CCS films are essentially two plume films added together, but with the plume centers (maximum plume film thickness) at different locations on the substrate. An example of a two-component CCS film is shown in Fig. 2(d). Subsequently, we compare the simulation results with an example film of doped TiO_2. The aim was to deposit a TiO_2 film doped with Cr and N, with the doping concentration ranging from 2 to 8 at. %, while keeping the total film thickness relatively constant along the "centerline" between the two plume centers. To obtain a constant thickness, some TiO_2 had to be added also in the location of the CrN plume center. As described in Sec. II, the final CCS film is built up by 400 repetitions of the deposition sequence listed in Table II. This sequence was determined in an iterative simulation process, where the simulation is mimicking the steps of the actual film deposition.

As for the single component films, the starting point for the simulations is the material spread $T_1(x, y)$ on the 50.8 mm (2 in.) substrate, but now for two targets. The $T_1(x, y)$ for the two target materials are then added to the substrate at the chosen plume positions (defined by x_p and y_p). The simulations can be extended to three or more targets. In general, the CCS film thickness and composition can

be tailored by changing the distance between the centers of the material spread (e.g., by varying y_p while keeping x_p constant) and varying the total number of pulses fired onto the two targets.

The composition of the CCS films will vary gradually along a line between the two plume center positions (along the y-axis for our example film). The composition can be calculated by dividing the (total) simulated thickness of one of the components with the total thickness of the CCS film and subsequently converting the volume fraction to at. %. For the simulated Cr and N doped TiO_2, the conversion to at. % was based on the assumption that the material deposited with the CrN target (in the CrN-P plume film) had the tabulated density of CrN and that the total film had the density of anatase TiO_2.

Focusing first on the thickness of the CCS film, the measured (a) and simulated (b) thickness maps of the central $1 \times 3.5\,\mathrm{cm}^2$ region of the Cr and N doped TiO_2 CCS film are shown in Fig. 9. Note that the sample is rotated 90° as compared to the photograph in Fig. 2(d), as shown in Fig. 9(d), where the white dashed rectangle indicates the mapped region.

Comparing Figs. 9(a) and 9(b), it can be seen that the measured and simulated thicknesses match, both in the thickness trends and features, such as the two maxima values and their positions. There is a small difference in absolute thickness, where the measured film is thinner than the simulated. This difference indicates that not all the assumptions made in the simulation (constant sticking coefficient, volume, and laser fluence) are valid.

To test the validity of the assumptions, we re-simulated the CCS film thickness along the centerline $x = 0$ [indicated by the red dashed line between (a) and (b) in Fig. 9] two times. The results from the initial and two subsequent simulations are presented in Fig. 10 together with the measured thickness. In the second simulation, we assume that the volume is not constant, meaning that when material is deposited in the film, it has a different volume than when the same material was deposited in the plume/calibration film. As mentioned in Sec. III where the thickness mapping was presented, we did observe voids in the TiO_2-P and the CrN-P plume film, but not in the CCS film; see Fig. 3. This indicates that the actual growth results in a denser film and that the assumption of a constant volume is not correct.

One way to account for the difference in volume between the calibration film and the actual film is to "remove" the voids from the plume film, effectively reducing $T_1(x, y)$.

The second simulation (green dashed curve in Fig. 10) accounts for the fraction of voids obtained in the VASE data analysis (meaning we subtract the film volume corresponding to the volume % voids and, hence, assuming the material deposited to be 100% dense). We see from the figure that the deviation between the simulated (green curve) and measured (black curve) thickness is reduced when accounting for the presence of voids. Note that the curve shape is slightly different for the initial and second simulations (especially for $y < -1.0$ cm and $y > +1.0$ cm). This is due to the (measured) variation in the fraction of void along the centerline. From Fig. 10, it is clear that the occurrence of voids in the plume films does not fully explain the deviation between the measured and initially simulated thickness.

In the third simulation, we assume again a constant volume as in the initial simulation, but now, the laser fluence is not assumed to be constant: We assume that the fluence hitting the target was lower when the CCS film was made, compared to the fluence when the plume films were made. A lower fluence might reduce the ablation rate and, thus, the amount of material in the plume. This will result in a reduced deposition rate and a smaller $T_1(x, y)$.

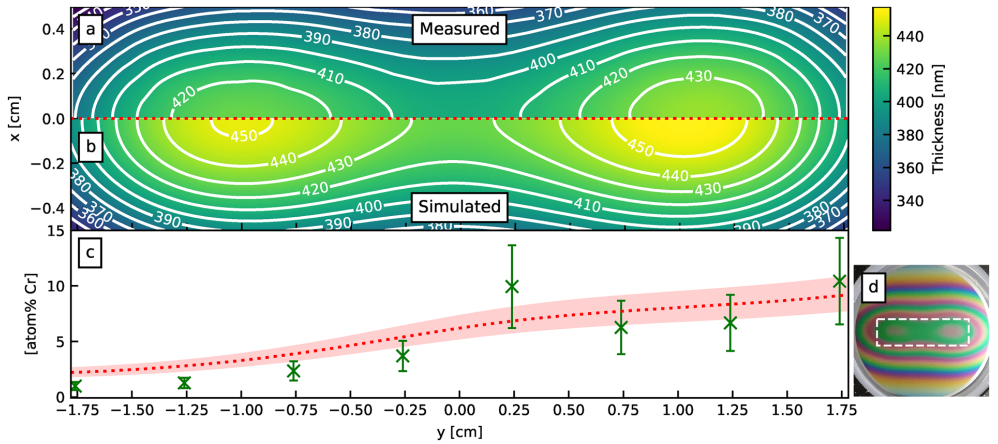

FIG. 9. Cr and N doped TiO_2 CCS film thickness and composition. Measured (a) and simulated (b) thickness maps above and below the $x = 0$ line, respectively. (c) Calculated (red dotted line and shading) and measured (in green markers) Cr content along the $x = 0$ cm line. (d) Photograph of the film indicating the area of interest inside the white rectangle. Note that the CCS film and the plots in (a)–(c) are rotated 90° compared with Fig. 2(d).

As mentioned in Sec. II, we did not clean the laser entry window between each deposition, and this means that material was built up on the inside of the window as the number of pulses fired onto the target increased. The CCS film was deposited approximately 170 000 laser pulses after the TiO_2-P film. We did not measure the actual reduction in the transmission of the laser entry window, meaning that we do not know the actual reduction in the fluence.

If we assume that the only factor explaining the deviation between the measured and simulated thickness is a reduction in the laser fluence/deposition rate, we can multiply the initial thickness simulation with a correction factor to take the reduction in fluence into account. We somewhat arbitrarily choose to calculate the scaling factor by dividing the measured thickness by the thickness for the initial simulation for $y = -1.3$ cm, i.e., at the first plume center and get a value of ≈95%. The third simulation of the CCS film thickness then consists of multiplying the result from the initial simulation by this correction factor. The result is plotted as the blue dashed curve in Fig. 10.

We see from Fig. 10 that the fit is almost perfect near the first plume center ($y = -1.3$ cm). This corresponds to a location where mainly TiO_2 has been deposited: The Cr,N doping level is ≈2 at. % here. The reminding deviation between the measured and third simulation indicates that also the other assumption of constant sticking and volume might be incorrect. At the second plume center ($y = +1.3$ cm, ≈8 at. % doping), we see a larger deviation between the simulated (blue dashed curve) and measured (black curve), and this indicates that the assumption $T_1^{AA}(x, y) = T_1^{AB}(x, y)$ is not valid, especially not for larger doping concentrations.

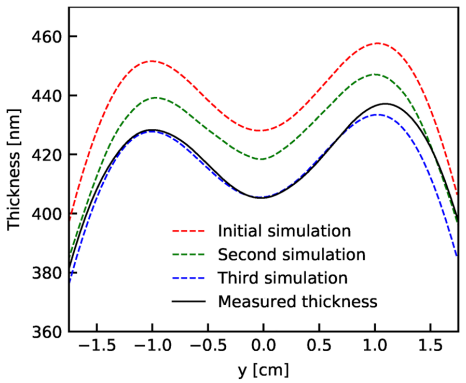

FIG. 10. Plot of the measured (black curve) and simulated (red, green, and blue) thickness along the centerline of the CCS film at $x = 0$ cm [see Figs. 9(a) and 9(b)]. For the initial simulation (red dashed curve), the volume of the deposited material is assumed to be constant (and the same for the plume film and the CCS film), while for the second (green dashes), the volume is not constant, but smaller in the CCS film than in the plume film. For the third simulation, the volume is assumed constant again, but the deposition rate is lowered due to a reduction in laser fluence between the growth of the plume film and the CCS film. See the text for details.

Based on the above observations, we argue that the second simulation, accounting for voids (in green), does not fully explain the deviation between the measured and initially simulated thickness. We conclude that the most likely main contribution to the deviation between the simulated and measured thickness is a lowering of material deposited per pulse due to laser entry window contamination. It is also clear that our assumption of a constant deposition rate independent of a deposition surface (i.e., constant sticking and volume of the deposited material) is not valid, at least not for higher doping concentrations.

Moving onto the CCS film composition, the simulated (dotted red line) and measured (green markers) Cr concentrations along the centerline [$x = 0$, marked with a red dashed line between Figs. 9(a) and 9(b)] are plotted in Fig. 9(c). An estimate of the uncertainty for the simulated concentration is indicated by the shaded light red area. The uncertainty is estimated based on the uncertainty in the densities used for the conversion from volume to at. %. The upper bound of the red shading is found assuming the TiO_2 density to be 85% of the tabulated value. The lower bounds is found by assuming the CrN to have a density of 85% of the tabulated value. For the measured Cr concentration, the data are calibrated using two reference samples with known Cr content implanted. To estimate the uncertainty, we calculated an average RSF based on three different measurements of reference samples. The resulting uncertainty is shown by the green error bars in Fig. 9(c).

As SIMS has such a large uncertainty in the absolute value for concentrations of this magnitude, it is more reasonable to use the results to compare the trends of the measured Cr concentration profile and the simulated one than the absolute values. Looking at the results, it is clear that the trends of the concentration curve of the simulation are very similar to the trend of the measured concentration.

For two locations, $y = 0.25$ cm and 1.75 cm, the measured Cr concentration deviates from the overall trend. We speculate that the seemingly higher Cr concentrations at these locations are due to differences in crystalline quality at different positions along the centerline. Possible causes can be differences in kinetic energy for the species arriving on the substrate during the deposition and/or the amount of doping. The poorer crystallinity might lead to changes in the ion yield in the SIMS sputtering process, and this might result in measured Cr concentrations deviating from the overall trend.

VIII. pyPLD—AN OPEN PYTHON LIBRARY FOR PLD SIMULATION

In this work, we have presented how we have simulated the deposition of single component PLD and CCS nc-PLD thin films. All the modeling and simulation described in Secs. IV–VII were implemented in a Python library named pyPLD that will be made openly available for use and further development/extensions. The library source code will be made available through GitHub. This library is licensed under the EUPL-1.2 license.

The library includes functions to read and handle thin film thickness data (obtained using VASE or any other method available to the users), to find the orientation of asymmetric plume films, to model the material spread from a single laser pulse using the single

or double plume model, and to simulate and optimize the PLD and nc-PLD deposition. Also included is a tool to calculate the needed number of pulses to secure deposition during full rotations when assuming a rotating substrate. In addition, a few tools are implemented to aid the visualization of data, models, and results of simulations. pyPLD has been made to be a generic tool for simulations, not strictly bound to the example cases presented in this paper.

pyPLD can also be used to optimize the plume shape for a given purpose, and this might give input to the laser spot geometry.

For nc-PLD, pyPLD can also be used for simulating layered structures with or without a continuous substrate rotation. Simulations of CCS films can be done as demonstrated in this paper or with additional targets. Flat films with uniform doping can also be simulated by making layered films.

IX. CONCLUSIONS

In this work, we have carefully modeled the distribution of material deposited from a single laser pulse in PLD and have used this to simulate deposition of both single component thin films and films with a continuous compositional spread (CCS). We have expanded on existing work by using variable angle spectroscopic ellipsometry (VASE) to determine optical properties and thicknesses of the calibration films with a very high accuracy. This has enabled us to extend the model of the material distribution of the deposited material, resulting in a higher agreement between simulated and measured film thicknesses. We have used the improved model to simulate and optimize single component TiO_2 films for thickness uniformity and Cr and N doped TiO_2 CCS films for a Cr concentration profile of 2-8 at. %. The modeling and simulations have been implemented in an open-source library, pyPLD.

The methods presented in this paper can be used to advance the growth of both single component and CCS thin films fabricated using nc-PLD. By optimizing the deposition routine through simulations, less trial and error is needed to obtain the desired film composition and/or thickness variation across the substrate. Even though VASE has been our chosen method to determine the thickness maps for the calibration plume films, any technique to map the thickness can be used as input to the pyPLD library. Also, input from theoretical calculations, such as Monte Carlo simulations, of the material spread can be used. In addition to what has been presented in this paper, pyPLD can be used to design films with a desired thickness variation. This is, in particular, interesting for ellipsometry measurements, where the optical properties are more easily determined when the thickness is varying in a controlled manner. In this work, nc-PLD was used to deposit CCS films, but nc-PLD can also be used to deposit films with a uniform doping, and this can also be simulated and optimized using pyPLD.

Another potential use of pyPLD is that one can determine the plume shape needed for a particular film by varying the parameters in the mathematical model of the plume systematically and determining the material spread per pulse. This can be considered reversing the workflow in pyPLD, where the goal now is to find the ideal material spread, instead of staring with a measured material spread. When the desired material spread is determined, one can next derive the spot size and shape needed to create such a material spread. Currently, this can be done manually in pyPLD, but further development of pyPLD may automatize this functionality. A combination with plume dynamics modeling would be highly desirable. pyPLD can also be developed further to take into account sticking coefficients and volume of the deposited material that vary, e.g., as the films grow or as a function of distance from the plume center as well as varying laser fluence. Other users are invited to develop the library further.

ACKNOWLEDGMENTS

This work was supported by "Oxide based intermediate band materials" (RCN Project No. 240466) and the "Research Centre for Sustainable Solar Cell Technology" (FME SuSolTech, RCN Project No. 257639), co-sponsored by the Norwegian Research Council, research and industry partners. The Research Council of Norway is acknowledged for the support to the Norwegian Micro- and Nano-Fabrication Facility, NorFab (Project No. 295864). Herman Solstrand is acknowledged for acquiring the AFM images.

AUTHOR DECLARATIONS

Conflict of Interest

The authors have no conflicts to disclose.

Author Contributions

Hogne Lysne: Conceptualization (equal); Data curation (equal); Formal analysis (equal); Investigation (equal); Methodology (equal); Software (equal); Validation (equal); Visualization (equal); Writing – original draft (equal). **Thomas Brakstad:** Conceptualization (equal); Data curation (equal); Formal analysis (equal); Investigation (equal); Methodology (equal); Validation (equal); Visualization (equal); Writing – original draft (equal). **Morten Kildemo:** Formal analysis (equal); Supervision (equal); Writing – review & editing (equal). **Turid Reenaas:** Conceptualization (equal); Data curation (equal); Formal analysis (equal); Funding acquisition (equal); Methodology (equal); Project administration (equal); Supervision (equal); Validation (equal); Visualization (equal); Writing – original draft (equal).

DATA AVAILABILITY

The data that support the findings of this study are available from the corresponding author upon reasonable request.

REFERENCES

[1]D. B. Chrisey and G. K. Hubler, *Pulsed Laser Deposition of Thin Films* (Wiley, New York, 1994).
[2]R. Eason, *Pulsed Laser Deposition of Thin Films: Applications-Led Growth of Functional Materials* (John Wiley & Sons, Inc., 2006).
[3]I. N. Mihailescu and A. P. Caricato, *Pulsed Laser Ablation: Advances and Applications in Nanoparticles and Nanostructuring Thin Films* (Pan Stanford Publishing Pte. Ltd., 2018).
[4]L. Duta and A. C. Popescu, "Current research in pulsed laser deposition," Coatings **11**, 274 (2021).
[5]D. H. Blank, M. Dekkers, and G. Rijnders, "Pulsed laser deposition in Twente: From research tool towards industrial deposition," J. Phys. D: Appl. Phys. **47**, 034006 (2014).

[6]S. J. Guilfoyle, M. D. Crapper, M. Lovelady, and M. Petty, "Modelling of pulsed laser deposition of large area films," J. Magn. Magn. Mater. **198-199**, 113–115 (1999).
[7]J. A. Greer and M. D. Tabat, "Large-area pulsed laser deposition: Techniques and applications," J. Vac. Sci. Technol., A **13**, 1175–1181 (1995).
[8]Z. Vakulov, D. Khakhulin, E. Zamburg, A. Mikhaylichenko, V. A. Smirnov, R. Tominov, V. S. Klimin, and O. A. Ageev, "Towards scalable large-area pulsed laser deposition," Materials **14**, 4854 (2021).
[9]M. D. Nguyen, R. Tiggelaar, T. Aukes, G. Rijnders, and G. Roelof, "Wafer-scale growth of highly textured piezoelectric thin films by pulsed laser deposition for micro-scale sensors and actuators," J. Phys.: Conf. Ser. **922**, 012022 (2017).
[10]H. Yang, W. Wang, Z. Liu, and G. Li, "Epitaxial growth of 2 inch diameter homogeneous AlN single-crystalline films by pulsed laser deposition," J. Phys. D: Appl. Phys. **46**, 105101 (2013).
[11]P. J. McGinn, "Thin-film processing routes for combinatorial materials investigations—A review," ACS Comb. Sci. **21**, 501–515 (2019).
[12]M. L. Green, I. Takeuchi, and J. R. Hattrick-Simpers, "Applications of high throughput (combinatorial) methodologies to electronic, magnetic, optical, and energy-related materials," J. Appl. Phys. **113**, 231101 (2013).
[13]N. D. Bassim, P. K. Schenck, E. U. Donev, E. J. Heilweil, E. Cockayne, M. L. Green, and L. C. Feldman, "Effects of temperature and oxygen pressure on binary oxide growth using aperture-controlled combinatorial pulsed-laser deposition," Appl. Surf. Sci. **254**, 785–788 (2007).
[14]N. D. Bassim, P. K. Schenck, M. Otani, and H. Oguchi, "Model, prediction, and experimental verification of composition and thickness in continuous spread thin film combinatorial libraries grown by pulsed laser deposition," Rev. Sci. Instrum. **78**, 072203 (2007).
[15]S. C. Barron, J. M. Gorham, M. P. Patel, and M. L. Green, "High-throughput measurements of thermochromic behavior in $V_{1-x}Nb_xO_2$ combinatorial thin film libraries," ACS Comb. Sci. **16**, 526–534 (2014).
[16]C. Daumont, Q. Simon, S. Payan, P. Gardes, P. Poveda, M. Maglione, B. Negulescu, N. Jaber, and J. Wolfman, "Tunability investigation in the $BaTiO_3$-$CaTiO_3$-$BaZrO_3$ phase diagram using a refined combinatorial thin film approach," Coatings **11**, 1082 (2021).
[17]M. L. Green, P. K. Schenck, K. S. Chang, J. Ruglovsky, and M. Vaudin, "Higher-κ dielectrics for advanced silicon microelectronic devices: A combinatorial research study," Microelectron. Eng. **86**, 1662–1664 (2009).
[18]J. L. Klamo, P. K. Schenck, P. G. Burke, K. S. Chang, and M. L. Green, "Manipulation of the crystallinity boundary of pulsed laser deposited high-k HfO_2-TiO_2-Y_2O_3 combinatorial thin films," J. Appl. Phys. **107**, 054101 (2010).
[19]J. Sakai, J. M. C. Roque, P. Vales-Castro, J. Padilla-Pantoja, G. Sauthier, G. Catalan, and J. Santiso, "Control of lateral composition distribution in graded films of soluble solid systems $A_{1-x}B_x$ by partitioned dual-beam pulsed laser deposition," Coatings **10**, 540 (2020).
[20]H. von Wenckstern, M. Kneiß, A. Hassa, P. Storm, D. Splith, and M. Grundmann, "A review of the segmented-target approach to combinatorial material synthesis by pulsed-laser deposition," Phys. Status Solidi B **257**, 1900626 (2020).
[21]R. D. Snyder, E. L. Thomas, and A. A. Voevodin, "Material optimization via combinatorial deposition and analysis for thermoelectric thin films," Thin Solid Films **596**, 233–241 (2015).
[22]P. K. Schenck, N. D. Bassim, M. Otani, H. Oguchi, and M. L. Green, "Design and spectroscopic reflectometry characterization of pulsed laser deposition combinatorial libraries," Appl. Surf. Sci. **254**, 781–784 (2007).
[23]A. Bogaerts, Z. Chen, R. Gijbels, and A. Vertes, "Laser ablation for analytical sampling: What can we learn from modeling?," Spectrochim. Acta, Part B **58**, 1867–1893 (2003).
[24]M. Pelliccione and T. M. Lu, *Evolution of Thin Film Morphology*, Springer Series in Materials Science (Springer, Berlin, 2008), Vol. 108, pp. 1–200.
[25]R. Álvarez, A. Palmero, L. O. Prieto-López, F. Yubero, J. Cotrino, W. De La Cruz, H. Rudolph, F. H. Habraken, and A. R. Gonzalez-Elipe, "Morphological evolution of pulsed laser deposited ZrO_2 thin films," J. Appl. Phys. **107**, 054311 (2010).
[26]T. Wijnands, E. P. Houwman, G. Koster, G. Rijnders, and M. Huijben, "Numerical modeling of the plasma plume propagation and oxidation during pulsed laser deposition of complex oxide thin films," Phys. Rev. Mater. **4**, 103803 (2020).
[27]G. Socol, A. C. Galca, C. R. Luculescu, A. Stanculescu, M. Socol, N. Stefan, E. Axente, L. Duta, C. M. Mihailescu, V. Craciun, D. Craciun, V. Sava, and I. N. Mihailescu, "Tailoring of optical, compositional and electrical properties of the $In_xZn_{1-x}O$ thin films obtained by combinatorial pulsed laser deposition," Dig. J. Nanomater. Biostruct. **6**, 107–115 (2011).
[28]H. Fujiwara, *Spectroscopic Ellipsometry: Principles and Applications* (John Wiley & Sons, Inc., 2007).
[29]D. Necas and P. Klapetek, "Gwyddion: An open-source software for SPM data analysis," Cent. Eur. J. Phys. **10**, 181–188 (2012).
[30]J. E. Baker, "Secondary ion mass spectrometry," in *Practical Materials Characterization*, edited by M. Sard (Springer, New York, 2014), Chap. 4, pp. 133–188.
[31]C. M. Herzinger, B. Johs, W. A. McGahan, J. A. Woollam, and W. Paulson, "Ellipsometric determination of optical constants for silicon and thermally grown silicon dioxide via a multi-sample, multi-wavelength, multi-angle investigation," J. Appl. Phys. **83**, 3323–3336 (1998).
[32]W. Oldham, "Numerical techniques for the analysis of lossy films," Surf. Sci. **16**, 97–103 (1969).
[33]B. Johs and J. S. Hale, "Dielectric function representation by B-splines," Phys. Status Solidi A **205**, 715–719 (2008).
[34]H. Fujiwara, J. Koh, P. Rovira, and R. Collins, "Assessment of effective-medium theories in the analysis of nucleation and microscopic surface roughness evolution for semiconductor thin films," Phys. Rev. B: Condens. Matter **61**, 10832–10844 (2000).
[35]B. Johs and C. M. Herzinger, "Quantifying the accuracy of ellipsometer systems," Phys. Status Solidi C **5**, 1031–1035 (2008).
[36]R. Matarrese, I. Nova, A. Li Bassi, C. S. Casari, V. Russo, and S. Palmas, "Preparation and optimization of TiO_2 photoanodes fabricated by pulsed laser deposition for photoelectrochemical water splitting," J. Solid State Electrochem. **21**, 3139–3154 (2017).
[37]K. Järrendahl and H. Arwin, "Multiple sample analysis of spectroscopic ellipsometry data of semi-transparent films," Thin Solid Films **313-314**, 114–118 (1998).
[38]G. A. Niklasson, C. G. Granqvist, and O. Hunderi, "Effective medium models for the optical properties of inhomogeneous materials," Appl. Opt. **20**, 26 (1981).
[39]T. Galy, M. Marszewski, S. King, Y. Yan, S. H. Tolbert, and L. Pilon, "Comparing methods for measuring thickness, refractive index, and porosity of mesoporous thin films," Microporous Mesoporous Mater. **291**, 109677 (2020).
[40]J. Perrière, C. Hebert, N. Jedrecy, W. Seiler, O. Zanellato, X. Portier, R. Perez-Casero, E. Millon, and M. Nistor, "On the relevance of large scale pulsed-laser deposition: Evidence of structural heterogeneities in ZnO thin films," J. Appl. Phys. **116**, 123502 (2014).
[41]A. Ojeda-G-P, C. W. Schneider, M. Döbeli, T. Lippert, and A. Wokaun, "Angular distribution of species in pulsed laser deposition of $La_xCa_{1-x}MnO_3$," Appl. Surf. Sci. **336**, 150–156 (2015).

Paper 3

Thomas Brakstad, Hogne Lysne, Marcus Grand Michaelsen, Morten Kildemo, and Turid Reenaas

"nc-PLD of (Cr+N) co-doped TiO_2 for intermediate band solar cells PART 1: Challenges in N incorporation"

To be submitted to *Solar Energy Materials and Solar Cells*

Paper 4

Thomas Brakstad, Hogne Lysne, Andreas Rosnes, Marcus Grand Michaelsen, Morten Kildemo, Randi Holmestrand, and Turid Reenaas

"nc-PLD of (Cr+N) co-doped TiO_2 for intermediate band solar cells PART 2: Optical properties and micro structure"

To be submitted to *Solar Energy Materials and Solar Cells*

Paper 5

Katherine Inzani, Mohammadreza Nematollahi, Sverre M. Selbach, Tor Grande, Magnus Langøien Waalekalv, Thomas Brakstad, Turid Worren Reenaas, Morten Kildemo, and Fride Vollum-Bruer

"Tailoring properties of nanostructured MoO_{3-x} thin films by aqueous solution deposition"

Applied Surface Science **459** (2018), pp. 822-829

Applied Surface Science 459 (2018) 822–829

Contents lists available at ScienceDirect

Applied Surface Science

journal homepage: www.elsevier.com/locate/apsusc

Full Length Article

Tailoring properties of nanostructured MoO_{3-x} thin films by aqueous solution deposition

Katherine Inzani[a], Mohammadreza Nematollahi[b], Sverre M. Selbach[a], Tor Grande[a], Magnus Langøien Waalekalv[b], Thomas Brakstad[b], Turid Worren Reenaas[b], Morten Kildemo[b], Fride Vullum-Bruer[a,*]

[a] Department of Materials Science and Engineering, Norwegian University of Science and Technology, N-7491 Trondheim, Norway
[b] Department of Physics, Norwegian University of Science and Technology, N-7491 Trondheim, Norway

ARTICLE INFO

Keywords:
Molybdenum oxide
Nanostructured thin films
Solution processing
Optical properties

ABSTRACT

Molybdenum oxide films are required for a large range of optical, electronic and catalytic applications, and optimal film characteristics are similarly broad. Furthermore, the layered crystal structure of MoO_3 is suited to nanostructuring, which can be adapted to enhance the film properties. Here, we present a simple, aqueous route to MoO_3 thin films and attain nanostructured morphologies by control of solution parameters. Smooth and homogeneous thin films were achieved by control of the molecular species in solution by pH. The sensitivity of film quality to pH was demonstrated with the addition of PVA to the solution, which resulted in large spherical particulates on the surface. Film thickness was adjusted from 10 to 60 nm, whilst maintaining good film quality, by changing the solution concentration. Moreover, the grain size and nanocrystallite orientation varied with solution concentration. The importance of film morphology is revealed in the compositional changes of the films during hydrogen reduction, with differences in breakdown of film coverage and growth of reduced phases. Furthermore, spectroscopic ellipsometry was used to determine the optical properties of the films. This revealed changes in the dielectric function and band gap that were dependent on the level of reduction. The nanoscale morphologies presented demonstrate the potential to precisely control film morphology, dimensions, oxygen stoichiometry and phase composition by a low-cost wet chemical route.

1. Introduction

Molybdenum oxide is renowned for its multifunctionality, being utilized in catalysis [1], optoelectronic devices [2–5], electrochromic coatings [6], sensors [7], energy storage [8,9] and other emerging technologies [10–12], often in the form of a thin film. The electronic structure of molybdenum oxide is affected by its phase composition and oxygen stoichiometry, both of which can be adjusted to tune the electrical and optical properties [5,9,13,14]. In most cases, film morphology must also be controlled to achieve good device performance [3,6,8,15]. These factors vary widely with application. Where low-conductivity and charge carrier recombination is problematic, ultra-thin, smooth and amorphous films are utilized, for example as an anode buffer layer for optoelectronic devices [3]. Microstructures with high aspect ratios are used to enhance sensitivity to adsorbed species for sensors or to increase the surface area for catalysis [1,16]. In order to be incorporated into device manufacture, these application-tailored morphologies must be compatible with scalable and low-cost solution processes. Therefore, nanostructuring of MoO_3 should be developed within the wet chemical route.

The crystal structure of MoO_3 is unique: layers of MoO_6 corner- and edge-sharing octahedra are separated by a van der Waals gap of dispersed interactions, and oxygen sits on three symmetrically inequivalent sites, singly, doubly and triply coordinated to Mo ions. The variety of bonding environments results in differences in surface free energies with orientation, which lends itself well to nanostructuring of MoO_3 crystals. Nanosized flakes, sheets, rods, wires, walls, belts, plates, spheres and flowers have all been demonstrated by physical deposition processes [10,12,16–20]. The morphologies have been shown variously to enhance sensing properties, charge carrier mobility, field emission, photoluminescence, magnetic and electrochemical properties [10,12,16,18,20,21]. These morphology effects can be due to high crystallinity, 2D-geometries or controlled porosity. With molybdenum oxide thin films, specifications are similarly diverse. Some

* Corresponding author.
E-mail address: fride.vullum-bruer@ntnu.no (F. Vullum-Bruer).

https://doi.org/10.1016/j.apsusc.2018.07.196
Received 23 April 2018; Received in revised form 2 July 2018; Accepted 29 July 2018
Available online 30 July 2018
0169-4332/

optoelectronic devices rely on a low root mean square (RMS) roughness to limit recombination sites, and can utilize thin amorphous films [3]. In addition, optimum thickness is dependent on the application, for example, MoO_3 is used as a hole transport layer in both organic photovoltaics (OPV) and organic light emitting diodes (OLEDs), but the former requires ultra-thin films less than 10 nm thick to keep electrical resistance low, whereas the latter can incorporate films as thick as 150 nm, exploiting the resistivity as a short circuit barrier [14,22,23]. The mechanisms taking place in MoO_3 films are not always completely understood, and, especially in emerging technologies, the ideal film structure will evolve alongside device optimization.

Alongside film morphology, additional factors that affect device operation include phase composition, crystallinity and stoichiometry [9,14,24–27]. Some of these behaviours are not well understood. Stoichiometry in particular plays an important role in many applications, and the presence or absence of oxygen vacancies is critical to several devices [5,22,25,27]. Despite this, films of MoO_x can be incorporated without knowledge of the stoichiometry or even the composition and species present [28–31]. Changes in chemical bonding will obviously affect the properties of the films, and better understanding of the chemistry resultant from solution processing is necessary to controllably apply these films.

Nanoscale control of morphology is currently achievable through physical processing means, commonly vacuum evaporation, sputtering and pulsed laser deposition [9,14,22,24,32]. With atomic layer deposition, control of MoO_3 film thickness on the nanoscale has been achieved, with similar control of the growth in related chemical vapour deposition-type conditions [33]. Wet-chemical routes have the advantage of deposition in ambient conditions and low equipment costs. Furthermore, solution processing is often compatible with existing device manufacture such as organic photovoltaics. Previously, several solution routes to MoO_3 films have been used. Oxomolybdate precursors in aqueous solution have been used to provide molybdate based ultra-thin and low roughness films which have been comparable to evaporated films, despite that in most cases the films are discontinuous or have an undetermined composition [28,30,34,35]. Another route is via dissolution of molybdenum in hydrogen peroxide, which has resulted in thick nanocrystalline films, though also not continuously covering the substrate [1,6]. A recent synthesis involved dissolving MoO_3 ammonia solution, providing nanoplates whose concentration can be increased to provide a homogeneous film [3]. These films were used for investigation of the hole injection property in organic electronics, and the discontinuous film was found to give the best device performance. Templates have been used to provide ordering in the form of mesoporous films, but in general solution processing has failed to provide control of nanostructuring of MoO_3 [8].

Here, we present an investigation into nanostructuring of solution processed MoO_3 films and produce an aligned nanocrystallite thin film morphology via a simple solution route. We demonstrate control of morphology, thickness, crystallinity and phase composition by solution parameters and post-deposition annealing. Morphology and thickness, and hence electrical and optical properties, are controlled by standard solution properties such as pH and concentration. The changing morphology results in a change in the mechanism and kinetics of reduction. This is of importance when considering reduced MoO_3 films for use in optoelectronic devices.

2. Experimental details

2.1. Synthesis route and reduction

Solution and film preparation was done in an ISO7 cleanroom (NTNU NanoLab). Solutions for spin-coating films were made by dissolving ammonium heptamolybdate tetrahydrate ($(NH_4)_6Mo_7O_{24}{\cdot}4H_2O$, referred to as AHM, 99.98% trace metals basis, Sigma-Aldrich) in deionized water to concentrations of 0.1–1 mol [Mo] L^{-1}. To prevent precipitation of MoO_3, the solution was adjusted to pH 10 by adding ammonia solution. In some cases, an aqueous solution of 6 wt% poly(vinyl alcohol) (PVA) was added to increase the viscosity. Solutions were stirred on a hotplate at 50 °C for 30 min and then sonicated for 10 s for degassing. Quartz substrates (Spectrosil® synthetic fused silica, UQG Optics) were prepared by cleaning in ethanol and activating the surface with a 5 min oxygen plasma treatment. (Diener Electronic, FEMTO Plasma Cleaner). The films were prepared by spin coating, applying the solutions to the substrates through a syringe with a 0.2 µm filter (Acrodisc, Pall) and spin coating at 2500 rpm for 1 min (Laurell WS-400B-6NPP-Lite Spinner). Heat treatment of the films was done in a rapid thermal processing furnace (RTP, Jipelec JetFirst 200 Processor). A heating rate of 6 Ks^{-1} was used and the films were held at 400 °C for 10 min in an oxygen flow of 200 sccm. Multiple layers were added to the heat-treated films by the same route. For reduction of the films, RTP was done in 5% H_2-95% Ar flow of 1000 sccm, holding at 200–500 °C for 30 min.

2.2. Characterization

X-ray diffraction (XRD) was used to determine the phase composition of the films. A Bruker D8 Advance DaVinci X-ray Diffractometer with LynxEye™ SuperSpeed Detector was used with a CuKα radiation source in grazing-incidence geometry (grazing angle fixed at 1°, 0.03° step size, 3.2 s step time and 10–60° 2θ). Atomic force microscopy (AFM, Veeco diMultimode V, Nanoscope software), used to observe film morphology, was performed with Peak Force Tapping™ in ScanAsyst mode. Film thickness was measured by profilometry (Veeco Dektak 150), with a resolution of 6 nm, after etching a step to the substrate with a 0.05 M NaOH solution. Scanning electron microscopy (FEG-SEM, Zeiss Ultra 55 Limited Edition, 10 kV) was carried out to observe the homogeneity of films over a large area. This required films to be coated with a thin layer of carbon to prevent charging. X-ray photoelectron spectroscopy (XPS) was used to determine the oxidation states present after reduction. This was obtained with a Kratos Axis Ultra with monochromatic Al Kα X-ray source with a pass energy of 20 eV. Background modelling and subtraction, peak fitting, and quantification of the components were processed using CasaXPS software. Further details are given in supplementary information SI.1.

Supplementary data associated with this article can be found, in the online version, at https://doi.org/10.1016/j.apsusc.2018.07.196.

Spectroscopic ellipsometry (SE) measurements were performed on a J. A. Woollam Co. RC2 ellipsometer. The spectral range was 210–1690 nm (photon energy range 0.73–5.9 eV) at an angle of incidence 55–75°, with 5° intervals. Transmittance measurements of the substrate were also carried out with the ellipsometer and used to develop the SE model. Briefly, the parametric dispersion model consisted of two Tauc-Lorentz oscillators for describing the dielectric function above the band gap, one Gaussian for absorption below the band gap, and a Drude oscillator for free carrier contribution at low photon energies [36,37]. A roughness layer was modelled by Bruggeman effective medium theory [38]. Details of the optical model are given in supplementary information SI.2. The refractive index, film thickness and band gap were extracted from this, and agreement between the model and measured spectra was quantified by the mean squared error (MSE) [39].

3. Results and discussion

A molybdenum oxide film as-deposited from 0.1 mol [Mo] L^{-1} solution was shown to be amorphous by XRD, and no crystallinity was detected on thermal annealing up to 300 °C in oxygen (Fig. 1). Thermal annealing at 400 °C revealed the formation of crystalline MoO_3 in the film. The intensities of the Bragg reflections, however, did not correspond well with the MoO_3 reference, and only the (0 2 0), (0 4 0) and (0 6 0) planes displayed clear reflections. This strongly indicates that a preferred crystal orientation of MoO_3 formed during the crystallization

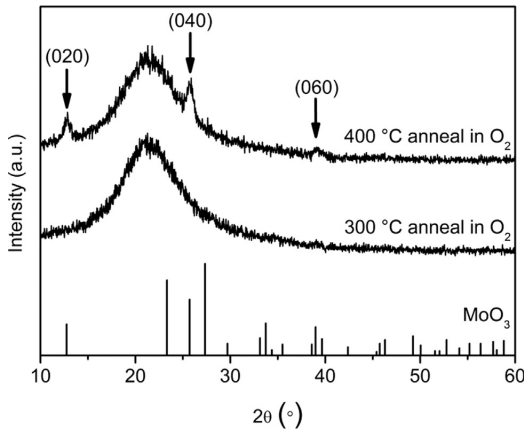

Fig. 1. Grazing-incidence XRD of deposited films after annealing in oxygen in at 300 °C and 400 °C, and XRD reference for MoO_3 (PDF 00-005-0508). The (0 2 0), (0 4 0) and (0 6 0) reflections of MoO_3 are labelled for the film annealed at 400 °C. The large amorphous background is attributable to the quartz substrate.

of the films.

As seen by AFM imaging in Fig. 2a, the as-deposited amorphous film covers the substrate homogenously. This can partly be attributed to the solution chemistry of the Mo^{6+} ion, which exists in the form of monomeric or polymeric oxo-ions, dependent on the pH and the concentration. The applied precursor AHM readily dissolves in water under the formation of the $Mo_7O_{24}^{6-}$ polyanion [40]. The pH of AHM in aqueous solution lies between 5 and 6, caused by the partial deprotonation of NH_4^+. Further lowering of the pH results in the formation of $Mo_8O_{26}^{4-}$ ions and finally in the precipitation of MoO_3. Raising the pH, however, causes the formation of monomeric MoO_4^{2-} ions [40]. The application of a high pH solution containing monomeric MoO_4^{2-} ions during spin coating prevents the risk of uncontrolled precipitation of MoO_3 in solution upon evaporation of the solvent. The monomeric oxomolybdate species are deposited on the substrate, providing a high quality film without inclusions.

Despite the lack of long range order after 300 °C annealing (XRD), morphology changes did occur at this temperature, evidenced by AFM (Fig. 2b). There appears to be clustering of nanoparticles, although homogeneous coverage is maintained across the surface. The morphology is very different after 400 °C annealing, and the film has a multicrystalline grain-like arrangement (Fig. 2c). The "grains" consist of platelet-like nanocrystallites, aligned in a pattern stacked from the centre of the grain and radiating outwards until intersecting alternatively oriented nanocrystallites of the neighbouring grain. The length of the plates is in excess of 100 nm and can be up to 1 μm. At the central point, a stepped arrangement reveals the plate edges. The height of the plates was determined by taking samples of line profiles and averaging the height difference in one step (Fig. 2d, with line profiles given in supplementary information SI.3). This gave an average height of 5 Å ± 2 Å. This value is of the order of one layer in the layered crystal lattice of MoO_3 (Fig. 2e) which is just less than half the unit cell height and equal to 6 Å [41]. Thus, it is likely that the exposed faces of the planes are the (0 2 0) planes of the lattice. This is justified by the lower surface energy of this face, intuitive from the fact that no Mo—O bonds are broken, and the strong {0 2 0} reflections seen by XRD.

Line profiles from the central part of a grain to its edges are given in the supplementary information (SI.4). The grain height increases from the central part to the edges of the grain, with a height difference of roughly 0.4–1 nm per 100 nm. This indicates that there is stacking from the centre to the edge of the grain, but the small height difference compared to the 6 Å layer height suggests that this stacking is not level with the surface.

Despite this nanostructuring, the films maintained full coverage of the substrate, and no large precipitates formed disrupting the continuity of the film. The films were smooth with an RMS roughness (Rq) of 0.85 nm, which is comparable to previously published values of amorphous films and is suitable for OPV applications. The film thickness was 10 nm, which is appropriate for the thinnest MoO_3 film applications. In order to obtain thicker films, the concentration of the deposition solution was increased. The annealing conditions were kept

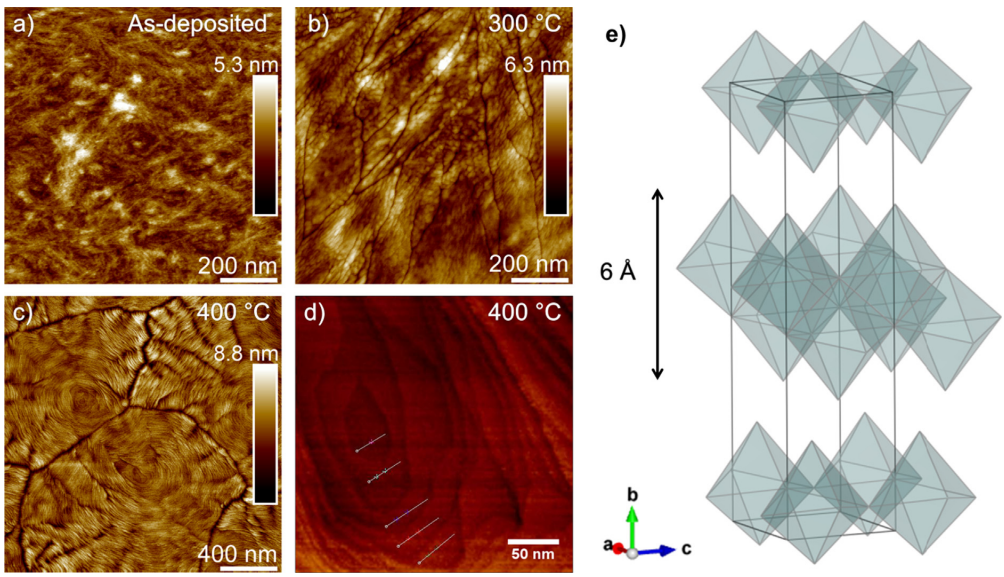

Fig. 2. AFM images of films deposited from a 0.1 mol [Mo] L^{-1} AHM solution. (a) As-deposited film. Films after heat treatment in O_2 at, (b) 300 °C and (c) 400 °C. (d) Sampling of line profiles to obtain nanocrystallite step height. (e) The layered crystal structure of orthorhombic MoO_3, with the layer height of 6 Å indicated.

Table 1
MoO_3 films with deposition solution concentration, film thickness, average grain size and root mean square roughness values measured by AFM over a 10 μm × 10 μm area.

Solution concentration [mol [Mo] L^{-1}]	Film thickness [nm ± 5 nm]	Average grain size [μm ± 0.1 μm]	RMS roughness, Rq [nm]
0.1	10	1.2	0.85
0.2	20	1.0	0.94
0.5	60	0.6	1.53
1.0	100	0.3	3.32

the same in all cases. The film thickness increased with increasing concentration in the solution, shown in Table 1. In addition, the average grain size decreased and Rq values increased with increasing concentration, also shown in Table 1. The decrease in grain size indicates that films are formed by heterogeneous nucleation and a higher nucleation rate occurs in formation of the thicker films. The orientation of the nanocrystallites also varies with film thickness (Figs. 3 and 5). Low concentrations result in the concentric and stepped alignment of plates. Whereas with higher concentrations, the majority of grains consisted of closely packed nanocrystallites oriented with {0 2 0} planes perpendicular to the surface. This change in nanocrystallite alignment can account for the increased Rq in the thicker films.

Although the 100 nm films would be applicable to many applications where thicker films are required, high concentrations

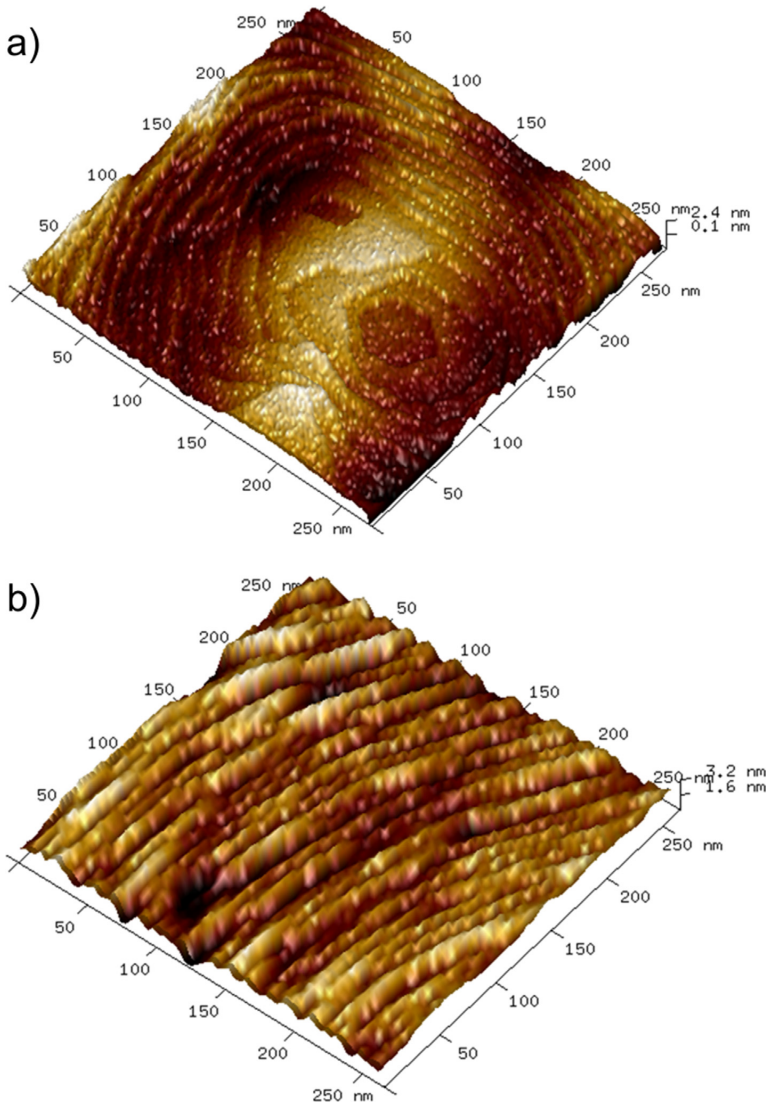

Fig. 3. AFM images of, (a) nanostructured stepped plates in a 0.1 mol [Mo] L^{-1} deposition film, and (b) oriented nanocrystallites in a 0.5 mol [Mo] L^{-1} deposition film.

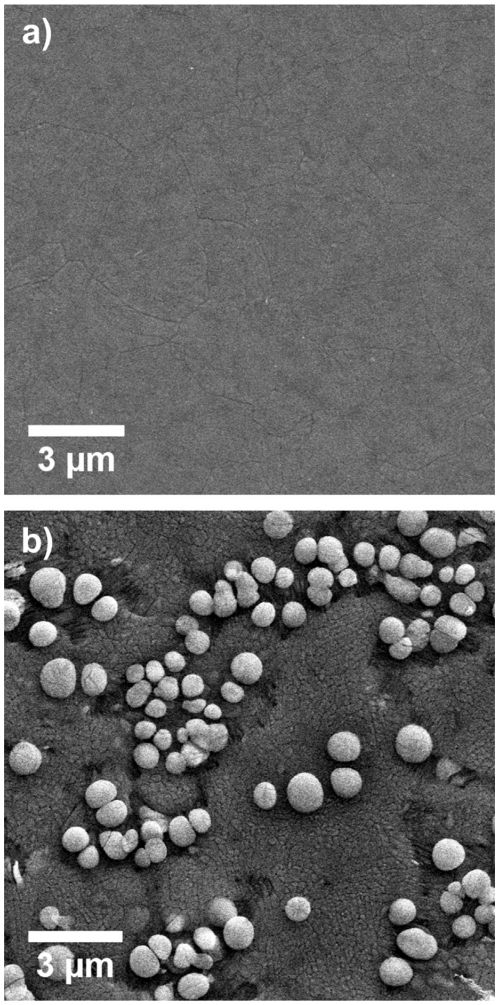

Fig. 4. SEM micrographs of MoO_3 films with PVA additive, (a) 1-layer deposition and (b) 3-layer deposition.

(≥ 0.75 mol [Mo] L^{-1}) resulted in precipitates in the solution or deposition stage. As a result, this gave a worsened film quality with particulates on the surface. The 0.5 mol [Mo] L^{-1} solution retained a good film quality and so it was the maximum concentration used for further film depositions. Alternative methods to increase the film thickness were attempted, including multiple layer depositions, and the addition of PVA solution to increase the viscosity. Multiple layers without the PVA additive had a negligible effect on film thickness. The addition of PVA does not alter the film quality, as shown in the homogeneous film surface scanning electron micrograph in Fig. 4a, nor does it have an effect on thickness. However, multiple layers with PVA additive resulted in the appearance of micron sized spheres distributed across the surface, seen in the SEM image of a film with three layers deposited, Fig. 4b.

The spheres are thought to be formed in solution after only a few hours ageing at room temperature. The oxomolybdate species tend to form large clusters at the low pH provided by the PVA molecules [42]. Another possibility is that the spheres form on the surface during deposition, on contact with the acidic MoO_3 surface of prior depositions. An alternative non-acidic additive for higher viscosity might limit this problem, but the acidic MoO_3 surface could still cause precipitation. Thus, single layer deposition was all that was required for optimum film quality and no additives were found necessary.

Post-treatment in a reducing atmosphere was performed to assess the effect of hydrogen reduction on films with minimum and maximum thickness. Films synthesized from 0.1 mol [Mo] L^{-1} and 0.5 mol [Mo] L^{-1} solutions were heated under a 5% H_2/95% Ar flow. Changes to the film morphology are shown in the AFM images in Fig. 5.

The grain structure is not affected in either of the film series at 200 °C post-treatment. At 300 °C treatment of the 0.1 mol [Mo] L^{-1} deposited film, the substrate is exposed at the grain boundaries. In addition, inclusions are seen within the film, which are likely nuclei of reduced molybdenum oxide phases. The 0.5 mol [Mo] L^{-1} deposited film does not show these changes at 300 °C reduction. Increasing to 400 °C, the 0.1 mol [Mo] L^{-1} deposited film has large areas of substrate exposed and dendritic phase growth is seen. In contrast, the 0.5 mol [Mo] L^{-1} deposited film remains intact and accommodates nuclei and plate like growth of reduced phases. At 500 °C, the 0.1 mol [Mo] L^{-1} deposited film has completely disintegrated and provides very little coverage of the surface. The 0.5 mol [Mo] L^{-1} deposited film exhibits large crystal growth and has a rough and inhomogeneous surface, which made it difficult to obtain a clear image by AFM.

XPS was done to assess the degree of reduction of the films. XPS spectra of the 0.1 mol [Mo] L^{-1} and 0.5 mol [Mo] L^{-1} depositions after reduction at 400 °C are shown in Fig. 6. Deconvolution of the Mo 3*d* peaks revealed the relative content of the Mo oxidation states, displayed with binding energy and FWHM in Table 2. There is a high proportion of Mo^{6+} in the 0.5 mol [Mo] L^{-1} film (91%), which suggests that the film remains mainly MoO_3. The remainder of Mo is Mo^{5+}. In the thinner 0.1 mol [Mo] L^{-1} film, only 61% of the Mo exists as Mo^{6+}. There is a greater proportion of Mo^{5+} (31%) in the 0.1 mol [Mo] L^{-1} film compared to the 0.5 mol [Mo] L^{-1} film. Mo^{5+} may be present due to oxygen vacancies or as Mo_4O_{11}, Mo_9O_{26} or $Mo_{18}O_{52}$ phases. It is unlikely that Mo^{5+} is a result of hydrogen doping, as atomic hydrogen would need to be dissociated, for example by a noble metal catalyst [43]. Without a catalyst, the reduction mechanism in hydrogen environment is known to progress through oxygen vacancy formation and reduced phase growth [44,45]. The concentration of isolated vacancies is expected to be small, as the formation of extended defects and reduced phases is favoured beyond $MoO_{2.999}$ [46].

About 8% of the Mo in the 0.1 mol [Mo] L^{-1} deposited film is Mo^{4+}, which could be present as MoO_2. The presence of MoO_2 in the 0.5 mol [Mo] L^{-1} deposited film is ruled out as there is no Mo^{4+} detected. There is no Mo^0, Mo^{2+}, or Mo^{3+} present in either of the films. The presence of Mo^{4+} and the higher concentration of Mo^{5+} in the 0.1 mol [Mo] L^{-1} deposited film reveal that it is reduced more rapidly than the 0.5 mol [Mo] L^{-1} deposited film.

The two series of films deposited from 0.1 mol [Mo] L^{-1} and 0.5 mol [Mo] L^{-1} solutions and treated with hydrogen reduction from 200 to 450 °C were further investigated by SE to understand the evolution of optical properties at different stages of reduction. Key parameters for the SE model and typical measured and fitted N, S, and C values are given in the supplementary information (SI.5 and SI.6). The model provided a good match to the measured transmittance (supplementary information SI.7) [47–52]. The transmittance spectra are also in keeping with other reports from literature, and the transmittance generally decreases with increasing reduction [27,53–55]. The total thickness of the films matches well to the thickness obtained by profilometry and the optical band gap of the non-treated sample is in good agreement with other observed values in the 3.2 eV region for MoO_3 (supplementary information SI.5) [47,48,56,57].

The dielectric function provides further insight to the phases introduced by reduction, especially for reduction temperatures above 400 °C (Fig. 7). The shape of the dielectric function is similar for all of

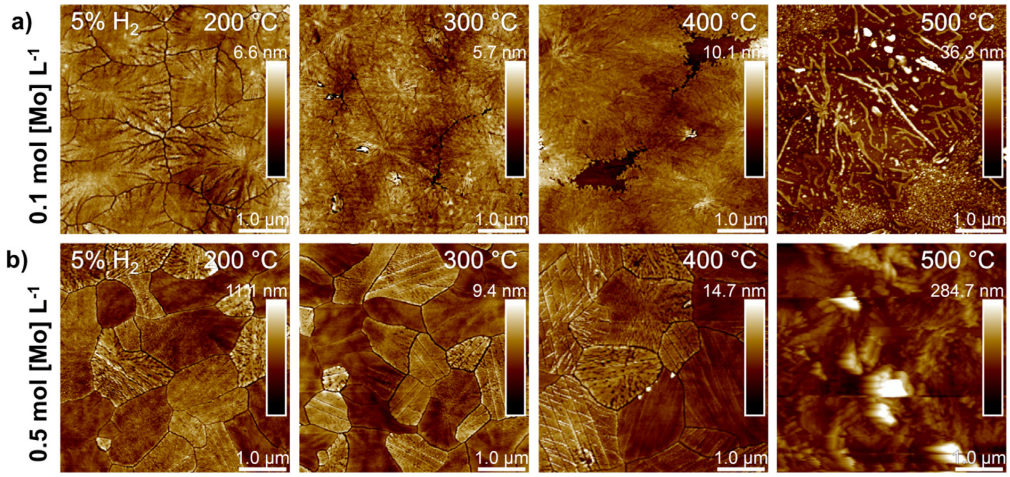

Fig. 5. AFM images of MoO_3 films from (a) 0.1 mol [Mo] L^{-1} solution and (b) 0.5 mol [Mo] L^{-1} solution after reduction in 5% H_2/95% Ar gas at 200 °C, 300 °C, 400 °C and 500 °C.

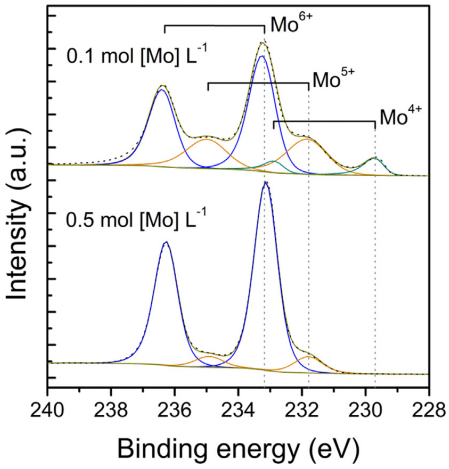

Fig. 6. XPS spectra of Mo 3*d* of two film thicknesses, 0.1 mol [Mo] L^{-1} and 0.5 mol [Mo] L^{-1} depositions, after hydrogen reduction treatment at 400 °C.

Table 2
Spectral fitting parameters for Mo $3d_{5/2}$ binding energy (eV), FWHM value (eV), and the relative content of 4+, 5+ and 6+ oxidation states of Mo (%). The distribution of oxidation states of molybdenum is found from deconvolution of both Mo $3d_{5/2}$ and Mo $3d_{3/2}$.

Film deposition [mol [Mo] L^{-1}]	Mo^{4+} Eb [eV] FWHM [eV] Content [%]	Mo^{5+} Eb [eV] FWHM [eV] Content [%]	Mo^{6+} Eb [eV] FWHM [eV] Content [%]
0.1	229.67 0.66 8%	231.77 1.45 31%	233.22 0.96 61%
0.5	– – –	231.79 1.04 9%	233.13 0.87 91%

the 0.5 mol [Mo] L^{-1} deposited films up to reduction temperature 350 °C, showing a mostly transparent region up to the band gap (Fig. 7c and d). This indicates that the films are mainly MoO_3 with few oxygen vacancies as they have almost no sub-band gap absorption. The same is true for the 0.1 mol [Mo] L^{-1} deposited films but only until the reduction temperature 200 °C (Fig. 7a and b). The very small contributions from the Gaussian, only 0.05–0.10 amplitude (SI.5), could be due to small concentrations of defects. At higher temperatures, the large contribution from the Gaussian indicates the presence of intermediate phases due to the position of their absorption bands, such as Mo_4O_{11} (1.3 eV, 2.13 eV and 2.42 eV) and Mo_9O_{26} (2.12 eV), or MoO_2 (2.48 eV) [57]. With the films from 0.1 mol [Mo] L^{-1} solution reduced at 350 °C, 400 °C and 450 °C, the higher amplitude at ~1.2 eV shows that there is a greater proportion of intermediate phases present in these films. This is in good agreement with the XPS results. Only the samples reduced at the highest temperature (450 °C) had significant contributions from free carriers at low photon energies. This is modelled by a Drude contribution and clearly indicates a metallic behaviour, most likely synonymous with the presence of MoO_2 [36,55].

Comparing ε_2 between the series (Fig. 7b and d), the more reduced samples of the 0.1 mol [Mo] L^{-1} deposited films have a higher dielectric function, again indicating that this series is more sensitive to reduction and evolve a greater proportion of reduced phases.

The evolution of reduced phases is in agreement with a previous work on the progression of reduction of MoO_3 [58]. It should be noted that the band gaps given by the Tauc analysis in the previous work include the contributions from the sub-band gap states, such that the Tauc band gap decreases with the onset of reduced phases. Here, the optical analysis accounts for the sub-band gap states with the Gaussian oscillator. Quantifying these reduced phases with ellipsometry would need further analysis, as polaron absorption has also been reported at approximately 1.4 eV [54].

Overall, the effect of reduction is greatly accelerated for the 0.1 mol [Mo] L^{-1} deposited films, with a greater proportion of reduced oxidation states. This occurs in combination with loss of material from the film, as seen by the decomposition of the film in Fig. 5, suggesting that the mechanism of reduction differs with film thickness. With the denser alignment of nanocrystallites, there is better tolerance against loss of oxygen and loss of Mo species is prevented. The 0.5 mol [Mo] L^{-1} deposited film allows the incorporation of oxygen vacancies and development and growth of reduced molybdenum oxide phases without breakdown of film coverage. This should be considered

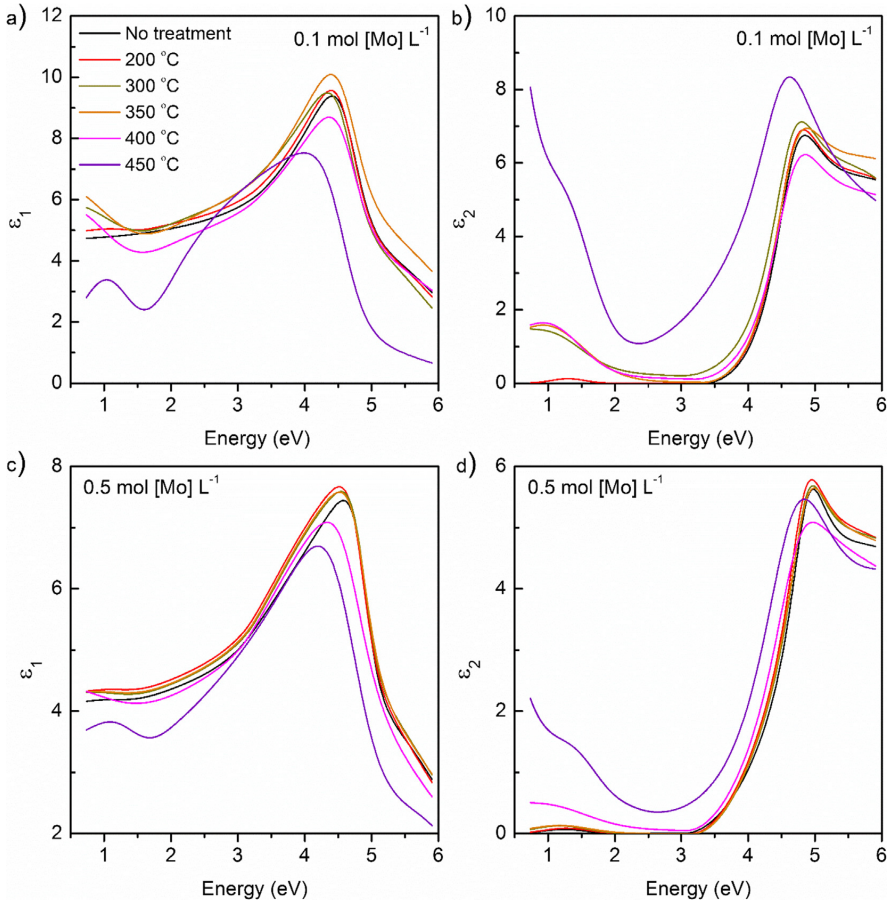

Fig. 7. SE model of the real and imaginary parts of the dielectric function for the films from 0.1 mol [Mo] L^{-1} solution (a) and (b), and 0.5 mol [Mo] L^{-1} solution (c) and (d) after reduction in 5% H_2-95% Ar gas at 200, 300, 350, 400 and 450 °C, and films with no treatment in reducing gas.

when applying thin films of MoO_3 to devices: a thin and smooth film is often used in a sub-stoichiometric state, and although the morphology is favourable for low carrier recombination and lower resistivity, a discontinuous coverage may quickly occur. It is possible that the nanocrystalline plates allow fast diffusion of species into and out of the structure and correspondingly faster reduction kinetics. In contrast, the thicker film morphology can provide a basis for well-developed reduced phases, which may also be enhanced by the layered structure.

4. Conclusions

A route to high quality, homogenous MoO_3 films with complete substrate coverage was demonstrated via deposition of monomeric molybdate species from aqueous solution. The amorphous as-deposited film crystallized by thermal annealing into a nanostructured arrangement of multicrystalline grains with ordering reflecting the layered crystal structure of MoO_3. The film morphology, including film thickness, grain size, and nanocrystallite orientation, was shown to be controlled by altering the solution concentration. As a consequence of the differing morphology, the kinetics and behaviours during reduction were modified. Films deposited from low concentration solution developed reduced phases at a lower temperature than films from a higher concentration solution, as determined by spectroscopic ellipsometry and X-ray photoelectron spectroscopy. However, these films with lower thickness exhibited film breakdown during reduction. In contrast, films deposited from higher concentration solution remained intact and allowed growth of new phases.

Acknowledgments

This work was performed within The Norwegian Research Centre for Solar Cell Technology project number 193829, a Centre for Environmentally-friendly Energy Research co-sponsored by the Research Council of Norway and research and industry partners in Norway. The Research Council of Norway is acknowledged for the support to the Norwegian Micro- and Nano-Fabrication Facility, NorFab, project number 245963/F50. NTNU NanoLab is acknowledged for support and subsidized use of their facilities.

Declaration of interests

None.

References

[1] E.M. Gaigneaux, K.I. Fukui, Y. Iwasawa, Morphology of crystalline α-MoO_3 thin

films spin-coated on Si (100), Thin Solid Films 374 (2000) 49–58.
[2] J. Meyer, P.R. Kidambi, B.C. Bayer, C. Weijtens, A. Kuhn, A. Centeno, A. Pesquera, A. Zurutuza, J. Robertson, S. Hofmann, Metal oxide induced charge transfer doping and band alignment of graphene electrodes for efficient organic light emitting diodes, Sci. Rep. 4 (2014) 5380.
[3] J. Liu, X. Wu, S. Chen, X. Shi, J. Wang, S. Huang, X. Guo, G. He, Low-temperature MoO_3 film from a facile synthetic route for an efficient anode interfacial layer in organic optoelectronic devices, J. Mater. Chem. C 2 (2014) 158–163.
[4] C. Battaglia, X. Yin, M. Zheng, I.D. Sharp, T. Chen, S. McDonnell, A. Azcatl, C. Carraro, B. Ma, R. Maboudian, et al., Hole selective MoO_x contact for silicon solar cells, NanoLetters 14 (2014) 967–971.
[5] D. Xiang, C. Han, J. Zhang, W. Chen, Gap states assisted MoO_3 nanobelt photodetector with wide spectrum response, Sci. Rep. 4 (2014) 4891.
[6] C.-S. Hsu, C.-C. Chan, H.-T. Huang, C.-H. Peng, W.-C. Hsu, Electrochromic properties of nanocrystalline MoO_3 thin films, Thin Solid Films 516 (2008) 4839–4844.
[7] M.M.Y.A. Alsaif, M.R. Field, B.J. Murdoch, T. Daeneke, K. Latham, A.F. Chrimes, A.S. Zoolfakar, S.P. Russo, J.Z. Ou, K. Kalantar-zadeh, Substoichiometric two-dimensional molybdenum oxide flakes: a plasmonic gas sensing platform, Nanoscale 6 (2014) 12780–12791.
[8] T. Brezesinski, J. Wang, S.H. Tolbert, B. Dunn, Ordered mesoporous α-MoO_3 with iso-oriented nanocrystalline walls for thin-film pseudocapacitors, Nat. Mater. 9 (2010) 146–151.
[9] H. Ohtsuka, Y. Sakurai, Characterization of MoO_{3-x} thin films, Jpn. J. Appl. Phys. 40 (2001) 4680–4683.
[10] H. Sinaim, D.J. Ham, J.S. Lee, A. Phuruangrat, S. Thongtem, T. Thongtem, Free-polymer controlling morphology of α-MoO_3 nanobelts by a facile hydrothermal synthesis, their electrochemistry for hydrogen evolution reactions and optical properties, J. Alloys Compd. 516 (2012) 172–178.
[11] D. Hanlon, C. Backes, T.M. Higgins, M. Hughes, A. O'Neill, P. King, N. McEvoy, G.S. Duesberg, B. Mendoza Sanchez, H. Pettersson, et al., Production of molybdenum trioxide nanosheets by liquid exfoliation and their application in high-performance supercapacitors, Chem. Mater. 26 (2014) 1751–1763.
[12] Y. Shen, S. Deng, Y. Zhang, F. Liu, J. Chen, N. Xu, Highly conductive vertically aligned molybdenum nanowalls and their field emission property, Nanoscale Res. Lett. 7 (2012) 463.
[13] X.-B. Shi, M.-F. Xu, D.-Y. Zhou, Z.-K. Wang, L.-S. Liao, Improved cation valence state in molybdenum oxides by ultraviolet-ozone treatments and its applications in organic light-emitting diodes, Appl. Phys. Lett. 102 (2013) 233304.
[14] S.Y. Chiam, B. Dasgupta, D. Soler, M.Y. Leung, H. Liu, Z.E. Ooi, L.M. Wong, C.Y. Jiang, K.L. Chang, J. Zhang, Investigating the stability of defects in MoO_3 and its role in organic solar cells, Sol. Energy Mater. Sol. Cells 99 (2012) 197–203.
[15] W.-Q. Yang, Z.-R. Wei, X.-H. Zhu, D.-Y. Yang, Strong influence of substrate temperature on the growth of nanocrystalline MoO_3 thin films, Phys. Lett. A 373 (2009) 3965–3968.
[16] M. Shafiei, J. Yu, M. Breedon, N. Motta, Q. Wu, Z. Hu, L. Qian, K. Kalantar-zadeh, W. Wlodarski, Hydrogen gas sensors based on thermally evaporated nanostructured MoO_3 Schottky Diode: a comparative study, IEEE Sensors 8–11 (2011), https://doi.org/10.1109/ICSENS.2011.6126970.
[17] O. Goiz, F. Chávez, C. Felipe, N. Morales, R. Peña-Sierra, Synthesis of molybdenum oxide microsheets via close-spaced vapor transport, Mater. Sci. Eng. B Solid-State Mater. Adv. Technol. 174 (2010) 174–176.
[18] S. Balendhran, J. Deng, J.Z. Ou, S. Walia, J. Scott, J. Tang, K.L. Wang, M.R. Field, S. Russo, S. Zhuiykov, et al., Enhanced charge carrier mobility in two-dimensional high dielectric molybdenum oxide, Adv. Mater. 25 (2013) 109–114.
[19] Y.B. Li, Y. Bando, D. Golberg, K. Kurashima, Field emission from MoO_3 nanobelts, Appl. Phys. Lett. 81 (2002) 5048–5050.
[20] I. Navas, R. Vinodkumar, V.P. Mahadevan Pillai, Self-assembly and photoluminescence of molybdenum oxide nanoparticles, Appl. Phys. A 103 (2011) 373–380.
[21] F. Li, Z. Chen, Tuning electronic and magnetic properties of MoO_3 sheets by cutting, hydrogenation, and external strain: a computational investigation, Nanoscale 5 (2013) 5321–5333.
[22] X. Haitao, Z. Xiang, Investigation of hole injection enhancement by MoO_3 buffer layer in organic light emitting diodes, J. Appl. Phys. 114 (2013) 244505.
[23] J. Liang, F.-S. Zu, L. Ding, M.-F. Xu, X.-B. Shi, Z.-K. Wang, L.-S. Liao, Aqueous solution-processed MoO_3 thick films as hole injection and short-circuit barrier layer in large-area organic light-emitting devices, Appl. Phys. Express 7 (2014) 111601.
[24] M. Rouhani, Y.L. Foo, J. Hobley, J. Pan, G.S. Subramanian, X. Yu, A. Rusydi, S. Gorelik, Photochromism of amorphous molybdenum oxide films with different initial Mo^{5+} relative concentrations, Appl. Surf. Sci. 273 (2013) 150–158.
[25] B. Dasgupta, Y. Ren, L.M. Wong, L. Kong, E.S. Tok, W.K. Chim, S.Y. Chiam, Detrimental effects of oxygen vacancies in electrochromic molybdenum oxide, J. Phys. Chem. C 119 (2015) 10592–10601.
[26] T.S. Sian, G.B. Reddy, Optical, structural and photoelectron spectroscopic studies on amorphous and crystalline molybdenum oxide thin films, Sol. Energy Mater. Sol. Cells 82 (2004) 375–386.
[27] S.-Y. Lin, Y.-C. Chen, C.-M. Wang, P.-T. Hsieh, S.-C. Shih, Post-annealing effect upon optical properties of electron beam evaporated molybdenum oxide thin films, Appl. Surf. Sci. 255 (2009) 3868–3874.
[28] J.J. Jasieniak, J. Seifter, J. Jo, T. Mates, A.J. Heeger, A Solution-processed MoO_x anode interlayer for use within organic photovoltaic devices, Adv. Funct. Mater. 22 (2012) 2594–2605.
[29] Q. Fu, J. Chen, C. Shi, D. Ma, Room-temperature sol-gel derived molybdenum oxide thin films for efficient and stable solution-processed organic light-emitting diodes, ACS Appl. Mater. Interfaces 5 (2013) 6024–6029.
[30] W. Qiu, A. Hadipour, R. Müller, B. Conings, H. Boyen, P. Heremans, L. Froyen, Ultrathin ammonium heptamolybdate films as efficient room-temperature hole transport layers for organic solar cells, ACS Appl. Mater. Interfaces 6 (2014) 16335–16343.
[31] P.Y. Ho, J.Y. Sun, S.H. Kao, C.Y. Kao, S.H. Lin, S. Lan, W.H. Tseng, C.I. Wu, C.F. Lin, The effects of MoO_3 treatment on inverted PBDTTT-C:PC $_{71}$BM solar cells, Sol. Energy Mater. Sol. Cells 119 (2013) 235–240.
[32] K. Majhi, L. Bertoluzzi, K.J. Rietwyk, A. Ginsburg, D.A. Keller, P. Lopez-Varo, A.Y. Anderson, J. Bisquert, A. Zaban, Combinatorial investigation and modelling of MoO_3 hole-selective contact in $TiO_2|Co_3O_4|MoO_3$ all-oxide solar cells, Adv. Mater. Interfaces 3 (2016) 1500405.
[33] M. Diskus, O. Nilsen, H. Fjellvåg, Growth of thin films of molybdenum oxide by atomic layer deposition, J. Mater. Chem. 21 (2011) 705–710.
[34] F. Liu, S. Shao, X. Guo, Y. Zhao, Z. Xie, Efficient polymer photovoltaic cells using solution-processed MoO_3 as anode buffer layer, Sol. Energy Mater. Sol. Cells 94 (2010) 842–845.
[35] S. Murase, Y. Yang, Solution processed MoO_3 interfacial layer for organic photovoltaics prepared by a facile synthesis method, Adv. Mater. 24 (2012) 2459–2462.
[36] T.E. Tiwald, D.W. Thompson, J.A. Woollam, W. Paulson, R. Hance, Application of IR variable angle spectroscopic ellipsometry to the determination of free carrier concentration depth profiles, Thin Solid Films 313–314 (1998) 661–666.
[37] G. Jellison Jr, F. Modine, Parameterization of the optical functions of amorphous materials in the interband region, Appl. Phys. Lett. 69 (1996) 371–373.
[38] H. Fujiwara, J. Koh, P.I. Rovira, R.W. Collins, Assessment of effective-medium theories in the analysis of nucleation and microscopic surface roughness evolution for semiconductor thin films, Phys. Rev. B 61 (2000) 10832.
[39] B. Johs, C.M. Herzinger, Quantifying the accuracy of ellipsometer systems, Phys. Status Solidi C 5 (2008) 1031–1035.
[40] J. Aveston, E.W. Anacker, J.S. Johnson, Hydrolysis of molybdenum(VI). Ultracentrifugation, acidity measurements, and Raman spectra of polymolybdates, Inorg. Chem. 3 (1964) 735–746.
[41] L. Kihlborg, Least squares refinement of the crystal structure of molybdenum trioxide, Ark. för Kemi 21 (1963) 357–364.
[42] S. Borg, W. Liu, B. Etschmann, Y. Tian, J. Brugger, An XAS study of molybdenum speciation in hydrothermal chloride solutions from 25–385 °C and 600 bar, Geochim. Cosmochim. Acta 92 (2012) 292–307.
[43] A. Borgschulte, O. Sambalova, R. Delmelle, S. Jenatsch, R. Hany, F. Nüesch, Hydrogen reduction of molybdenum oxide at room temperature, Sci. Rep. 7 (2017) 40761.
[44] M.J. Kennedy, S.C. Bevan, A kinetic study of the reduction of molybdenum trioxide by hydrogen, J. Less-Common Met. 36 (1974) 23–30.
[45] E. Lalik, W.I.F. David, P. Barnes, J.F.C. Turner, Mechanisms of reduction of MoO_3 to MoO_2 reconciled? J. Phys. Chem. B 105 (2001) 9153–9156.
[46] L.A. Bursill, Crystallographic shear in molybdenum trioxide, Proc. R. Soc. Lond. A. Math. Phys. Sci. 311 (1969) 267–290.
[47] T. Ivanova, A. Szekeres, M. Gartner, D. Gogova, K.A. Gesheva, Spectroscopic characterization of CVD-molybdenum oxide films, Electrochim. Acta 46 (2001) 2215–2219.
[48] A. Szekeres, T. Ivanova, K. Gesheva, Spectroscopic ellipsometry study of CVD molybdenum oxide films: effect of temperature, J. Solid State Electrochem. 7 (2002) 17–20.
[49] A. Arfaoui, B. Ouni, S. Touihri, A. Mhamdi, A. Labidi, T. Manoubi, Effect of annealing in a various oxygen atmosphere on structural, optical, electrical and gas sensing properties of Mo_xO_y thin films, Opt. Mater. (Amst.) 45 (2015) 109–120.
[50] A. Boukhachem, O. Kamoun, C. Mrabet, C. Mannai, N. Zouaghi, A. Yumak, K. Boubaker, M. Amlouk, Structural, optical, vibrational and photoluminescence studies of Sn-doped MoO_3 sprayed thin films, Mater. Res. Bull. 72 (2015) 252–263.
[51] I. Kostis, N. Vourdas, G. Papadimitropoulos, A. Douvas, M. Vasilopoulou, N. Boukos, D. Davazoglou, Effect of the oxygen sub-stoichiometry and of hydrogen insertion on the formation of intermediate bands within the gap of disordered molybdenum oxide Films, J. Phys. Chem. C 117 (2013) 18013–18020.
[52] M. Itoh, K. Hayakawa, S. Oishi, Optical properties and electronic structures of layered MoO_3 single crystals, J. Phys. Condens. Matter 13 (2001) 6853–6864.
[53] H. Simchi, B.E. McCandless, T. Meng, J.H. Boyle, W.N. Shafarman, Characterization of reactively sputtered molybdenum oxide films for solar cell application, J. Appl. Phys. 114 (2013) 13503.
[54] S.H. Mohamed, O. Kappertz, J.M. Ngaruiya, T.P.L. Pedersen, R. Drese, M. Wuttig, Correlation between structure, stress and optical properties in direct current sputtered molybdenum oxide films, Thin Solid Films 429 (2003) 135–143.
[55] K. Inzani, M. Nematollahi, F. Vullum-Bruer, T. Grande, T.W. Reenaas, S.M. Selbach, Electronic properties of reduced molybdenum oxides, Phys. Chem. Chem. Phys. 19 (2017) 9232–9245.
[56] F. Hamelmann, A. Brechling, A. Aschentrup, U. Heinzmann, P. Jutzi, J. Sandrock, U. Siemeling, T. Ivanova, A. Szekeres, K. Gesheva, Thin molybdenum oxide films produced by molybdenum pentacarbonyl 1-methylbutylisonitrile with plasma-assisted chemical vapor deposition, Thin Solid Films 446 (2004) 167–171.
[57] V.R. Porter, W.B. White, R. Roy, Optical spectra of the intermediate oxides of titanium, vanadium, molybdenum, and tungsten, J. Solid State Chem. 4 (1972) 250–254.
[58] K. Inzani, M. Nematollahi, S.M. Selbach, T. Grande, F. Vullum-Bruer, Progression of reduction of MoO_3 observed in powders and solution-processed films, Thin Solid Films 626 (2017) 94–103.

Paper 6

Marina Jorge, Thomas Brakstad, Mohammadreza Nematollahi, Morten Kildemo, and Turid Reenaas

"Sub-stochiometric MoO_3 for intermediate band solar cells"

In 2019 IEEE 46th Photovoltaic Specialists Conference (PVSC). IEEE 2019, pp. 1756-1759.

Paper 7

Thomas Brakstad, Benjamin R. Hope, Mohammadreza Nematollahi, Morten Kildemo, Nikolas J. Podraza, Kiran Ghimire, and Turid W. Reenaas

"Ellipsometric study of the optical response of ZnS:Cr for PV applications"

Applied Surface Science **421** (2017), pp. 315-319

Applied Surface Science 421 (2017) 315–319

Contents lists available at ScienceDirect

Applied Surface Science

journal homepage: www.elsevier.com/locate/apsusc

Full Length Article

Ellipsometric study of the optical response of ZnS:Cr for PV applications

Thomas Brakstad[a,*], Benjamin R. Hope[a], Mohammadreza Nematollahi[a], Morten Kildemo[a], Nikolas J. Podraza[b], Kiran Ghimire[b], Turid W. Reenaas[a]

[a] Norwegian University of Science and Technology (NTNU), 7491 Trondheim, Norway
[b] University of Toledo, 2600 Dorr St., Toledo, OH 43606, USA

ARTICLE INFO

Article history:
Received 31 July 2016
Received in revised form 23 October 2016
Accepted 24 October 2016
Available online 26 October 2016

Keywords:
Ellipsometry
Cr doped ZnS
ZnS
Dielectric function

ABSTRACT

Optical properties of highly chromium doped (2–4 at.%) zinc sulfide made by pulsed laser deposition have been studied by spectroscopic ellipsometry in the spectral range of 0.73–5.90 eV. The characteristic optical features of the ZnS are a direct bandgap with absorption onset at 3.6 eV, with E_0, E_1 and E_2 critical points around 3.7, 5.7 and 7 eV. Excitonic effects were observed to be strong in this material – in line with the literature. The sub-bandgap absorption accredited to the chromium doping appears as a broad sub-bandgap feature increasing monotonously with increased doping concentration at a given growth temperature. In this report, we discuss three different approaches to extract and analyze the optical properties in terms of the complex dielectric function.

1. Introduction

An intermediate band solar cell (IBSC) is based on a semiconductor where a narrow, intermediate energy band (IB) is present within the bandgap (E_g) [1]. This additional band allows for better utilization of both low and high energy photons in the solar spectrum, as sub-bandgap light can excite electrons from the valence band (VB) to the IB and from the IB to the conduction band (CB). This increases the photo-generated current while maintaining a high open circuit voltage. The maximum theoretical efficiency (for fully concentrated light) of such a solar cell is as high as 63.2%, in comparison to a limit of 40.7% for a conventional solar cell under the same operating conditions [1]. Different approaches have been pursued, but the challenge remains to fabricate an IB material with suitable properties to obtain an IBSC with higher efficiency than a conventional solar cell [2].

ZnS is a well-studied and abundant material, which is interesting with regards to IBSC application. This is due to 1), an isolated, partially filled IB has been predicted by ab initio studies of Cr-doped ZnS [3,4], and 2), ZnS has a very large bandgap, (E_g ~3.6–3.9 eV) [5], which would make it easier to create an isolated IB within the bandgap with its own quasi-fermi level (QFL) when the solar cell is illuminated.

Undoped ZnS have been studied earlier using spectroscopic ellipsometry (SE), to obtain the optical constants of both zinc blende (ZB) [6,7] and wurtzite (WZ) [8] crystal structures. Doped ZnS has also been studied for various dopants, but only a few reports are found on ZnS:Cr [9,10] and none for very high dopant concentrations (2–4 at.%) which is needed for suppressing non-radiative recombination [11]. The complex dielectric function ($\varepsilon = \varepsilon_1 + i\varepsilon_2$) gives information on the material's electronic band structure, density of filled and empty states, magnitude of optical probability of a transition between filled and empty states, and excitonic absorption [12], and is therefore a highly important property to characterize.

In this work, we discuss three different approaches to model ε from room temperature ex situ spectroscopic ellipsometric data. Of particular importance is to understand how the Cr doping alters the dielectric function below the ZnS bandgap. Three different models for the optical response were applied, and these are presented below.

2. Experimental details

The ZnS and ZnS:Cr films were grown by pulsed laser deposition (PLD) on Si and quartz substrates. Prior to depositions, the substrates were cleaned using acetone, isopropanol, and deionized water. The Si substrates were etched in 5% HF for 3 min followed by 3 min rinsing in deionized water, and annealing at 850 C for 2 min in the PLD chamber. Then, the substrate temperature was reduced

* Corresponding author.
E-mail address: thomas.brakstad@ntnu.no (T. Brakstad).

http://dx.doi.org/10.1016/j.apsusc.2016.10.157
0169-4332/

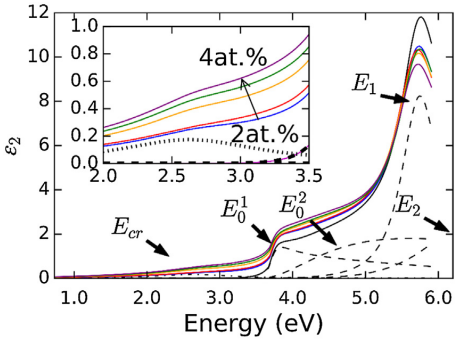

Fig. 1. ε_2 plotted for undoped (black) and different at.% of Cr (blue, red, orange, green and purple for 2.0, 2.3, 3.0, 3.3, and 4.0 at.%, respectively) ZnS films. The resulting lineshape from each oscillator for undoped ZnS is plotted in black, dashed lines, while the contribution for 4.0 at.% of the doped samples (black, dash-dotted line) are given as an example of below bandgap contribution. (For interpretation of the references to color in this figure legend, the reader is referred to the web version of this article.)

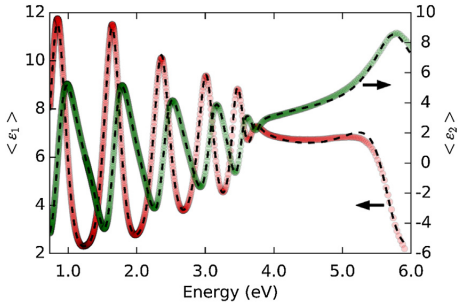

Fig. 2. The as-measured (colored circles) and simulated (black dotted lines) complex pseudo dielectric function (<ε>) for 4 at.% Cr-doped ZnS film. $<\varepsilon_1>$ is plotted in red, while $<\varepsilon_2>$ is plotted in green. The arrows indicate the corresponding axis. (For interpretation of the references to color in this figure legend, the reader is referred to the web version of this article.)

to the growth temperature, i.e. 500 C and 550 C for undoped and doped films, respectively. A KrF excimer laser (Lambda Physics COMPex Pro 110, 248 nm, 20 ns) was operated at 5 Hz to ablate a polycrystalline $(ZnS)_{0.94}Cr_{0.06}$ target. The Cr content in the films was varied between 2 and 4 at.% by varying the laser fluence in the range 1.0–4.3 J/cm^2 as elaborated in Ref. [13]. The films were between 160 and 660 nm thick [14].

The optical properties of the films were determined using a dual rotating compensator variable angle spectroscopic ellipsometry (VASE) (RC2, J.A. Woollam Co.) in the wavelength range 210–1690 nm (photon energy range 0.73–5.90 eV). Spectra were recorded at incidence angles of 60–75°, with 2.5° increments. In addition, VUV-VASE was used for measurements of selected samples in the 4.0–8.5 eV range.

3. Results and discussion

3.1. Modeling details

All ZnS layers were modelled as a homogeneous thin film on a semi-infinite c-Si substrate covered by a native oxide. A simple Bruggeman effective medium approximation (BEMA) consisting of 50/50 void/ZnS for the undoped samples, and void/ZnS:Cr for the doped samples, was used to model the surface roughness [15]. Surface roughness's were compared to atomic force microscopy (AFM) measurements from Ref. [16], and the films were in general found to be very smooth, with root mean squared roughness values of 1.2–2.8 nm [16]. The roughness, native oxide and ZnS layer thicknesses were all fitted. The agreement between the optical model and the measured ellipsometric spectra (in $N = \cos 2\Psi$, $C = \sin 2\Psi \cos\Delta$, $S = \sin 2\Psi \sin\Delta$) was quantified by the mean squared error (MSE) [17].

3.2. Harmonic oscillator dispersion model

In this approach, the main features of the ZnS layer was modelled by one Cody-Lorentz oscillator with an Urbach tail (labeled E_0^1 in Fig. 1) corresponding to a 3D exciton (according to Ozaki and Adachi [6]), and a Tauc Lorentz oscillator (E_1) modelling the E_1-CP, which is dominated by an exciton. The model was refined to include one Tauc Lorentz oscillator (E_0^2 in Fig. 1), which resembles the E0/E0 + Δ critical point found by Ozaki and Adachi. The two Tauc Lorentz oscillators used the same bandgap value (E_g). Indeed, this was motivated by Ozaki and Adachi [6] dispersion model describing the absorption at the bandgap edge by a combination of an exciton lineshape and a 3D-CP. The E_2-CP and other high energy transitions were grouped into a Gaussian oscillator, (mainly from the E_2-CP around 7 eV). These lineshape-components are shown in Fig. 1 (black dashed lines), along with the resulting imaginary part of the dielectric function (full black line). The other, colored curves above the black lineshape is ε_2 for various amount of Cr in the ZnS films ranging from 2.0 to 4.0 at.% Cr.

Table 1
Parameters for the harmonic oscillator model as a function of Cr content. E_g was here 3.56 eV and $\varepsilon_\infty = 1$. The Cody Lorentz parameters were $E_p = 3.0$, $E_t = 0.109$ and $E_u = 0.129$ eV. Broadening and the position of the E_{cr} Lorentzian oscillator was set to $\Gamma_{Cr} = 0.85$ and $E_{cr} = 2.68$ eV. E_1 is the position for the center of oscillator, A_1 is the amplitude, Γ_1 is the broadening, and A_{cr} is the amplitude of the Cr contribution.

	ZnS	2.0 at.%	2.3 at.%	3.0 at.%	3.3 at.%	4.0 at.%
E_1 (eV)	5.73	5.70	5.68	5.69	5.71	5.68
A_1	36.50	32.37	32.41	32.02	30.93	29.06
Γ_1 (eV)	0.54	0.66	0.67	0.69	0.66	0.68
A_{cr}	N/A	0.06	0.04	0.08	0.09	0.10

The as-measured pseudo dielectric function of a typical doped ZnS film is shown in Fig. 2. We note the sharp cut-off of the interference fringes at the bandgap, around 3.7 eV related to the E_0-CP, and the strong feature around 5.7 eV related to the E_1-CP.

The E_0^1 shape in our model is much broader than the excitonic peak in the Ozaki and Adachi model [6]. The E_1 peak was for simplicity modelled by a Tauc-Lorentz oscillator, rather than an exciton lineshape, in order to insure cut-off at the bandgap.

To account for new states in the bandgap when doping ZnS with Cr, one Lorenz oscillator, with center energy (E_{Cr}) was added to account for the increased absorption below the bandgap. The lineshape contribution for 4 at.% Cr is seen in Fig. 1, and the complete model shows a good agreement with the data, as exemplified in Fig. 2. The large number of parameters was compensated for by performing a multi sample analysis of all samples, and some main parameters are shown in Table 1.

The E_1 amplitude in Fig. 1 is reduced significantly for 4 at.% of Cr compared to the undoped sample. Between 2.0% and 3.3% doping content, the E_1 peak is only slightly reduced or not reduced at all. The peak amplitude of the E_1 peak is reduced following the introduction of doping, but no significant change in its energy position or the broadening of the peak can be seen from Fig. 1 or Table 1.

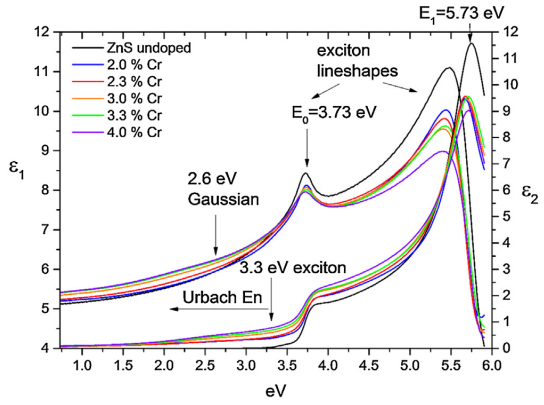

Fig. 3. Dielectric functions determined using the numerical CPPB model modified by the Urbach tail. Black, blue, red, orange, green, and purple for undoped ZnS, 2.0, 2.3, 3.0, 3.3, and 4.0 at.% Cr content, respectively. (For interpretation of the references to color in this figure legend, the reader is referred to the web version of this article.)

3.3. CPPB dispersion model modified by an Urbach tail

A model which incorporates critical point parabolic band (CPPB) dispersion for all the CPs, but which falls off sufficiently fast in order to correctly model the interference fringes and the weak sub-bandgap absorption, as in Figs. 2 and 4, has recently been proposed [18]. The idea is that the below bandgap absorption tail of the CPs are multiplied by the Urbach tail, as in the Tauc-Lorentz model [19,20]. In our implementation the dispersion model is described by:

$$\varepsilon_1(E) = \varepsilon_\infty + \frac{A}{E_{res}^2 - E^2} + \frac{2}{\pi} P \int_0^\infty \frac{\zeta \varepsilon_2(\zeta)}{\zeta^2 - E^2} d\zeta, \quad (1)$$

where the imaginary part is for simplicity given by the sum of only exciton line shapes:

$$\varepsilon_2(E) = \begin{cases} \varepsilon_{2,Gauss}(E) + \varepsilon_{2,CPPB}(E_g)\, e^{-\frac{(E_g - E)}{E_u}}, & E < E_g \\ \varepsilon_{2,Gauss}(E) + \varepsilon_{2,CPPB}(E), & E \geq E_g \end{cases} \quad (2)$$

$$\varepsilon_{2,CPPB}(E) = \sum_{q=1}^{4} \mathrm{Im}\left[A_q e^{i\phi} \left(\frac{\Gamma_q}{2E_q - 2E - i\Gamma_q} \right)^{\mu_q} \right] \quad (3)$$

Here, A is the amplitude, E_q is the CP energy, Γ_q is the broadening, μ_q is the dimensionality of the CP, and φ is the phase. E_{res} in the second term in Eq. (1) is the resonance energy outside the range of measurement. The resulting ε is shown in Fig. 3, and shows the same features and trends as the parametric dispersion model. The modified CPPB dispersion model also gave an excellent fit to the data from undoped to 4% Cr doped ZnS (see Fig. 4), and appeared reasonably stable. That is, the weak Gaussian sub-band absorption was only added at the very end of the fit, and only the two highest doping ratios showed a major improvement in MSE (factor 2 for these samples). Note that the Sellmeier function (i.e. the second term in Eq. (1)) was not needed if a sufficient number of oscillators were added in the UV and the corresponding Kramers-Kronig (KK) integral performed up to at least 9 eV. Such oscillators could be estimated from VUV-ellipsometry data.

The parametric fit, with all CPs limited to $\mu = 1$, i.e. excitonic line shapes, gave all reasonable fits without the Gaussian inter-band, implying that the long absorption tail describes the main absorption. However, adding the Gaussian sub-band absorption reduced the final MSE by a factor 2 for the highest doping levels, see Fig. 4. Typical parameters are shown in Table 2. It is observed that the Urbach energy was found to be around 1.2 eV which basically allows for the long tail of the absorption towards lower energies, while the Gaussian is located near 2.57 eV. The advantage of the latter model is that it allows to determine accurate values for the E_0−CP, to describe the range of states through the Urbach tail, and to describe the weak localized states that have features similar to Cr^{2+} photoionization at around 2.8 eV [21].

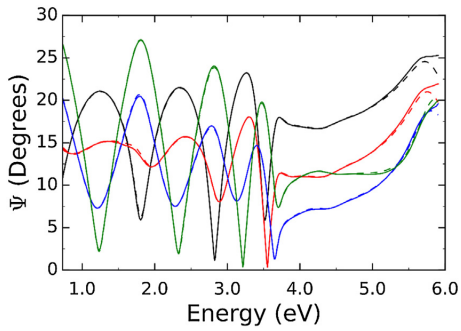

Fig. 4. The ellipsometric parameter Ψ at angles of incidences $\theta_0 = 60$ (black), 65 (red), 70 (blue) and 75 (green) degrees, for 3.3 at.% of Cr doped ZnS. The full lines correspond to the experimental data, and the dotted lines are the CPPB dispersion model fit. (For interpretation of the references to color in this figure legend, the reader is referred to the web version of this article.)

Table 2
Selected parameters used in the CPPB dispersion model for E_g equal to 3.36 eV and ε_∞ varied from 1 to 1.3. The Urbach energy varied from E_u = 1.1–1.3 eV. Broadening and the position of the E_{cr} Gaussian oscillator was set to $\Gamma = 0.80 \pm 0.1$ and $E_{cr} = 2.56 \pm 0.01$ eV E_1 is the position for the center of oscillator, A is the amplitude, Γ is the broadening, and A_{cr} is the amplitude of the Cr contribution.

	ZnS	2.0 at.%	2.3 at.%	3.0 at.%	3.3 at.%	4.0 at.%
E_1 (eV)	5.8	5.7	5.7	5.7	5.7	5.8
A_1	8.35	5.80	5.84	5.83	5.80	5.47
Γ_1 (eV)	0.54	0.46	0.50	0.54	0.53	0.52
A_{cr}	N/A	0.02	0.02	0.06	0.07	0.08

Table 3
The position, E_1, broadening, Γ_1, and amplitude, A_1, for the ZnS film and 2–4 at.% Cr doped ZnS samples for the 2nd derivative analysis.

	ZnS	2.0 at.%	2.3 at.%	3.0 at.%	3.3 at.%	4.0 at.%
E_1	5.73	5.71	5.72	5.73	5.74	5.74
A_1	2.61	3.00	3.19	2.94	2.61	2.25
Γ_1	0.32	0.39	0.42	0.41	0.38	0.37

3.4. Direct inversion and 2nd derivative CPPB analysis

The dielectric function was extracted with the KK-consistent B-spline method [22]. The double derivatives for the PLD series after smoothening are plotted in Fig. 5. The main changes of the double derivatives as a function of doping concentration have been marked with black arrows. When the doping level increases, it is seen that the E_0 feature at 3.7 eV becomes weaker, more broadened but do not change much in energy, while the E_1 feature at around 5.7 eV becomes less broadened and shifts to higher energy.

Some key CP lineshape parameters from the fit to the 2nd derivative of the undoped pulsed laser deposited sample are given in Table 3. The fit of the undoped sample was used as a starting point for the analysis of the doped samples, and a comparison of the prin-

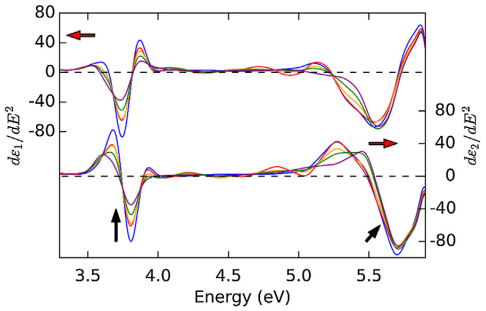

Fig. 5. The double derivatives of the dielectric function for ZnS:Cr. Blue, red, orange, green, and purple for 2.0, 2.3, 3.0, 3.3, and 4.0 at.% Cr, respectively. The red arrow indicate the graph's axis, while the black arrows indicate the trend for increasing Cr at.%. (For interpretation of the references to color in this figure legend, the reader is referred to the web version of this article.)

Table 4
The E_0^1, E_0^2, E_1 and E_2 position, in eV, from the general oscillator model, modified critical point parabolic band model, 2nd derivative analysis (2da) of ε_2 from the B-spline model, as well as values from the literature [6,7] for undoped ZnS.

	Gen. Osc.	Modified CPPB	2da (B-spline)	Ozaki and Adachi [6]	Ghong et al. [7]
E_0^1	3.69	3.34	3.75	3.75	
E_0^2	3.73	3.72	3.78	3.82	
E_1	5.73	5.76	5.73	5.74	5.85
E_2	7.30	7.24	7.00	7.00	7.03

cipal parameters, E_0^1, E_0^2 and E_1 CPs, are shown in Table 4. The CP energies are in overall agreement with the energies extracted by the CPPB model in Ref. [6]. Note that two nearly superposing CPs (one excitonic ($\mu = 1$) and one 3D-M_0 ($\mu = 0.5$, $\varphi = 280$, $E_0 \sim 3.75$ eV)) were found to fit the 2nd derivate spectra, while the CPPB dispersion model systematically rather converged to a single exciton lineshape at 3.73 eV, and a more curious broader lineshape below the E_0 gap (around 3.34 eV).

One hypothesis regarding the crystal structure of the ZnS films was that the original ZnS were mostly ZB phase, while the WZ fraction increased with increasing Cr-content. This was difficult to confirm with XRD measurements as the WZ and ZB peaks overlap [13]. By analyzing the position and amplitude of the E_1 peak, it can be seen that the amplitude diminishes, indicating that the WZ fraction might increase (see Table 3). However, the position of the E_1 peak does not seem to change as one might expect for increasing WZ [8], making the crystal phase purity another possible cause for the broadening and diminishing amplitude for the E_1 peak. Measurements of pure WZ phase ZnS is needed to test this hypothesis.

In order to quantify sub-bandgap absorption as a function of Cr concentration, we estimated the transition strength, f, from the B-spline extracted imaginary part of the dielectric function [22], giving: $f(E) = M \int_{E_1}^{E_2} \varepsilon_2(E) E dE$. The transition strength gave similar results for all dispersion models, and it displays a linear relationship between transition strength and Cr content, indicating that the increase in sub-band absorption is due to increased Cr doping. This relationship was also found and plotted in Ref. [14].

4. Summary and conclusions

Two parametric dispersion models were applied in order to describe undoped ZnS; a harmonic oscillator based model (Cody Lorentz) and a modified CPPB model. By appropriate modelling of the dielectric function, we were able to extract weak sub-bandgap absorption of ZnS:Cr, potentially related to an intermediate band. The parameters of these models were compared to the result of the 2nd derivative analysis (also using CPPB line shapes) of B-spline extracted dielectric function of the films.

The harmonic based model does not in principle convey the details of the CPs (type, dimension etc.), and also consisted of a large number of free parameters. This issue was resolved by using a modified CPPB model, which still allowed for the sharp cut-off at the E_0 gap to be accurately modelled.

As excitonic absorption dominates for ZnS and similar wide bandgap semiconductors, therefore both approaches probably fit equally well, and explains the similar position of the CPs. Finally these CP positions are in good correspondence with those determined using line shape fitting of 2nd derivative spectra of the B-spline extracted dielectric function.

Acknowledgments

This work was performed with partial support from the Norwegian Center for Solar Cell Technology (project 193829) and the Norwegian Research Council (grants 240466 and 221860/F60).

References

[1] A. Luque, A. Marti, Increasing the efficiency of ideal solar cells by photon induced transitions at intermediate levels, Phys. Rev. Lett. 78 (1997) 5014–5017, http://dx.doi.org/10.1103/PhysRevLett.78.5014.
[2] A. Datas, E. López, I. Ramiro, E. Antolín, A. Martí, A. Luque, Intermediate band solar cell with extreme broadband spectrum quantum efficiency, Phys. Rev. Lett. 114 (2015) 1–4, http://dx.doi.org/10.1103/PhysRevLett.114.157701.
[3] C. Tablero, Optoelectronic properties of Cr-substituted II–VI semiconductors, Comput. Mater. Sci. 37 (2006) 483–490, http://dx.doi.org/10.1016/j.commatsci.2005.11.009.
[4] C. Tablero, Effects of the impurity-host interactions on the nonradiative processes in ZnS:Cr, J. Appl. Phys. 108 (2010) 93114, http://dx.doi.org/10.1063/1.3506705.
[5] Collaboration: Authors and editors of the volumes III/17B-22A-41B, Zinc Sulfide (ZnS) Band Structure, Cubic Modification, in: O. Madelung, U. Rössler, M. Schulz (Eds.), Springer Materials–The Landolt–Börnstein Database, 2014 http://www.springermaterials.com.
[6] S. Ozaki, S. Adachi, Optical constants of cubic ZnS, Jpn. J. Appl. Phys. 32 (1993) 5008–5013, http://dx.doi.org/10.1143/jjap.32.5008.
[7] T.H. Ghong, T.J. Kim, Y.D. Kim, Study of the dielectric function of ZnS by spectroscopic ellipsometry, J. Korean Phys. Soc. 42 (2003) 238–241.
[8] J.L. Freeouf, Far-ultraviolet reflectance of II–VI compounds and correlation with the Penn—Phillips gap, Phys. Rev. B 7 (1973) 3810–3830, http://dx.doi.org/10.1103/physrevb.7.3810.
[9] K. Ichino, Y. Morimoto, H. Kobayashi, Molecular beam epitaxy and structural properties of ZnCrS, Phys. Status Solidi 3 (2006) 776–779, http://dx.doi.org/10.1002/pssc.200564699.
[10] M.P. Sarma, G. Wary, Structural and optical properties of nanocrystalline pb1-xCdxS thin films prepared by chemical bath deposition, Am. J. Mater. Sci. Technol. 4 (2015) 58–71, http://dx.doi.org/10.5539/apr.v4n3p75.
[11] A. Luque, A. Martí, E. Antolín, C. Tablero, Intermediate bands versus levels in non-radiative recombination, Phys. B Condens. Matter 382 (2006) 320–327, http://dx.doi.org/10.1016/j.physb.2006.03.006.
[12] H. Tompkins, E. Irene, Handbook of Ellipsometry, Elsevier Inc., 2005, http://dx.doi.org/10.1007/3-540-27488-x.
[13] M. Nematollahi, X. Yang, U.J. Gibson, T.W. Reenaas, Pulsed laser ablation and deposition of ZnS:Cr, Thin Solid Films 590 (2015) 28–32, http://dx.doi.org/10.1016/j.tsf.2015.07.046.
[14] M. Nematollahi, X. Yang, L.M.S. Aas, Z. Ghadyani, M. Kildemo, U.J. Gibson, T.W. Reenaas, Molecular beam and pulsed laser deposition of ZnS:Cr for intermediate band solar cells, Sol. Energy Mater. Sol. Cells 141 (2015) 322–330, http://dx.doi.org/10.1016/j.solmat.2015.06.004.
[15] H. Fujiwara, J. Koh, P. Rovira, R. Collins, Assessment of effective-medium theories in the analysis of nucleation and microscopic surface roughness evolution for semiconductor thin films, Phys. Rev. B 61 (2000) 10832–10844, http://dx.doi.org/10.1103/PhysRevB.61.10832.
[16] M. Nematollahi, X. Yang, E. Seim, P.E. Vullum, R. Holmestad, U.J. Gibson, T.W. Reenaas, Compositional and structural properties of pulsed laser-deposited ZnS:Cr films, Appl. Phys. A 122 (2016) 1–11, http://dx.doi.org/10.1007/s00339-016-9594-9.
[17] B. Johs, C.M. Herzinger, Quantifying the accuracy of ellipsometer systems, Phys. Status Solidi 5 (2008) 1031–1035, http://dx.doi.org/10.1002/pssc.200777755.

[18] K. Ghimire, H.F. Haneef, R.W. Collins, N.J. Podraza, Optical properties of single-crystal Gd3Ga5O12 from the infrared to ultraviolet, Phys. Status Solidi 252 (2015) 2191–2198, http://dx.doi.org/10.1002/pssb.201552115.
[19] J. Tauc, R. Grigorovici, A. Vancu, Optical properties and electronic structure of amorphous germanium, Phys. Status Solidi 15 (1966) 627, http://dx.doi.org/10.1002/pssb.19660150224.
[20] G.E. Jellison Jr., F.A. Modine, Parameterization of the optical functions of amorphous materials in the interband region, Appl. Phys. Lett. 69 (1996) 371–373, http://dx.doi.org/10.1063/1.118064.
[21] N.A. Vlasenko, P.F. Oleksenko, Z.L. Denisova, M.O. Mukhlyo, L.I. Veligura, Cr-related energy levels and mechanism of Cr2+ ion photorecharge in ZnS:Cr, Phys. Status Solidi Basic Res. 245 (2008) 2550–2557, http://dx.doi.org/10.1002/pssb.200844044.
[22] W. Oldham, Numerical techniques for the analysis of lossy films, Surf. Sci. 16 (1969) 97–103, http://dx.doi.org/10.1016/0039-6028(69)90008-9.

Appendix A

Supplementary material for Paper 5

Katherine Inzani, Mohammadreza Nematollahi, Sverre M. Selbach, Tor Grande, Magnus Langøien Waalekalv, Thomas Brakstad, Turid Worren Reenaas, Morten Kildemo, and Fride Vollum-Bruer

"Tailoring properties of nanostructured MoO_{3-x} thin films by aqueous solution deposition"

Applied Surface Science **459** (2018), pp. 822-829

Supplementary information

Tailoring properties of nanostructured MoO_{3-x} thin films by aqueous solution deposition

Katherine Inzani[1], Mohammadreza Nematollahi[2], Sverre M. Selbach[1], Tor Grande[1], Magnus Langøien Waalekalv[2], Thomas Brakstad[2], Turid Worren Reenaas[2], Morten Kildemo[2] and Fride Vullum-Bruer[1]*

*[1]Department of Materials Science and Engineering, Norwegian University of Science and Technology, N-7491 Trondheim, Norway. [2]Department of Physics, Norwegian University of Science and Technology, N-7491 Trondheim, Norway. *Phone: +47-73-59-39-76; e-mail: fride.vullum-bruer@ntnu.no*

SI.1 Details of the X-ray photoelectron spectroscopy measurements

X-ray photoelectron spectroscopy (XPS) was obtained with a Kratos Axis Ultra with monochromatic Al Kα X-ray source (hv = 1486.6 eV, 15 mA, 15 kV, with lowest energy resolution 150 meV). The Kratos charge neutralizer system was used for all measurements, and the binding energies (Eb) were corrected by Eb equal to 284.8 eV of adventitious C 1s. Mo 3d core levels were measured for the Eb range 219–242 eV. Measurements were carried out with a pass energy of 20 eV. Background modelling and subtraction, peak fitting, and quantification of the components were processed using CasaXPS software (version 2.3.16). An offset Shirley background was subtracted from the spectrum from a blend of a Shirley and linear backgrounds $OS(E{:}\lambda) = S(E)(1-\lambda)+L(E)\lambda$, where the Shirley and the linear background are represented by $\lambda = 0$ and $\lambda = 1$, respectively. In the curve fitting models, $\lambda = 0.3$ was used. For Mo 3d peaks a LF(α, β, w, m) line shape was used (CasaXPS), which is a Lorentzian line shape including consideration of the Gaussian instrumental broadening. The Mo 3d peaks had a slightly asymmetric line shape.

SI.2 Details of the spectroscopic ellipsometry model

Spectroscopic ellipsometry data acquisition and analysis were done with the software CompleteEASE 4.64. The optical response was determined by fitting to the parameters N, C and S (N = cos2Ψ, C = sin2ΨcosΔ, S = sin2ΨsinΔ, where Ψ and Δ are the ellipsometric angles measured). The optical model consisted of three elements, surface roughness, thin film and substrate. The film optical properties were modelled by a parametric dispersion model from which the refractive index, film thickness and band gap were extracted. This modelled layer consists of two Tauc-Lorentz oscillators for describing the dielectric function above the band gap, one Gaussian for absorption below the band gap, and a Drude oscillator for free carrier contribution at low photon energies.[36,37] In the Tauc-Lorentz analytical expression the imaginary part of the dielectric function is given by

$$\varepsilon_{\mathrm{imTL}}(E) = \frac{AE_0Br\left(E-E_g\right)^2}{\left(E^2-E_0^2\right)^2+Br^2E^2} * \frac{1}{E} \text{ for } E > E_g \quad (1)$$

$$\varepsilon_{\mathrm{imTL}}(E) = 0 \text{ for } E \leq 0$$

Here, A is the amplitude, E_0 is the centre resonance energy, Br is the broadening and E_g is the optical bandgap of the oscillator. The real part of the dielectric function is given by the Kramers-Kronig integral of ε_{im}.[37] A Gaussian lineshape in $\varepsilon_{\mathrm{im}}$ with a Kramers-Kronig consistent line shape for $\varepsilon_{\mathrm{real}}$ is given by

$$\varepsilon_{imGaus} = Ae^{-\left(\frac{E-E_0}{\sigma}\right)^2} - Ae^{-\left(\frac{E+E_0}{\sigma}\right)^2} \quad (2)$$

with $\sigma = Br/2\sqrt{\ln(2)}$. The Drude contribution is modelled by

$$\varepsilon_{Drude}(E) = \frac{-\hbar^2}{\varepsilon_0\rho(\tau*E^2+i\hbar E)} \quad (3)$$

where ρ is the resistivity (Ωcm) and τ is the mean scattering time (fs).[36] The films were assumed to be homogenous and isotropic. The roughness layer was modelled by a simple Bruggeman effective medium theory containing 50/50 of void/$MoO_{(3-x)}$.[38] The agreement between the optical model and the measured ellipsometric spectra was quantified by the mean squared error (MSE).[39] All reflection ellipsometry spectra were modelled as thin films on a semi-infinite quartz substrate, and transmittance was simulated on a finite substrate thickness assuming incoherent reflections.

SI.3. Sampling of line profiles to obtain nanocrystallite step height, from an AFM image of a film deposited from 0.1 mol [Mo] L^{-1} AHM solution

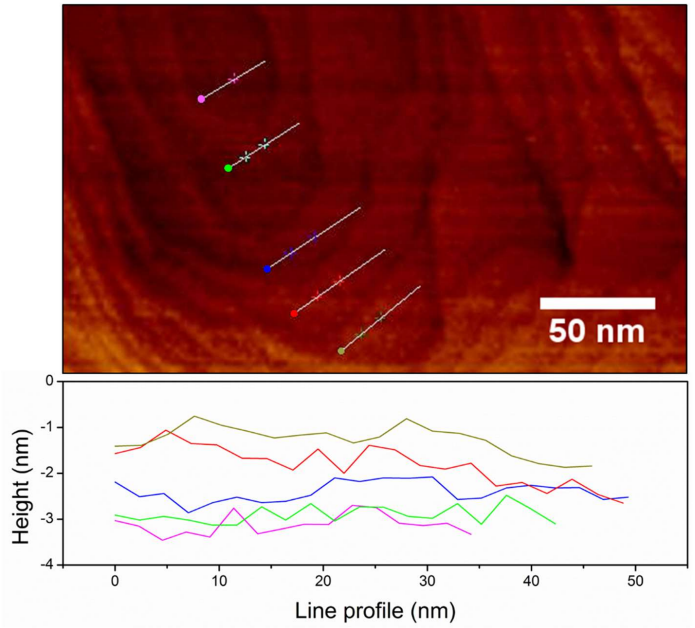

SI.4. Sampling of line profiles from the centre to the edge of a grain, from an AFM image of a film deposited from 0.1 mol [Mo] L^{-1} AHM solution

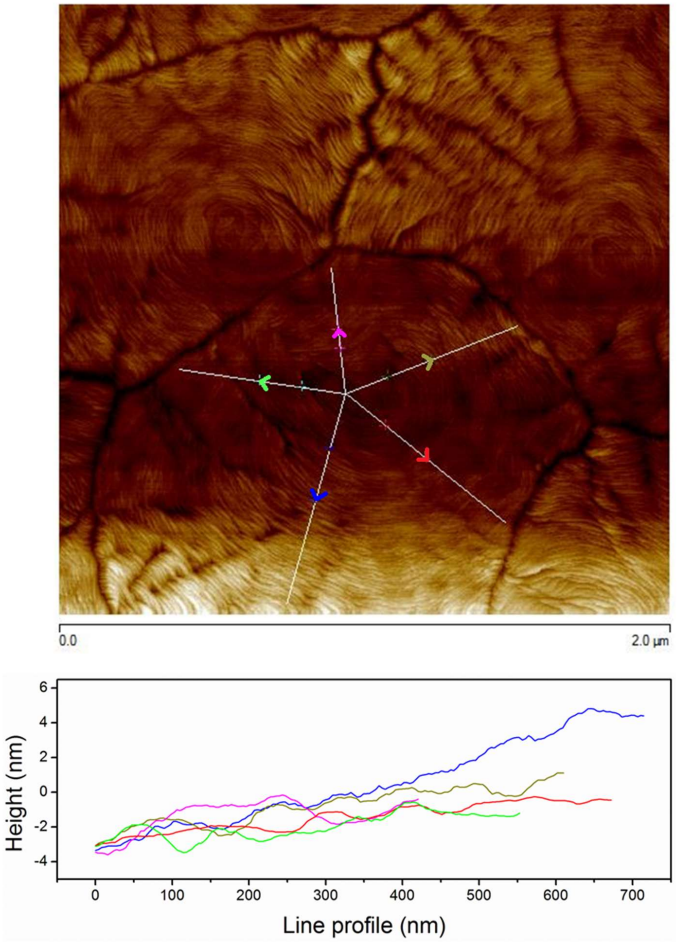

The AFM micrograph is the same as that in figure 2d, but this image has not had post-processing flattening applied to it. The line profiles have been smoothed with 10-point adjacent averaging.

SI.5. Key parameters for the SE model of films from two solution concentrations and various reduction temperatures: the total thickness of the film, band gap energy, E_g, amplitude of the Gaussian, A_{Gauss}, and mean squared error, MSE, of the model to measured N, C, S values.

Film deposition [mol [Mo] L^{-1}]	Reduction temperature [°C]	Thickness [nm]	E_g [eV]	A_{Gauss}	MSE
0.1	-	12	3.3	-	2.7
	200	11	3.3	0.13	2.4
	300	12	3.1	0.89	4.4
	350	10	3.3	1.34	3.5
	400	13	3.2	1.27	3.7
	450	6	1.9	2.06	4.8
0.5	-	75	3.0	0.07	5.9
	200	68	3.1	0.09	4.9
	300	69	3.2	0.13	5.3
	350	69	3.2	0.13	4.7
	400	67	3.1	0.32	4.2
	450	63	2.4	0.15	8.6

The band gap energy given here corresponds to the Tauc gap common to the two Tauc-Lorentz oscillators representing the interband transitions. These values extracted from the model show that at high reduction temperature (≥ 450 °C) the band gap narrows. However, one of the limitations with the Tauc-Lorentz parametric dispersion model is that it assumes no absorption below the band gap. This forces any below band gap absorption detected to be described as a change in the band gap, when this could be described by an Urbach tail caused by defect states.[a] Therefore, further work should be done in order to precisely determine the actual band gap and not only the onset of absorption as described here.

SI.6. (a) Measured N, C, and S values for the 0.5 mol [Mo] L^{-1} film deposition reduced at 400°C at 65° incident angle, with the model response in black. (b) The dielectric function at the top, middle and bottom of the film for the same sample.

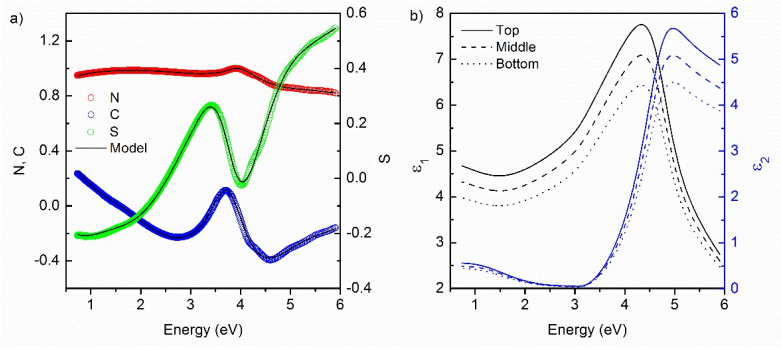

For the thicker films of the 0.5 mol [Mo] L^{-1} deposition series, a linear grading of 10 % was needed to fit the data, where the top layer has a higher refractive index than the lower layer. This is shown in SI.6b for the sample reduced at 400 °C. In Figures 8c and 8d in the manuscript, only the middle dielectric function is plotted.

The linear grading in the 0.5 mol [Mo] L^{-1} deposited films could be due to the oxygen reduction initiating from the top, creating a more reduced film on the top compared to the bottom of the film. This, however, is not the case for the thick film reduced at 450 °C, nor any of the 0.1 mol [Mo] L^{-1} deposited film series. The reason for this could be that at higher temperatures or reduced film thicknesses the films have time to reach an equilibrium of phases.

SI.7 The measured (solid lines) and model generated (dashed lines) transmittance of the films from 0.1 mol [Mo] L^{-1} solution (a), and 0.5 mol [Mo] L^{-1} solution (b) after reduction in 5% H_2-95% Ar gas at 200, 300, 350, 400 and 450 °C, and films with no treatment in reducing gas.

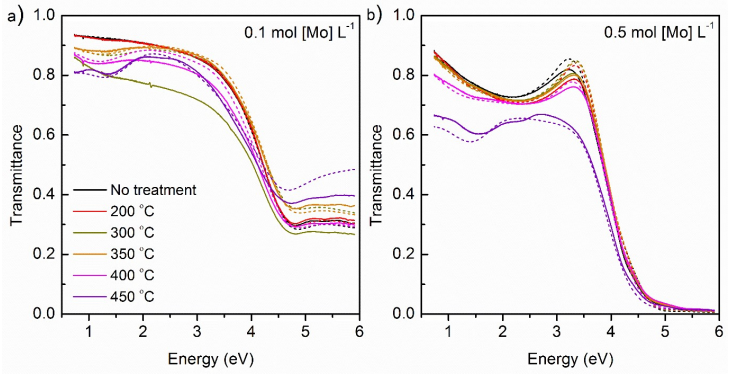

It should be noted that the transmittance of the thinnest films remains at 0.2-0.4 at high photon energies, due to the thickness of the samples being too small to absorb all incident light, as has been seen with similarly thin Mo oxide films.[b]

References

a – Ferlauto, A. S., Ferreira, G. M., Pearce, J. M., Wronski, C. R., Collins, R. W., Deng, X. & Ganguly, G. Analytical model for the optical functions of amorphous semiconductors and its applications for thin film solar cells. *Thin Solid Films* **455–456,** 388–392 (2004).

b – Vasilopoulou, M., Douvas, A. M., Georgiadou, D. G., Palilis, L. C., Kennou, S., Sygellou, L., Soultati, A., Kostis, I., Papadimitropoulos, G., Davazoglou, D., *et al.* The Influence of Hydrogenation and Oxygen Vacancies on Molybdenum Oxides Work Function and Gap States for Application in Organic Optoelectronics. *J. Am. Chem. Soc.* **134,** 16178–16187 (2012).

ISBN 978-82-326-7236-3 (printed ver.)
ISBN 978-82-326-7235-6 (electronic ver.)
ISSN 1503-8181 (printed ver.)
ISSN 2703-8084 (online ver.)

NTNU

Norwegian University of
Science and Technology